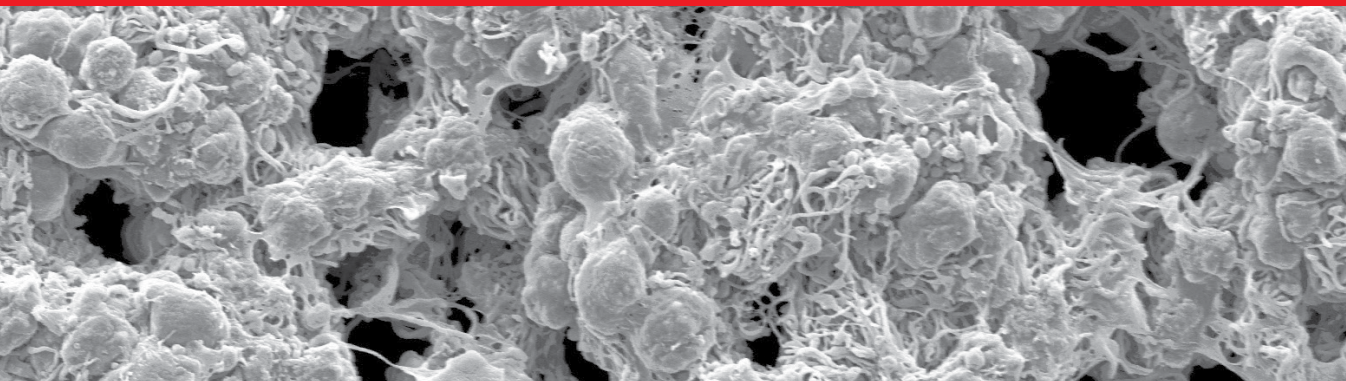


IntechOpen

New Advances in Powder Technology

*Edited by Shashanka Rajendrachari,
Volodymyr Shatokha and Baris Avar*



New Advances in Powder Technology

*Edited by Shashanka Rajendrachari,
Volodymyr Shatokha and Baris Avar*

Published in London, United Kingdom

New Advances in Powder Technology

<http://dx.doi.org/10.5772/intechopen.102106>

Edited by Shashanka Rajendrachari, Volodymyr Shatokha and Baris Avar

Contributors

Chang Li, Zhongshi Ni, Ying Li, Hary Lanto L. Razafindralambo, Mohamed Amin Ali, Joël De Coninck, Pattapagalu Naga Sudhakar Srinivas, Pittam Srinivas Rao, Venkateshwar Reddy Prathapalli, Nallamilli Srinivas Reddy, Volodymyr Shatokha, Yuri Korobeinikov, Dahee Park, Hye Young Koo, Olga Klimova-Korsmik, Gleb Andreevich Turichin, Marina Gushchina, Escarlet Batista da Silva, Lioudmila Aleksandrovna Matlakhova, Marcia Giardinieri Azevedo, Luciano José José de Oliveira, Bárbara Ferreira de Oliveira

© The Editor(s) and the Author(s) 2023

The rights of the editor(s) and the author(s) have been asserted in accordance with the Copyright, Designs and Patents Act 1988. All rights to the book as a whole are reserved by INTECHOPEN LIMITED. The book as a whole (compilation) cannot be reproduced, distributed or used for commercial or non-commercial purposes without INTECHOPEN LIMITED's written permission. Enquiries concerning the use of the book should be directed to INTECHOPEN LIMITED rights and permissions department (permissions@intechopen.com).

Violations are liable to prosecution under the governing Copyright Law.



Individual chapters of this publication are distributed under the terms of the Creative Commons Attribution 3.0 Unported License which permits commercial use, distribution and reproduction of the individual chapters, provided the original author(s) and source publication are appropriately acknowledged. If so indicated, certain images may not be included under the Creative Commons license. In such cases users will need to obtain permission from the license holder to reproduce the material. More details and guidelines concerning content reuse and adaptation can be found at <http://www.intechopen.com/copyright-policy.html>.

Notice

Statements and opinions expressed in the chapters are those of the individual contributors and not necessarily those of the editors or publisher. No responsibility is accepted for the accuracy of information contained in the published chapters. The publisher assumes no responsibility for any damage or injury to persons or property arising out of the use of any materials, instructions, methods or ideas contained in the book.

First published in London, United Kingdom, 2023 by IntechOpen

IntechOpen is the global imprint of INTECHOPEN LIMITED, registered in England and Wales, registration number: 11086078, 5 Princes Gate Court, London, SW7 2QJ, United Kingdom

British Library Cataloguing-in-Publication Data

A catalogue record for this book is available from the British Library

Additional hard and PDF copies can be obtained from orders@intechopen.com

New Advances in Powder Technology

Edited by Shashanka Rajendrachari, Volodymyr Shatokha and Baris Avar

p. cm.

Print ISBN 978-1-83769-992-6

Online ISBN 978-1-83768-220-1

eBook (PDF) ISBN 978-1-83768-221-8

We are IntechOpen, the world's leading publisher of Open Access books Built by scientists, for scientists

6,500+

Open access books available

176,000+

International authors and editors

190M+

Downloads

156

Countries delivered to

Our authors are among the
Top 1%

most cited scientists

12.2%

Contributors from top 500 universities



WEB OF SCIENCE™

Selection of our books indexed in the Book Citation Index
in Web of Science™ Core Collection (BKCI)

Interested in publishing with us?
Contact book.department@intechopen.com

Numbers displayed above are based on latest data collected.
For more information visit www.intechopen.com



Meet the editors



Dr. Shashanka Rajendrachari is an assistant professor in the Department of Metallurgical and Materials Engineering, Bartın University, Turkey. He obtained a Ph.D. from the Department of Metallurgical and Materials Engineering, National Institute of Technology Rourkela, India. He also holds an MSc in Industrial Chemistry and an MTech in Nanoscience and Technology from Kuvempu University, Karnataka, India. He is the recipient of numerous national and international awards for his research contributions. His research areas are nano-structured alloys, powder metallurgy, electrochemical sensors, corrosion, and smart and high-entropy alloys. He has 8 years of research and teaching experience and has published more than fifty-five research articles, ten books, and nine book chapters.



Volodymyr Shatokha graduated in 1982 as a Ferrous Metallurgy engineer. In 1985, he received a Ph.D. degree from the Dnipropetrovsk Metallurgical Institute (known since 1999 as the National Metallurgical Academy of Ukraine and since 2021 as the Ukrainian State University of Science and Technology). In 1998, he received the title of professor with the Ironmaking Chair. During 1999–2002, he was the dean of the Metallurgical Faculty. During 2002–2021, he was the vice-rector for Research and Education. Since 2022 he is a professor of the Ironmaking & Steelmaking Department. His research deals mainly with the properties of iron ore materials, physicochemical processes of ironmaking, recycling methods, sustainability analysis, etc. He is the author of over 180 research papers, 7 books, and 7 patents. He is an honorary professor at the Inner Mongolia University of Science and Technology, China, and a visiting professor at the University of Tokyo (2013). He is a laureate of the State Prize of Ukraine in Science and Technology (2010) and a fellow of the Erasmus+ Jean Monnet Programme for the EU climate and energy policy studies (since 2015).



Baris Avar is an associate professor in the Department of Metallurgical and Materials Engineering, Zonguldak Bülent Ecevit University, Turkey. He is currently involved in teaching and research activities focused on material sciences and nanotechnology. His research interests include nanocrystalline, amorphous, and quasicrystalline alloys, as well as mechanical alloying and rapid solidification processes.

Contents

Preface	XI
Section 1 Fabrication of Powders	1
Chapter 1 Conductive Powder Synthesis Technology for Improving Electrical Conductivity by One-Pot Ultrasonic Spray Pyrolysis Process <i>by Hye Young Koo and Dahee Park</i>	3
Chapter 2 Features of the Powder Application in Direct Laser Deposition Technology <i>by Marina Gushchina, Olga Klimova-Korsmik and Gleb Turichin</i>	19
Section 2 Wettability of Powders	43
Chapter 3 An Application of Bio-Inspired Superwetting Surfaces: Water Collection <i>by Chang Li, Zhongshi Ni and Ying Li</i>	45
Chapter 4 Wettability of Probiotic Powders: Fundamentals, Methodologies, and Applications <i>by Mohamed Amin Ali, Joël De Coninck and Hary L. Razafindralambo</i>	67
Chapter 5 Wetting of Solid Iron by Molten FeO-Containing Slag <i>by Volodymyr Shatokha and Yuri Korobeynikov</i>	87
Section 3 Consolidation of Powders	99
Chapter 6 Spark Plasma Sintering of NiCrSiBC Alloys <i>by Escarlet Batista da Silva, Márcia Giardinieri Azevedo, Liudmila Aleksandrovna Matlakhova, Bárbara Ferreira de Oliveira and Luciano José de Oliveira</i>	101

Chapter 7

111

**Experimentation and Optimization of Multilayered Aluminum-Based
Functionally Graded Materials**

*by Pattapagalu Naga Sudhakar Srinivas, Pittam Srinivas Rao, Kolari Deepak
and Nallamilli Srinivas Reddy*

Preface

New Advances in Powder Technology consists of seven chapters that discuss powder metallurgy, including preparations, properties, and applications.

Section 1, “Fabrication of Powders”, includes two chapters. Chapter 1 focuses on the spray pyrolysis synthesis of powders and their applications as electrode materials. Chapter 2 discusses the additive manufacturing of powders by direct laser deposition method. It also presents the main requirements for the direct laser deposition method and characterizes the prepared metal powders. This section is useful for powder metallurgists, materials engineers, and chemists.

Section 2, “Wettability of Powders”, includes three chapters. Chapters 3–5 focus on the wettability properties of powders by measuring the interface of the powders and the dispersing media by the sessile drop method and the capillary rise technique. Section 2 is useful for chemists, biologists, and material researchers.

Section 3, “Consolidation of Powders”, includes Chapters 6 and 7, which discuss the consolidation of metal powders by spark plasma sintering and conventional sintering methods, respectively. Both chapters investigate the density and mechanical and surface properties of metal and alloy powders. They also report on the microstructure evolution of powders during consolidation. Section 3 is useful for metallurgists, powder metallurgists, material researchers, and mechanical engineers to understand the basics of sintering alloys and their mechanical properties.

Overall, this book is an informative resource for a wide range of readers, including engineering students and industry professionals.

Dr. Shashanka Rajendrachari

Assistant Professor,
Department of Metallurgical and Materials Engineering,
Bartın University,
Bartın, Turkey

Volodymyr Shatokha

Iron and Steel Institute of the National Academy of Science of Ukraine,
Ukraine

Baris Avar

Department of Metallurgical and Materials Engineering,
Zonguldak Bülent Ecevit University,
Zonguldak, Turkey

Section 1

Fabrication of Powders

Conductive Powder Synthesis Technology for Improving Electrical Conductivity by One-Pot Ultrasonic Spray Pyrolysis Process

Hye Young Koo and Dahee Park

Abstract

In this chapter, we will study the spray pyrolysis process, which is a bottom-up process, and examine the composite electrode powder synthesis process and properties of the core-shell structure. Generally, it is difficult to produce fine particles from metal powders using the top-down method. Thus, the liquid phase method, which is a bottom-up process, is mainly used. However, the liquid phase method has a problem in that impurities exist in the particles. In addition, it is difficult to control the precipitation when synthesizing powder using a solution containing several types of metal salts. The spray pyrolysis process introduced here made it possible to produce composite particles in a one-pot manner without any additional processes for synthesizing the core-shell structure. In the case of core-shell structure of Ag-glass composite powder, the specific resistance of the composite electrode was significantly lowered, compared to the electrode formed by mixing glass frits individually, which improved the dispersibility of the glass. In the case of Cu composite particles with a coating layer, both Ag and glass coating layers formed a passivation layer to improve atmospheric stability, and the introduction of a coating material also improved electrical properties.

Keywords: spray pyrolysis, electrode materials, conductive powder, core-shell structure, composite

1. Introduction

Metals with high intrinsic conductivity, such as gold, silver, and copper, are mainly used as electrodes. Conductive powders using noble metals are easily synthesized into metals even in an oxidizing atmosphere, whereas transition metals are synthesized into metal in a reducing atmosphere [1].

Generally, the powder synthesis technology is divided into top-down and bottom-up methods. The solid phase method can be classified as a top-down method, while the liquid phase method and gas phase method are regarded as bottom-up methods. In the solid phase method, mechanical energy is applied to the raw materials of the

desired composition in order to induce bonding and pulverization repeatedly between the powders, which reduce the particle size and synthesize powder while continuously contacting a new surface. Then, synthesis is completed at room temperature or a desired composition is obtained through post-treatment. The mechanical alloying method is a representative solid phase method. Compared to the bottom-up method, this method has the advantages of relatively easy process operation, low cost, and fewer by-products. However, it is limited in reducing the particle size, and homogeneity of the particles is not secured locally when synthesizing multi-component particles [2–6]. In particular, in pulverization of metals, it is difficult to atomize through crushing due to the ductility of the metal. Furthermore, since spheroidization through crushing is impossible, synthesizing conductive spherical powders through the solid phase method is not possible.

The liquid phase method ionizes a metal salt in a solvent to recover the synthesized particles using a reducing or precipitating agent. Since the raw materials can be mixed evenly at the molecular level, it is possible to control the composition uniformly, and the particle size and distribution can be controlled uniformly as well. Synthesis can be realized at a relatively low temperature, and thus, the method has the advantage of low process cost. However, this method generates substantial amount of chemical solvent byproducts, because particles are precipitated by chemical reaction. Moreover, it is difficult to improve the purity due to residual chemical substances in the particles. In addition, it has the disadvantage of low crystallinity, since it is synthesized at low a temperature [7–10].

The gas phase method is a process in which the raw material is divided into atomic or molecular units by vaporizing a metal salt or solution of metal salt, and then, particles are synthesized through nucleation, growth, and agglomeration during condensation. Examples of such a method include Physical Vapor Deposition (PVD) and Chemical Vapor Deposition (CVD). In the gas phase method, the vaporized molecules are nucleated again to grow into particles, and thus, fine particles can be synthesized. It is an advantageous process for producing high-purity particles with low residues of C, N, S, etc., because the synthesis occurs at a high temperature. However, there are some difficulties in synthesizing alloy powders, because non-uniformity may occur due to the difference in vapor pressure during the vaporizing stage. Additionally, the production cost is also high [11–16].

The spherical shape is preferred for conductive powders, because the density of the electrode must be high after formation. As the dispersion is suboptimal when significantly small particles are applied to the manufacturing paste, mixtures of particles with sub-micron sizes are mainly used. Therefore, synthesis has been performed mainly through the liquid phase process. However, in the case of the liquid phase process, since metal particles are synthesized through a reducing agent, residual carbon is present in the particles, which lowers the purity, thereby lowering the conductivity.

In order to overcome the disadvantages of the liquid phase method, a method for synthesizing metals at high temperature using a gas phase method is introduced, but in the case of PVD and CVD, the process for atomization of 0.2 μm or less. This is due to the nature of the process in which vaporized molecules are condensed and powdered. This characteristic is very advantageous, but there is a limit to synthesizing particles with a size of sub-micron to 1 μm .

The ultrasonic spray pyrolysis process is a process that simultaneously utilizes the advantages of the bottom-up, liquid phase, and gas phase methods. The desired raw material is placed in a solvent to prepare a solution, and fine droplets are generated using an ultrasonic generator, followed by heating in a high-temperature furnace.

It is a process of synthesizing particles in within seconds by passing through drying and thermal decomposition. This is similar to a process of synthesizing particles by generating fine-sized droplets in the form of aerosols, similar to vaporizing a solution using a homogeneous solution at the molecular level. Additionally, it is a process that can utilize both the effects of the gas phase and liquid phase methods, as it starts from the liquid phase to synthesize the powder using the sprayed droplets. Since the spray pyrolysis process performs synthesis using the initial raw material as a solution, it is also advantageous to produce multi-component particles that contain trace elements. Furthermore, this process facilitates synthesizing composite powders using various additives during solution preparation. In particular, the mist comprising a solution with a uniform composition passes through the heating furnace to form particles such that the composition of the entire solution is kept the same, and spherical particles are mainly synthesized in a droplet-like form.

The main requirements for conductive powders are spherical shape, low resistivity, high electrical conductivity, high purity, high crystallinity, low temperature sintering, oxidation resistance, etc. The spray pyrolysis process produces spherical shaped powders, since it maintains the shape of the droplets. Moreover, the pyrolysis process enables synthesizing high-purity and highly crystalline particles with a size of 1 μm or less.

When manufacturing an electrode using a conductive powder, a paste is prepared by mixing the conductive powder and glass frit as an inorganic binder with an organic binder, and printing is used to produce an electrode layer. It is essential to control the surface oxidation of the conductive powder in order to improve the density of the electrode, and the presence or absence of glass frit and particle characteristics are very important [17]. The mixing ratio of the conductive powder of the electrode and the glass frit is generally at least 8–20 times different. In particular, amorphous glass frit generally synthesizes powders through crushing, and realizing uniform dispersion becomes difficult due to the irregular size. Further, in the case of transition metal conductive powders, in addition to the problem of mixing glass frit, an oxide layer is formed on the surface powder after synthesis, since it is easily oxidized even at room temperature. This inhibits the densification of the electrode by decreasing sinterability when forming electrodes and leads to poor conductivity due to oxidation.

In this chapter, a method for synthesizing a composite electrode powder with a core-shell structure using a single-step phase-segregation mechanism using the ultrasonic spray pyrolysis process is described, and the corresponding characteristics are studied. The proposed method overcomes the limitations of the conductive paste process. Moreover, this chapter summarizes some representative studies on the subject.

2. Experimental procedure

In the ultrasonic spray pyrolysis process, a precursor solution with a dissolved salt of a desired composition is generated into fine droplets using an ultrasonic generator, and the generated droplets are dried using a carrier gas in an oxidizing, inert, or reducing atmosphere through a high-temperature heating furnace. It undergoes a pyrolysis process and synthesizes particles of the desired composition through process controls, such as the type of salt used in this process, concentration of the solution, presence or absence of additives, type and speed of the carrier gas, temperature, length, and tube width of the heating furnace. Ag composite powder has the characteristic of being synthesized as a metal powder even if it passes through a high temperature of 900°C or higher using air, and transition-metal-based materials

such as Cu can be synthesized at a temperature of 900°C or higher under a reducing atmosphere. All particles of the core-shell structure used in this chapter were synthesized in one-step through the same process of synthesizing electrode powder of a single composition by including all desired compositions in the solution. The particles maintained spherical shape, because the synthesis was performed without a separate post-processing for composite powder synthesis. The particle morphology was observed through scanning electron microscopy (SEM) and transmission electron microscopy (TEM), and crystal structure analysis was performed with X-ray diffraction (XRD). In addition, by analyzing energy-dispersive spectroscopy (EDS) mapping through scanning transmission electron (STEM), the composition of the surface and the inside was observed. The powder thus synthesized was prepared into paste, screen-printed, and then heat-treated at a uniform temperature to form an electrode layer. The specific resistivities of these heat-treated electrodes were measured and compared through the four-point probe method.

3. Conductive Ag-glass composite powder

Ag has very high conductivity, and thus, it has been used as an electrode for solar cells and various electric circuits [18–20].

The electrode layer formed is mixed with glass frit and an inorganic binder in addition to the conductive powder and organic binder to form a paste through heat treatment after printing. The glass frit plays an important role when sintering power by acting as a pool of liquid sintering agent, as well as in densification by helping to form an electrode layer without pores between the powders. Since a small amount (The mixing ratio of the conductive powder of the electrode and the glass frit is generally at least 8–20 times different) is added compared to the conductive powder, it is very difficult to evenly disperse it throughout. In addition, when a large amount is added to evenly disperse the entire electrode layer, the content of the conductive powder must be relatively low due to the density of the paste, which causes a problem of lowering the conductivity. In order to overcome this problem, the electrode powder synthesis technology in which glass and Ag powder are composited into a core-shell

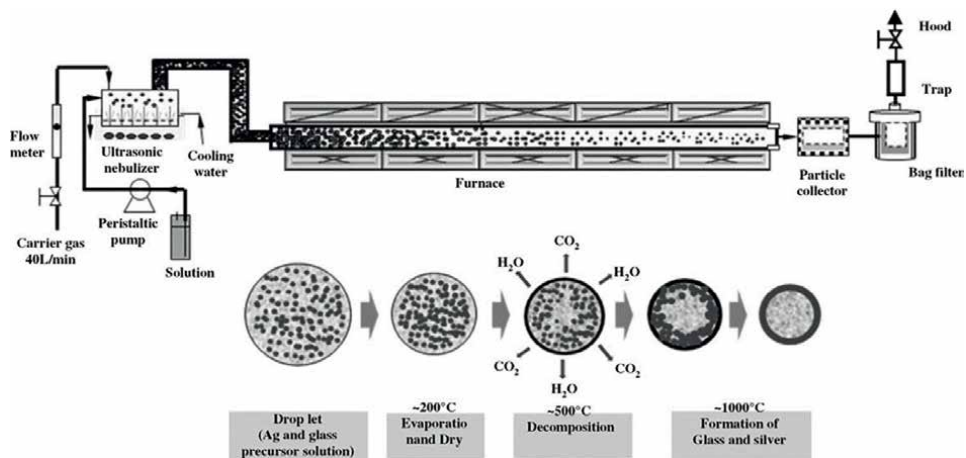


Figure 1. Formation mechanism of silver-glass composite powder [21].

structure using the spray pyrolysis process has been reported in several papers [21–24]. Composite powders of this structure are manufactured by mixing silver nitrate and a salt comprising glass in a precursor solution under the same process of synthesizing powder (pure Ag) through ultrasonic spray pyrolysis process, as shown in **Figure 1**. It is analyzed that during the pyrolysis and melting process, the glass is pushed into the shell due to the density difference between glass and Ag (glass: 2.4–2.8 g/cm³, Ag: 10.5 g/cm³), forming a core-shell structure. Structural analysis of these particles showed that glass is present on the surface by comparing the composition of the shell and core in the DES analysis using STEM, as shown in **Figure 2**.

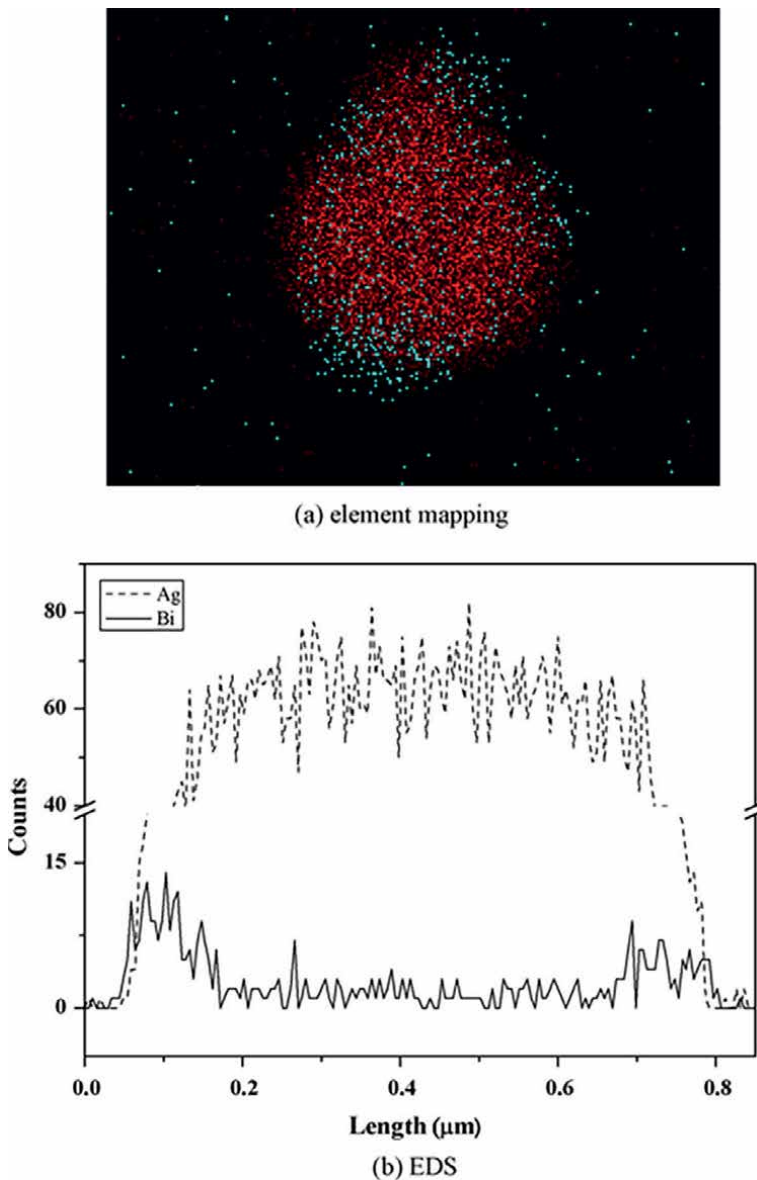


Figure 2. Element mapping and EDS results of the composite powder [21].

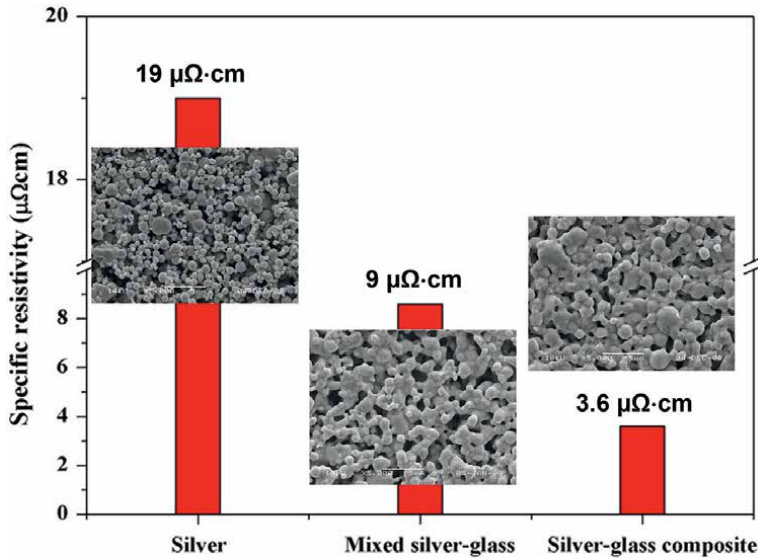


Figure 3. SEM photographs of surfaces and specific resistivity of silver conducting films sintered at a temperature of 450°C [21].

For the electrode layer thus formed, the effect of the composite powder on the densification of the electrode was analyzed through SEM and resistivity analysis as shown in **Figure 3**. As can be confirmed from the SEM analysis, in the electrode layer using only Ag powder, there are several pores without complete connection between the Ag particles, whereas in the case of the electrode layer using the composite powder, the pores on the surface of the electrode layer are significantly reduced, and the contact force between the electrode powders is improved. The specific resistances of the electrodes formed using Ag powder, Ag powder and spherical glass powder mixture, and Ag-glass composite powder were 19 $\mu\Omega\cdot\text{cm}$, 9 $\mu\Omega\cdot\text{cm}$, and 3.6 $\mu\Omega\cdot\text{cm}$, respectively. The specific resistivity was lowered to approximately 50% compared to using only Ag, and approximately 40% compared to the composite powder through ideal

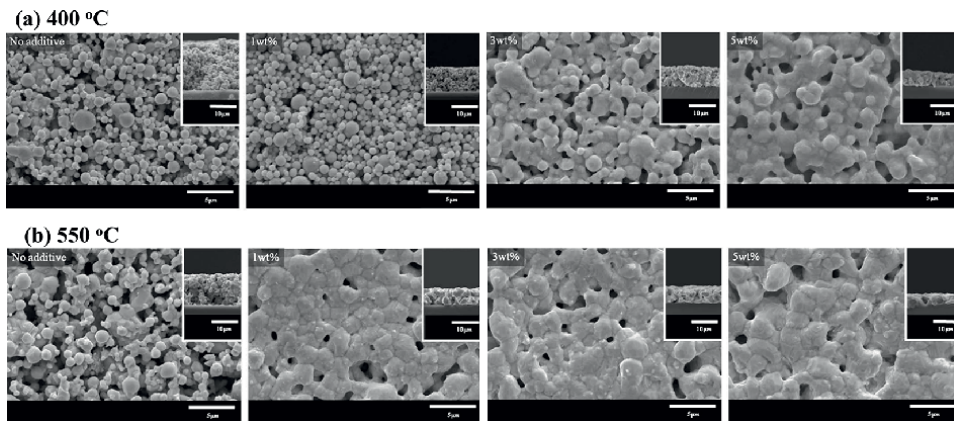


Figure 4. SEM photographs of surfaces of silver conducting films with various contents of glass sintered at a temperature of 400 and 550°C [24].

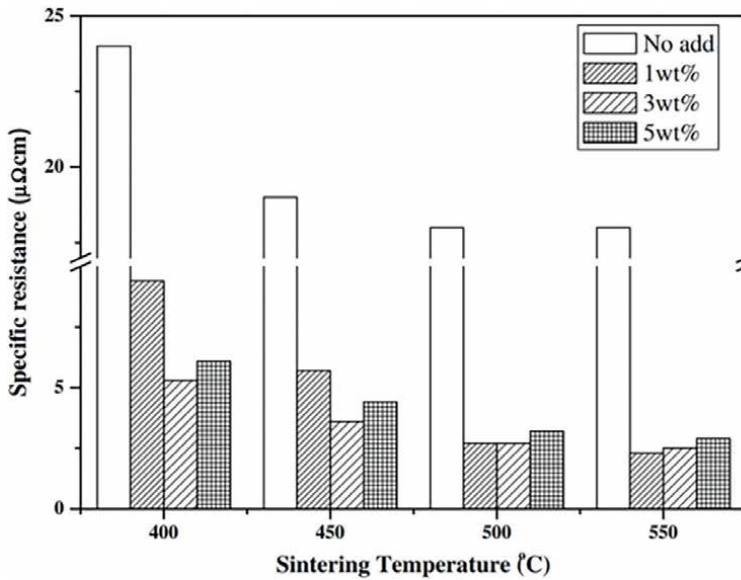


Figure 5. Specific resistance of silver conducting thick films as a function of sintering temperature and content of glass additive.

dispersing glass frit. This shows that the composite power has the effect of improving conductivity by enhancing the density of the electrode.

Although glass frit can be advantageous in facilitating sintering, it is an amorphous oxide, and should be applied in a minimum amount. Therefore, studies have been reported on the content of glass compared to Ag. Since composite powders can ideally disperse glass and Ag, a previous study observed the density of the electrode according to the glass wt.% through SEM. Further, the effect of glass content on the heat treatment temperature for the electrode was also investigated [24]. As shown in **Figure 4**, an increase in the glass content had a positive effect on the electrode density improvement, and the lowest glass content varied depending on the post-heat treatment temperature. In the results of this study, 5.3 and 2.3 $\mu\Omega\cdot\text{cm}$ showed the lowest resistivity values at post-treatment temperatures of 400 and 550°C, respectively, as shown in **Figure 5**. Moreover, the glass content was 3 wt.% and 1 wt.%.

4. Air stable coated copper powder

Ag powder has high utility, but the price of precious metal raw materials is high. Thus, the demand for metals to replace Ag is continuously increasing [25, 26]. Copper, which is relatively inexpensive and has low resistivity, can be used as an alternative, but low atmospheric stability is a major problem. In addition, as the size decreases, the specific surface area increases, and thus, the oxidation problem becomes more pronounced.

In order to solve this problem, efforts have been made to improve atmospheric stability by coating surfactants, conductive polymers, silver, titanium, silica, etc. [27–35]. However, such attempts have led to lowering the conductivity. Further, the method of coating the copper surface with metal requires an additional coating

process after synthesizing the copper powder, which increases the production cost in industrial applications. In addition, these methods present a difficulty in realizing uniform coating.

In this study, a technique for synthesizing coated copper composite particles using the spray pyrolysis process was studied in order to solve problems such as low atmospheric stability, complicated process, and uniform coating. The Cu composite particles developed in this study were prepared into a mixed solution by simultaneously adding copper nitrate trihydrate and silver nitrate salt for producing Ag-coated Cu powder when preparing the precursor solution to be input to the droplet generating device. And hydrogen mixed gas was used as carrier gas for reduction and synthesizing silver-coated copper powder [36]. The melting points of Ag and Cu are 962 and 1084°C, respectively. The results of this study showed that when the synthesis was conducted at 900°C, Cu remained in the core, and Ag was uniformly pushed to the surface. This is because Ag with a lower melting point has relatively better mobility. **Figure 6** shows the result of evaluating the air stability of these uncoated particles, after being left in the atmosphere for 1 month. The uncoated bare Cu powder developed substantial surface irregularities due to oxidation, and its HRTEM elemental profile showed that the oxygen peak on the surface was relatively higher than that on the inside. Further, as shown in **Figure 7**, the surface analysis of the coated particles after 1 month showed smooth characteristics similar to the initial stage, and the HRTEM analysis showed lattice spacing (Ag on the surface and Cu on the core). The elemental profile also confirmed atmospheric stability, showing relatively high Ag on the surface and no major change in oxygen peak. **Figure 8a** shows the sheet resistances of the electrode according to the Ag content of the Ag-coated Cu electrode layer. All samples were sintered at 700°C for 10 min under N₂ atmosphere. In **Figure 8a**, the sheet resistance value showed the lowest value of 2 mΩ square⁻¹ when Ag was 15 wt.%, which showed the characteristic that the porosity of the electrode was low, as shown in **Figure 8c**. When Ag was as high as 50 wt.%, large pores were exhibited due to the high mobility of Ag, and the sheet resistance value increased.

Glass-coated Cu particles have been proposed as another structure for synthesizing particles with improved atmospheric stability and electrode properties [37]. In the reported study, one-pot synthesis was performed using the spray pyrolysis process in the same manner as the previously shown process. To prepare glass-coated copper particles, The precursor solution was obtained by combining copper nitrate trihydrate

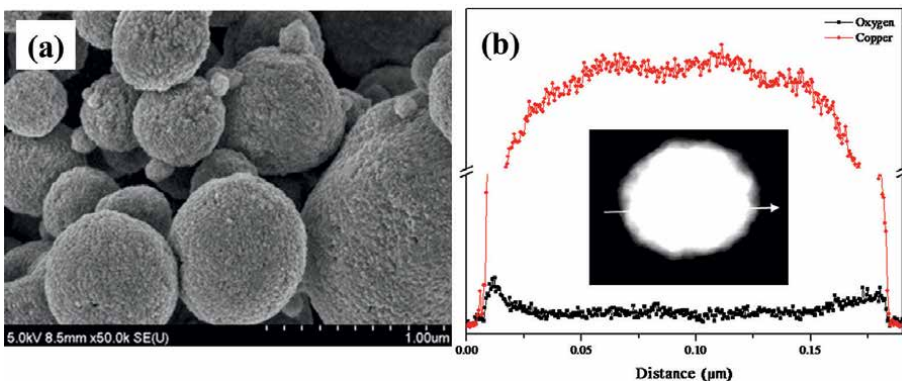


Figure 6. (a) SEM image, (b) element profile of bare copper particles after 1-month exposure to air [36].

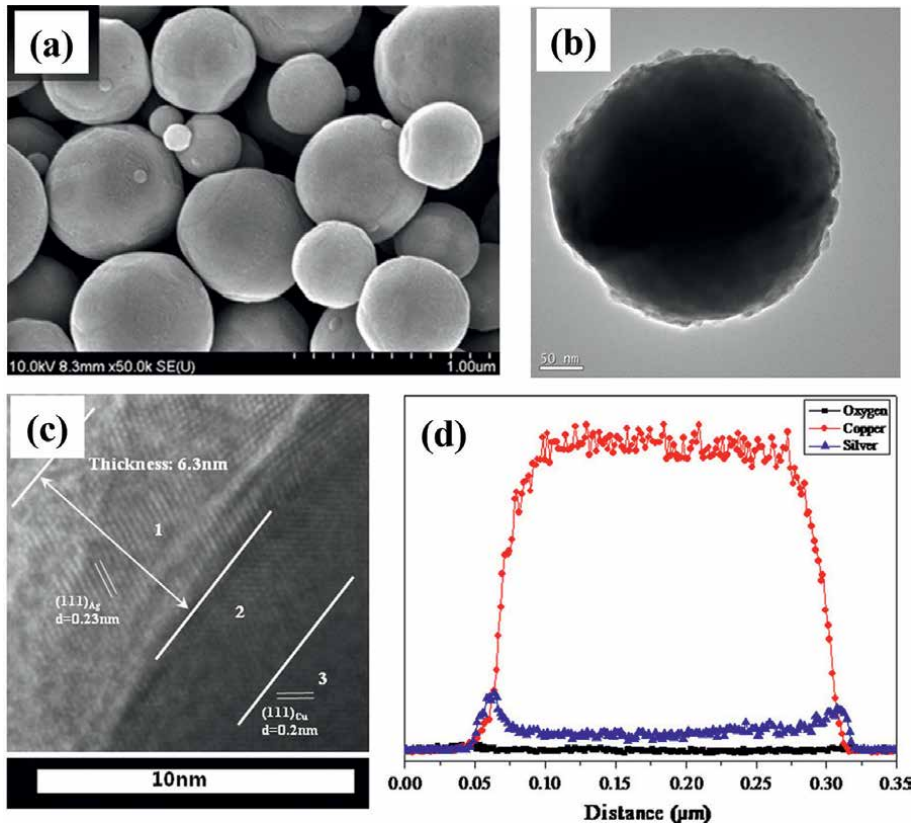


Figure 7. (a) SEM, (b) TEM, (c) HRTEM images of 20 wt.% silver coated copper, and (d) element profile across the particle diameter direction. The sample was exposed to air for 1 month [36].

($\text{Cu}(\text{NO}_3)_2 \cdot 3\text{H}_2\text{O}$), barium carbonate (BaCO_3), tetraethyl orthosilicate ($\text{SiC}_8\text{H}_{20}\text{O}_4$), and boric acid (H_3BO_3). The content of the glass precursors in the Cu@BBS particles was varied such that the final weight portion of the glass comprised 0.5–10 wt% of the Cu.

In the Cu electrode, the glass material also serves as an inorganic binder, helping the electrode sinter to increase the density of the electrode, and as an auxiliary agent to improve the electrode conductivity. It simultaneously acts as an inorganic binder and passivation to derive two positive effects in the case of Cu, enabling the synthesis of Cu particles without an additional process, which provides several advantages for mass production.

Figure 9 shows the synthesis process of Cu@BBS particles synthesized in the core-shell structure by the one-pot spray pyrolysis process. It was analyzed that CuO_x is changed to Cu during dry pyrolysis in a reducing atmosphere, and the materials constituting BBS that are not easily reduced are formed into BBS glass. Then, Cu is pushed to the center, and BBS glass is pushed to the surface due to the difference in melting point.

As shown in **Figure 10**, the surface of the synthesized particles was uniformly coated, and the coating layer was amorphous. In addition, the resistance values were compared by forming an electrode using the powder before and after coating, and the Cu and Cu@BBS particles exposure to air for 1 month, followed by heat treatment. As a result, the resistance values of bare Cu and Cu@BBS particles were lowered to 5.1 and

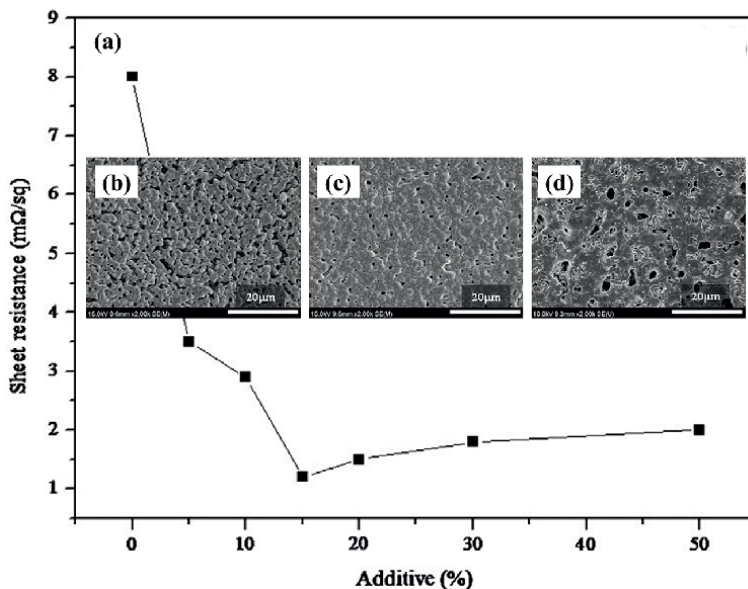


Figure 8. (a) Sheet resistance of conducting films obtained from silver-coated copper particles with various loadings of silver, sintered at 700°C for 10 min in N₂ atmosphere. SEM photographs of surface section of the prepared conductive films obtained from (b) bare copper, (c) 15 wt.%, and (d) 50 wt.% silver-coated particles [36].

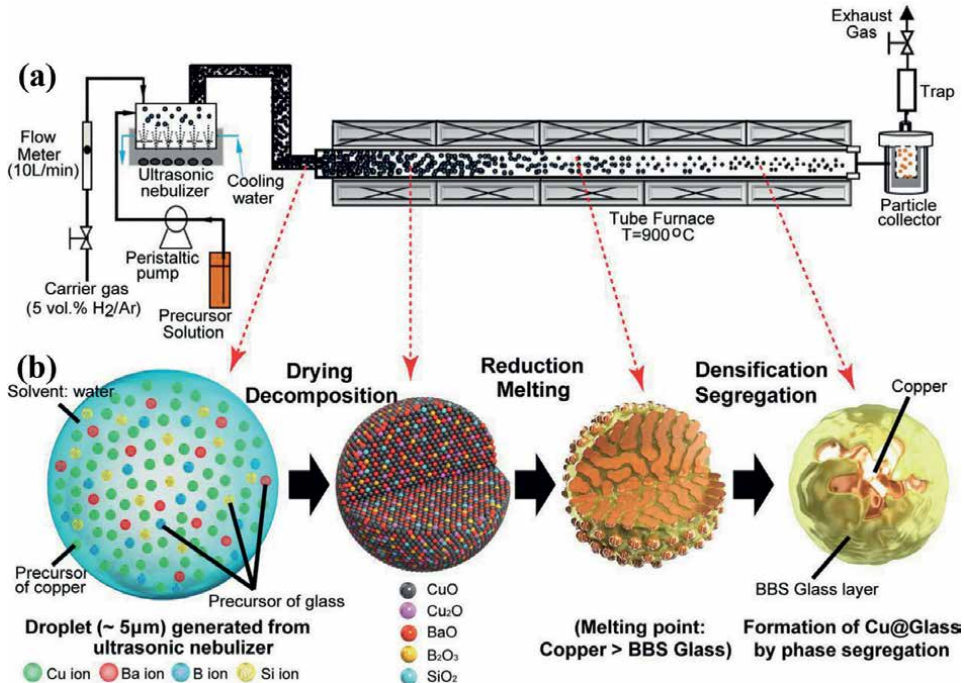


Figure 9. (a) Experimental setup for ultrasonic spray pyrolysis used in the current investigation. (b) Formation of BBS glass-coated copper particles by phase segregation [37].

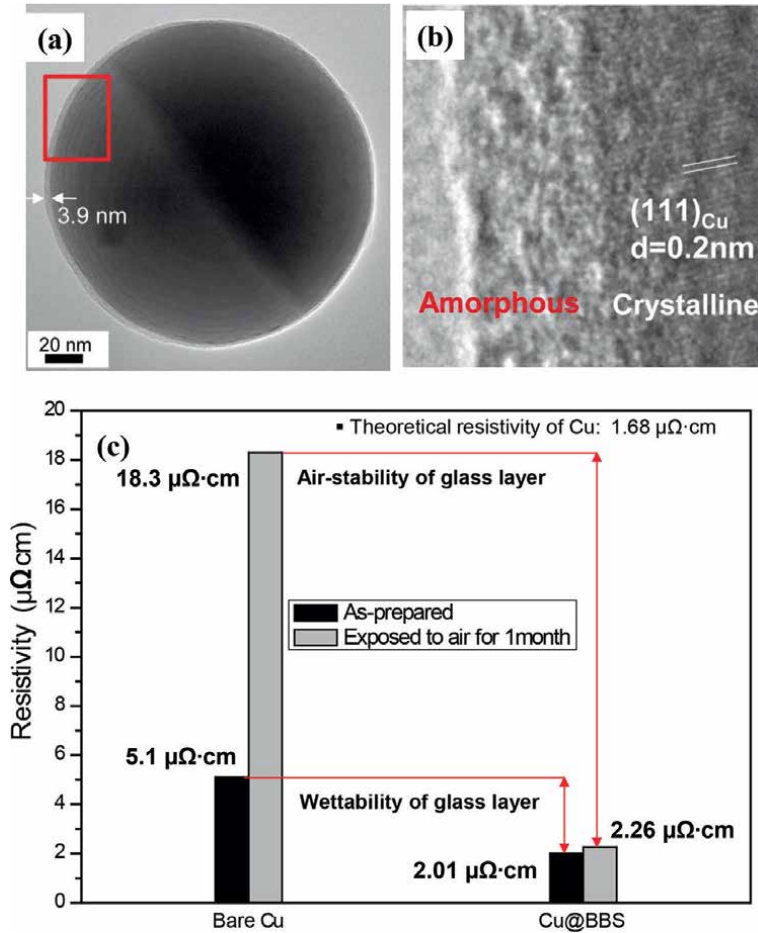


Figure 10. (a) Transmission electron microscopy (TEM) images of Cu@BBS particles (b) high-resolution TEM image magnified from the red box in (a) showing the amorphous coating layer and (c) resistivities of Cu conductive films based on bare Cu particles and Cu@BBS particles (measured after sintering at 800°C for 10 min under N_2 atmosphere) [37].

2.01 $\mu\Omega\cdot\text{cm}$, respectively, and those for the electrodes formed after 1 month of exposure were 18.3 and 2.26 $\mu\Omega\cdot\text{cm}$, respectively. As a result, the resistivity of bare Cu particles and Cu@BBS particles was lowered to 5.1 and 2.01 $\mu\Omega\cdot\text{cm}$, respectively, and after 1 month of exposure, these values were 18.3 and 2.26 $\mu\Omega\cdot\text{cm}$, respectively. Thus, the resistivity of the electrode comprising bare Cu increased by approximately three times or more than that of the existing electrode, while the Cu@BBS particle showed similar resistivity and presented improved atmospheric stability and electrode characteristics.

5. Conclusions

The ultrasonic spray pyrolysis process simultaneously utilizes the advantages of the bottom-up, liquid-phase, and gas phase methods. It involves the steps of placing the desired raw material in a solvent to prepare a solution, generating fine droplets using

an ultrasonic generator, and passing through a high-temperature heating furnace to synthesize particles within seconds via thermal decomposition. Since the process uses a solution by adding a desired metal salt, it is possible to uniformly distribute the material of the desired composition in a single particle. Furthermore, it is an advantageous process for synthesizing particles of complex structures that are difficult to synthesize top-down in one-pot through only process control of fine metal composite particles.

In this chapter, the process of synthesizing Ag and Cu particles, which are mainly used as electrodes, with glass, one of the electrode components, and the process of synthesizing silver-coated copper powder are summarized. All the composite electrode powders showed the advantage of synthesis in the same process as the electrode powder manufacturing process without a coating layer, and all of the samples showed superior electrical properties and atmospheric stability compared to bare powders.

From the results presented in this chapter, it can be inferred that the ultrasonic spray pyrolysis process can be used to synthesize not only single metals, but also various types of composite metal powders utilizing differences in density and melting point.

Acknowledgements

This research was supported by the National Research Council of Science & Technology (NST) grant by the Korea government (MSIT) (No. CAP22081-000) and the Ministry of Trade, Industry & Energy (MOTIE) of the Republic of Korea under grant (No. 20011040).

Conflict of interest


The authors declare no conflict of interest.

Author details

Hye Young Koo* and Dahee Park
Department of Metal Powder, Powder Materials Division, Korea Institute of Materials Science (KIMS), Changwon, Republic of Korea

*Address all correspondence to: hykoo@kims.re.kr

IntechOpen

© 2022 The Author(s). Licensee IntechOpen. This chapter is distributed under the terms of the Creative Commons Attribution License (<http://creativecommons.org/licenses/by/3.0>), which permits unrestricted use, distribution, and reproduction in any medium, provided the original work is properly cited. 

References

- [1] Walsh F. Electrode reactions in metal finishing. Transactions of the IMF. 2017;**69**:107-110
- [2] Al-Namil D, Khoury E, Patra D. Solid-state green synthesis of Ag NPs: Higher temperature harvests larger Ag NPs but smaller size has better catalytic reduction reaction. Scientific Reports. 2019;**9**:15212
- [3] Zhao Q, Feng G, Jiang F, Lan S, Chen J, Liu M, et al. Comparison of Fe₂TiO₅/C photocatalysts synthesized via a nonhydrolytic sol-gel method and solid-state reaction method. RSC Advances. 2020;**10**:43762-43772
- [4] Kumari S, Kumar A, Kumar V, Dubey S, Goyal P, Kumar S, et al. Structural, dielectric and ferroelectric properties of Cu²⁺- and Cu²⁺/Bi³⁺-doped BCZT lead-free ceramics: A comparative study. Journal of Materials Science. 2021;**32**:16900-16915
- [5] Watanabe M, Muto M, Abe Y, Kaneko T, Toda A, Uematsu K, et al. Synthesis of red-emissive CaV₂O₆ Nanophosphor via a water assisted solid state reaction method. ECS Journal of Solid State Science and Technology. 2021;**10**:106010
- [6] Barik S, Gogoi K, Sahoo S, Kim HS, Hajra A. Lead-free perovskite Bi_{1/2}(Na_{1/4}Li_{1/4})TiO₃: Investigation on structural, electrical properties, and device application. Journal of Materials Science: Materials in Electronics. 2021;**32**:4629-4638
- [7] Sahoo D, Kumar B, Sinha J, Ghosh S, Roy S, Kaviraj B. Cost effective liquid phase exfoliation of MoS₂ nanosheets and photocatalytic activity for wastewater treatment enforced by visible light. Scientific Reports. 2020;**10**:10759
- [8] Lee S, Heo J, Im S. Large-scale synthesis of uniform PbI₂(DMSO) complex powder by solvent extraction method for efficient metal halide perovskite solar cells. American Chemical Society. 2020;**12**:8233-8239
- [9] Kawashita M, Tsuneyama S, Miyaji F, Kokubo T, Kozuka H, Yamamoto K. Antibacterial silver-containing silica glass prepared by sol-gel method. Biomaterials. 2020;**21**:393-398
- [10] Wu S, Cui T, Hu Q, Yin F, Feng Q, Zhou S, et al. Mixing solvothermal synthesis nickel selenide on the surface of graphene for high-efficiency asymmetric supercapacitors. Synthetic Metals. 2020;**268**:116490
- [11] You J, Hossain M, Luo Z. Synthesis of 2D transition metal dichalcogenides by chemical vapor deposition with controlled layer number and morphology. Nano Convergence. 2018;**5**:26
- [12] Okada M, Okada N, Chang W, Endo T, Ando A, Shimizu T, et al. Gas-source CVD growth of atomic layered WS₂ from WF₆ and H₂S precursors with high grain size uniformity. Scientific Reports. 2019;**9**:17678
- [13] Drosos C, Vernardou D. Advancements, challenges and prospects of chemical vapour pressure at atmospheric pressure on vanadium dioxide structures. Materials. 2018;**11**:384
- [14] Li J, Wu Z, Xu Y, Pei Y, Wang G. Stability analysis of multi process parameters for metal-organic chemical vapor deposition reaction cavity. Molecules. 2019;**24**:876
- [15] Bouzakis K, Michailidis N. Physical vapor deposition. CIRP Encyclopedia of Production Engineering. 2019:1308-1316

- [16] Perrotta A, Werzer O, Coclite A. Strategies for drug encapsulation and controlled delivery based on vapor-phase deposited thin film. *Advanced Engineering Materials*. 2017;**20**:1700639
- [17] Jung D, Koo H, Kang Y. The effects of glass powders prepared by spray pyrolysis on the structures and conductivities of silver electrode. *Materials Chemistry and Physics*. 2010;**124**:959-963
- [18] Vest R. Materials science of thick film technology. *Ceramic Bulletin*. 1986;**65**:631-636
- [19] Rane S, Seth T, Phatak G, Amalnerkar D, Das B. Influence of surfactants treatment on silver powder and its thick films. *Materials Letters*. 2000;**57**:3096-3100
- [20] Provance J, Allison K. Particle size effects on viscosity of silver pastes—a manufacturer's view. *Proceedings of the International Symposium of Hybrid Microelectronics*. 1983;**6**:60-65
- [21] Jung D, Koo H, Kang Y. Composite conducting powders with core-shell structure as the new concept of electrode material. *Colloids and Surfaces A: Physicochemical and Engineering Aspects*. 2010;**360**:69-73
- [22] Koo H, Kim J, Ko Y, Jung D, Kang Y. Preparation of silver-glass composite powder and conducting film. *Journal of the Ceramic Society of Japan*. 2010;**118**:353-356
- [23] Koo H, Yi J, Ko Y, Kim J, Kang Y. Firing characteristics of size-controlled silver-glass composite powders prepared by spray pyrolysis. *Powder Technology*. 2010;**198**:347-353
- [24] Jung D, Koo H, Kang Y. Electrical and morphological properties of conducting layers formed from the silver-glass composite conducting powders prepared by spray pyrolysis. *Journal of Colloid and Interface Science*. 2010;**343**:1-6
- [25] Wu S. Preparation of fine copper powder using ascorbic acid as reducing agent and its application in MLCC. *Materials Letters*. 2007;**61**:1125-1129
- [26] Pollet M, Marinell S. Copper electrodes multilayer ceramic capacitors Part I: The dielectric composition. *Journal of Materials Science*. 2004;**39**:1943-1958
- [27] Bateni M, Ashrafizadeh F, Szpunar J, Drew J. Improving the tribological behavior of copper through novel Ti-Cu intermetallic coatings. *Wear*. 2002;**253**:626-639
- [28] Kanninen P, Johans C, Merta J, Kontturi K. Influence of ligand structure on the stability and oxidation of copper nanoparticles. *Journal of Colloid and Interface Science*. 2008;**318**:88-95
- [29] Kobayashi Y, Sakuraba T. Silica-coating of metallic copper nanoparticles in aqueous solution. *Colloids and Surfaces A: Physicochemical and Engineering Aspects*. 2008;**317**:756-759
- [30] Wang J, Yang J, Wan C, Du K, Xie J, Xu N. Sulfur composite cathode materials for rechargeable lithium batteries. *Advanced Functional Materials*. 2003;**13**:487-492
- [31] Kim C, Lee G, Rhee C, Lee M. Expedient low-temperature sintering of copper nanoparticles with thin defective carbon shells. *Nanoscale*. 2015;**7**:6627-6635
- [32] Son Y, Jang J, Kang M, Ahn S, Lee C. Application of flash-light sintering method to flexible inkjet printing using anti-oxidant copper nanoparticles. *Thin Solid Films*. 2018;**656**:61-67
- [33] Chung W, Hwang Y, Lee S, Kim H. Electrical wire explosion process of copper/silver hybrid nano-particle ink

and its sintering via flash white light to achieve high electrical conductivity. *Nanotechnology*. 2016;**27**:205704

[34] Shiomi S, Kawamori M, Yagi S, Matsubara E. One-pot synthesis of silica-coated copper nanoparticles with high chemical and thermal stability. *Journal of Colloid and Interface Science*. 2015;**460**:47-54

[35] Magdassi S, Grouchko M, Kamyshny A. Copper nanoparticles for printed electronics: Routes towards achieving oxidation stability. *Materials*. 2010;**3**:4626-4638

[36] Jung D, Lee H, Kang Y, Park S. Air-stable silver-coated copper particles of sub-micrometer size. *Journal of Colloid and Interface Science*. 2011;**364**:574-581

[37] Jung D, Koo H, Wang S, Park S, Kang Y. Ultrasonic spray pyrolysis for air-stable copper particles and their conductive films. *Acta Materialia*. 2021;**206**:116569

Chapter 2

Features of the Powder Application in Direct Laser Deposition Technology

Marina Gushchina, Olga Klimova-Korsmik and Gleb Turichin

Abstract

The chapter presents the basic aspects of the use of metal powders in one of the main additive technologies—direct laser deposition (DLD). Direct laser deposition refers to a group of direct energy deposition (DED) methods and is analogous to Laser Metal Deposition (LMD) technology. The main requirements applied to DLD used metal powders are analyzed and substantiated. The influence of the basic properties of the powders on the quality of the deposited samples is demonstrated. An example of incoming quality control of powders, allowing its application in DLD technology, is presented. The results of experimental research on obtaining quality control samples for the most used metallic materials are presented. The results of structure and properties studies for the main groups of alloys based on iron, nickel, and titanium are shown. The potential for manufacturing products for various areas of industry using DLD has been demonstrated.

Keywords: direct energy deposition, direct laser deposition, metal powder, structure, properties, alloys

1. Introduction

Additive manufacturing (AM) is one of the fastest growing areas today [1–3]. This interest is dictated by the high demand from the part of the industry. However, now there are high requirements for additive manufacturing products, including AM technology. It should be noted that despite the prospects of introducing AM technologies into real production and substitution for some subtractive methods for the real application, a high number of parameters that affect the quality of the final product still have to be considered [4]. Laser-Direct Energy Deposition (L-DED) is one of the examples such AM technology. Many researchers at the stage of commissioning technology into real parts production have difficulties that are associated with the necessity for many parameters control, which can be divided into the following groups:

- machine specification (laser type, shielding gas, laser beam radius, alarms, and interlocks, etc.)

- process and environmental state (thermal history, substrate temperature distribution, laser state, chamber pressure and temperature distribution, melt pool temperature, etc.)
- Powder/material (impurity, size distribution, shape, powder type, fraction, etc.);
- Process parameters (power, powder feed rate, scanning speed, etc.);
- Motion and process control (dwell time, hatch spacing, build strategy, layer thickness, etc.).

All of the abovementioned parameters have a high impact on the quality and performance of laser-based AM technologies [5, 6]. Errors in selected parameters or inadequate control can lead to large losses of both operating hours of expensive equipment and large volumes of powder material. This chapter discusses the basic requirements of L-DED technology for initial powder materials, as well as the basic powder control methods that can minimize the number of defective products during additive manufacturing.

Figure 1 shows the main characteristics of metal powders that can affect the quality of the laser direct energy deposited products. The combination of these factors can significantly affect the properties of the items and its performance. The properties of products are reduced not only because of the formation of defects such as pores and cracks, but also because of changes in the phase composition and structure of the metals and its alloys. Impurities such as hydrogen, oxygen, nitrogen as interstitial atoms change the crystal lattice parameters and lead to a change in the phase composition, as well as to a significant embrittlement of the material.

A high hydrogen content, for example, can lead to the formation of cold cracks. In titanium alloys, a high oxygen content not only increases the hardness and leads to the formation of titanium oxides, but also, as a stabilizer of the α -phase can change the phase composition of the alloy. A change in the content of niobium in the Inconel 718 alloy leads to a change in the phase composition, since niobium can form many phases (gamma, delta phase, carbides, and leaves phase). Depending on the concentrations of niobium, a different quantitative relation of phases can be formed in deposited Inconel 718 alloy. This significantly affects the properties of the final product.

All properties of powders, both physical and chemical, depend on the manufacturing process and the parameters of the corresponding process.

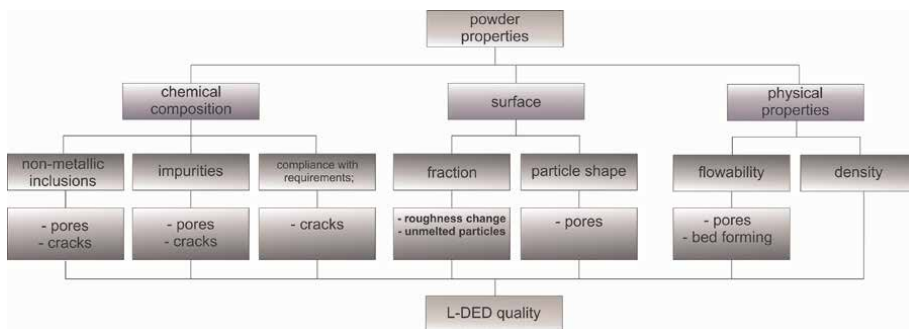


Figure 1. Influence of metal powders characteristics on defects formation in L-DED materials.

Among the various production methods, several technologies are usable for the manufacturing of powders suitable for L-DED technology.

1. Gas atomization (GA). There are few melting mechanisms for gas atomization. Inductive heating (**Figure 2a**), plasma torch (**Figure 2b**), rotating rod (EIGA) (**Figure 2c**);
2. Plasma atomization, PA (**Figure 2d**);
3. Plasma Rotating Electrode Process, PREP (**Figure 2e**);
4. Water atomization (WA).

Powders produced by water atomization technology are limited used for L-DED technologies. Reason is that water-atomized powders are non-spherical and are usually have an irregular shape with an average particle size of about 100 μm [8].

In gas atomization, liquid metal is dispersed with using a high-speed gas stream (air, nitrogen, argon, or helium). In gas atomization, the metal or alloy is melted in a melting chamber filled with an inert gas. Molten metal poured in a controlled mode through a sprayer. Jet of inert gas is broken the flow of liquid metal into spherical powder particles under high pressure, which solidify in flight (**Figure 2a–c**). The particles have the same chemical composition as the molten stream. Gas atomization processes can be classified by the heating method as well as by the design of the nozzle used. The most commonly encountered nozzle types in the production of metal powders for additive manufacturing are the free-fall nozzle, the close coupled nozzle, and the De Laval nozzle. The combination of parameters of gas atomization processes largely determines the shape and size of powder particles. The pressure of the spheroidizing gas determines the size of the powder and the quality of its surface. Gas atomization methods are characterized by the satellites formation on the particles surface. Satellites are formed during the collision of small particles with partially molten larger particles during gas circulation in the spray chamber. Another disadvantage of gas atomization methods is the possibility of forming internal porosity, which is formed because of the capture of the gas used for sputtering by liquid metal [9]. Satellites and

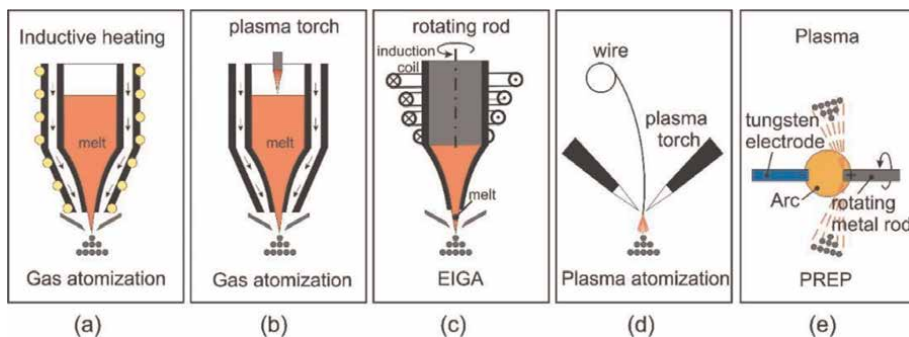


Figure 2. Metal powders manufacturing technologies: (a) gas atomization with inductive heating, (b) gas atomization with plasma torch, (c) electrode inert gas atomization, (d) plasma atomization, and (e) plasma rotating electrode process [7].

internal pores during the AM process are also inherited in deposited material from gas-atomized powders that lead to reduction of the mechanical properties. In addition, some studies have shown that an increase in the number of satellites can affect the behavior of particles in the gas flow, which also leads to the formation of porosity in the metal [10].

Plasma atomization technology realizes by plasma melting of the wire. The spherical powder particles are formed when molten droplets are cooled [11]. The main parameter of plasma atomization process is the thermal power of the plasma arc, which depends on the current force and the rate of plasma gas supply. In addition, the quality of the PA metal powders depends on the cooling rate, which is determined both by the thermophysical characteristics of the sprayed material and its heat exchange with the environment surrounding the particle [12, 13]. Powders manufactured by plasma atomization (PA) are free from satellites and have a higher quality than powders got by gas atomization. The PA disadvantage is the relatively low process of productivity compared to gas atomization. This technology is most promising for the production of titanium and titanium alloys powders [14, 15]. Another minor disadvantage is only powder alloys available as wire can be made by PA.

Plasma rotating electrode process (PREP) is a centrifugal atomization method [16]. The metal melted at the end of the rod billet moves to the periphery under the action of centrifugal forces. As the metal accumulates in the rod surface, the centrifugal forces acting on the melt increase and at some point exceed the surface tension forces. The metal is sprayed. Flow rate of the melt influence on the mode of drop formation.

It is also worth mentioning that the particle size can be controlled by the electrical current applied to the plasma arc and the distance between the tip of the plasma gun and the end of the rod. In PREP, the droplets fly radially away from the metal surface in a centrifugal force; in other words, it moves in order, so the chance of collisions of droplets and particles to form satellites is very low.

Figure 3 shows powder surface for AM depending on manufacturing technology.

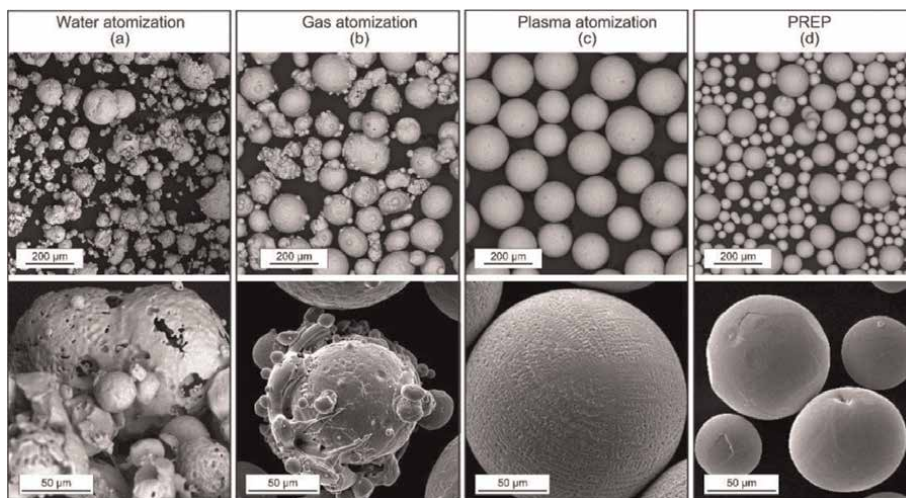


Figure 3. Powder surface: (a) iron powders produced by water atomization; (b) 316 L powders produced by gas atomization; (c) 316 L powders produced by plasma atomization; and (d) Ti-6Al-4 V powders produced by plasma rotating electrode process.

2. Metal powder materials for the DLD process, requirements

2.1 Size distribution

Various methods can determine the size distribution of powders, including using the laser analyzer (**Figure 4a**), measurement of the particle's projection from scanning electron microscope (**Figure 4b–d**) or optical microscope images or by sieve analysis.

Predominantly, the size distribution should be normal unimodal. However, in some powders, a bimodal distribution can be observed (**Figure 4c**). Experimental works have shown that there is no effect of the bimodality of the powder distribution on the change in the properties and structure of the L-DED material. However, several features were found related to the influence on the structure and formation of defects of such parameters as the width of the powder fraction and particle size.

For L-DED technology, usually use following particle size distribution: 45–100 μm , 100–150 μm , 100–180 μm . Wide range of the fractional composition is possible depending on the manufacturer. However, it is not recommended to use powders smaller than 45 microns, because of a decrease in the flow rate of powder. Such powders lead to contamination of the supply system and the formation of various defects subsequently. The conducted studies also showed that the powder fraction has influenced the surface roughness [17]. **Figure 5** shows the influence of the powder fraction on the surface quality.

For L-DED technology, usually use following particle size distribution: 45–100 μm , 100–150 μm , 100–180 μm . Wide range of the fractional compositions are possible depending on the manufacturer. Nevertheless, it is not recommended to use powders smaller than 45 microns, due to a decrease in flow rate of powder. Such powders lead to contamination of the supply system and the formation of various defects subsequently. The conducted studies also showed that the powder fraction has an effect on the surface roughness [17]. **Figure 5** shows the influence of the powder fraction on the surface quality. Sample surface deposited from Ti-6Al-4 V powder with (a) fraction 45–90 μm (b) fraction 106–180 μm .

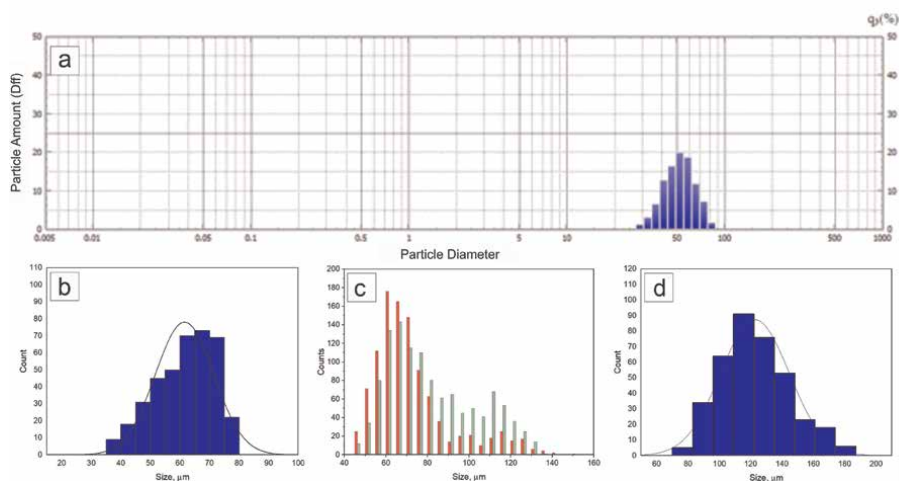


Figure 4. Particle size distribution of nickel-based superalloy: (a) laser diffraction method (fraction of 45–100 μm), and (b–d) graphical method with using SEM images.

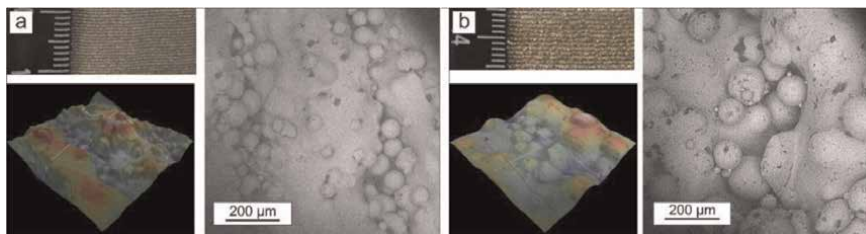


Figure 5. Sample surface deposited from Ti-6Al-4 V powder with (a) fraction 45–90 μm, and (b) fraction 106–180 μm.

It can be seen from **Figure 5** that the layers formed from coarse powder are less stable, while the roughness of thin walls is higher (**Figure 5b**). At the same time, the fine particles create a stable melt pool, resulting in a smoother surface (**Figure 5a**). In addition, large particles themselves introduce roughness equal to their size. An increase in roughness has negative effect the mechanical properties. That influence was shown experimentally. The effect of surface quality on mechanical properties was demonstrated on thin walls. Part of deposited walls was tested without treatment while the other part was polished mechanically. **Table 1** shows the deposition mode used to obtain the experimental samples. **Figure 6** presents test specimens.

The samples before and after treatment were tested on uniaxial tension on a Zwick installation model Roell Z100. Test temperature was 26°C. The results of investigation are presented in **Table 2**. It can be seen from **Table 2** that the roughness has a significant influence on the results of mechanical tests.

Laser power, W	Speed, mm/s	Laser spot size, mm	Gas flow, l/min	Layer height, mm
1300	25	3	12.5	0.5

Table 1. L-DED mode parameters for Ti-6Al-4 V sample production for mechanical tests.



Figure 6. Sample with roughness removed (top) and untreated (bottom).

Before treatment		After treatment	
Tensile strength, MPa	Elongation, %	Tensile strength, MPa	Elongation, %
1007	6	1050	8

Table 2. Mechanical test results of L-DED Ti-6Al-4 V samples.

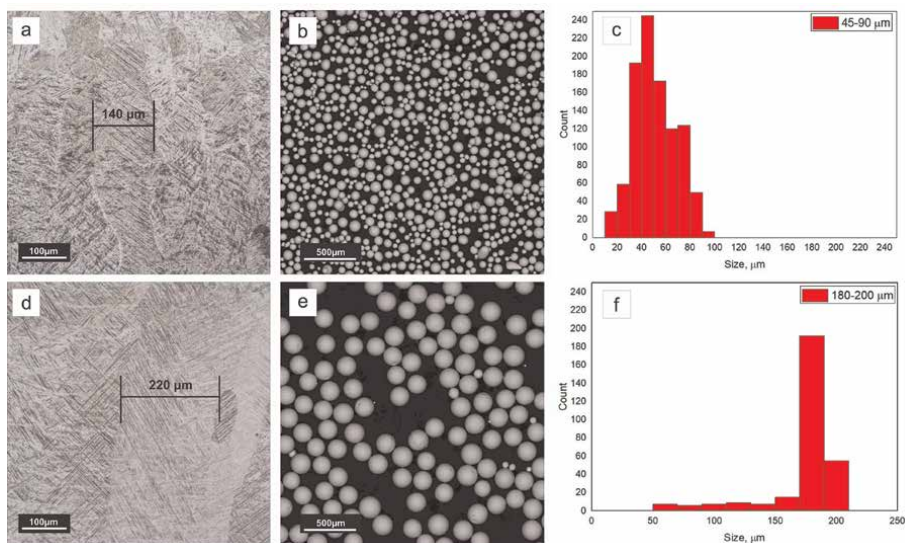


Figure 7. L-DED Ti-6Al-4 V alloy: (a) microstructure of L-DED Ti-6Al-4 V obtained from 45 to 100 μm fraction powder, (b) SEM image of powder, fraction 45–100 μm, (c) size distribution of powder, fraction 45–100 μm, (d) microstructure of L-DED Ti-6Al-4 V obtained from 45 to 100 μm fraction powder, (e) SEM image of powder, fraction 180–200 μm, and (f) size distribution of powder, fraction 180–200 μm.

Particle size distribution also can affect the size factor of the structure, for example, the grain size. In the work of the authors present results [18] of powder size influence on the grain size for L-DED Ti-6Al-4 V titanium alloy (**Figure 7**). Wide powder fraction is also undesirable for an L-DED process. For example, a low laser power level can be not enough for melting particles that are too large. That led to incomplete particle melting, which can, among other things, cause effects spatter formation or powder island formation [19]. The presence of high-heat oxide films on the particle surface has the same effect. Such processes reduce the stability of the L-DED process and reduce the quality of the deposited parts as well as the process efficiency.

2.2 Chemical composition

The chemical composition of powder determines the structure and phase composition of the systems under consideration. As a rule, deviations from the required composition and content of alloying elements can lead not only to a change in the required properties, but also to a decrease in the material's processability for the L-DED process. For example, an excess of vanadium content in the Ti-6Al-4 V titanium alloy can lead to a decrease in ductility during deposition, which in turn leads to premature failure of the product during printing.

A change in the content of the main alloying elements in 321 stainless steel leads to a change in the content of phases in the structure of the deposited material. **Table 1** shows the chemical composition of steel 321 powders of different batches (labeled #1 and #2). The nickel content in powder #2 is lower than those required by the ASTM A276-98b 321 [20].

It can be seen on the X-ray diffraction pattern of the powder, the content for powder # 2 of the austenite phase was 55% and ferrite was 45% (**Figure 8**).

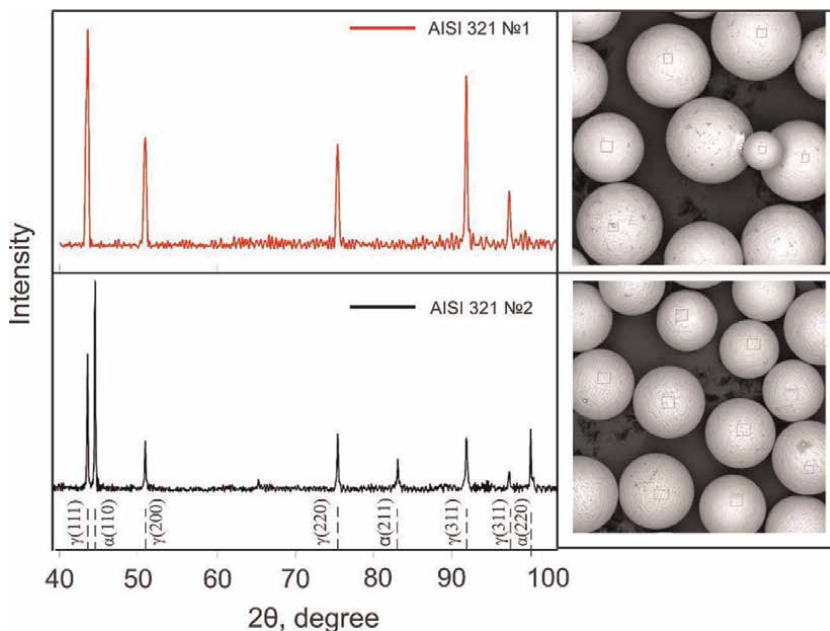


Figure 8.
X-ray diffraction pattern of the deposited 321 steel sample.

Sample	Chemical composition, wt. %									
	C	Si	Mn	Ni	S	P	Cr	Ti	Cu	Fe
321 #1	0,03	0,42	1,06	9,65	0,0018	0,028	18,16	0,52	0,03	bal.
321 #2	0,044	0,41	1,21	8,06	0,013	0,036	18,30			
ASTM A276-98b 321 [*]	≤0,08	≤1	≤2	9–12	≤0,03	≤0,045	17–19	≤0,8	≤0,3	

^{*}ASTM A276-06 Standard Specification for Stainless Steel Bars and Shapes.

Table 3.
Chemical composition of 321 steel powders.

An increase in the content of the ferrite leads to a change in the properties of the material, including magnetic ones. This behavior, among other things, leads to powder flow in the supply systems is deviated because of the increased magnetization of small powder particles. In this case, the stability of the deposition process and wall formation is impaired (**Table 3**).

Impurities also have a significant affect the structure during the deposition process, not only the main alloying elements content. For example, a slight increase in the iron content in a nickel superalloy leads to the crack's formation in the deposited material. An increase in the iron content in the alloy, even a slight one, can lead to the formation of the Laves phase, which in turn leads to the formation of cracks [21, 22].

It was experimentally shown that in EP 648 nickel superalloy powders, an increase in the iron content (**Table 4**) led to the formation of cracks in L-DED material, as shown on **Figure 9**. Samples #1, #2, #3 were deposited using similar process parameters. The formation of porosity, as will be shown in the next chapter, is caused by internal porosity and the presence of satellites on the surface of the powders.

Chemical composition, wt. %								
	Al	Ti	Cr	Fe	Ni	Nb	Mo	W
1	0,93	0,76	34,50	—	55,65	0,51	2,74	4,90
2	0,85	0,98	33,99	0,55	54,50	0,78	2,86	5,49
3	0,98	1,03	33,79	0,32	53,32	0,78	2,44	4,84

Table 4.
 Chemical composition of different EP 648 superalloy powders.

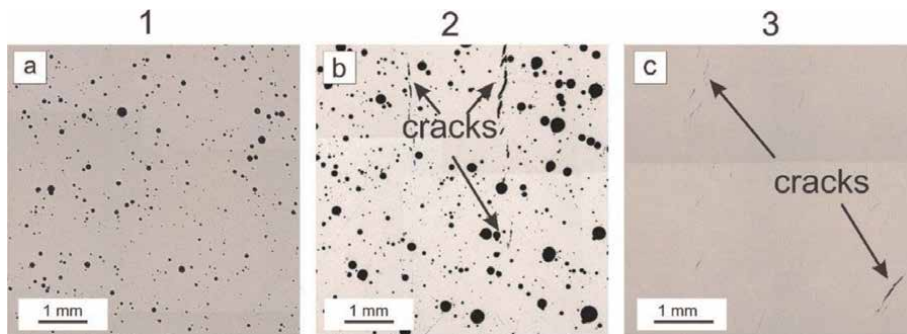


Figure 9.
 Optical image of L-DED EP 648 superalloy microstructure obtained from powder with different Fe content.

Harmful impurities of light elements also have a significant impact on the quality of the material.

2.3 Foreign inclusions on the surface of the particles and inside

During the production of powders, various non-metallic inclusions can form, both on the surface of the particles and inside. Such inclusions can have different properties and, to varying degrees, affect the formation of the structure and the properties of the deposition material.

Figure 10 shows microstructure and chemical composition measuring results of powder and L-DED material got with using scanning electron microscopy (SEM).

The results demonstrate the heredity of inclusions (presumably Cr_2O_3) that are found in the initial powders on the structure of the deposited material. Such inclusions are formed during the powder manufacturing process and can have a negative effect on the properties of the finished material. Therefore, their control is very important in the powder's study.

2.4 Powder particle shape

The recommended and desired shape of the powder particles is spherical or subspherical. This form of particles allows to get the best fluidity in L-DED systems. **Figure 11** shows the classification of particles according to their possible shape. As a rule, the particle sphericity can be expressed numerically in terms of the ratio of the maximum particle length to the minimum (l_{\max}/l_{\min}).

In practice, powders with an angular shape but larger than $45\ \mu\text{m}$ are also used and show good results for L-DED process of composite materials (**Figure 12**) [23].

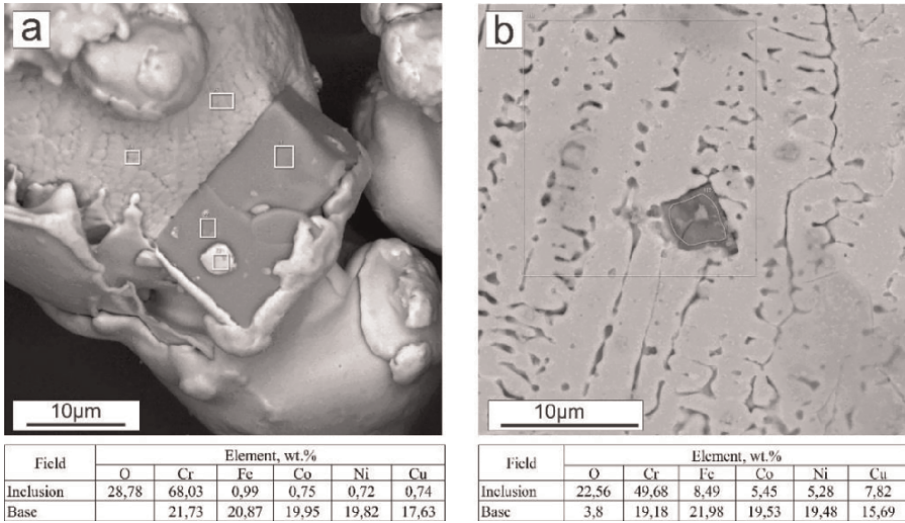


Figure 10. SEM (BSE) image and EDS analyze the results of high-entropy alloy for (a) powder surface, and (b) L-DED structure.

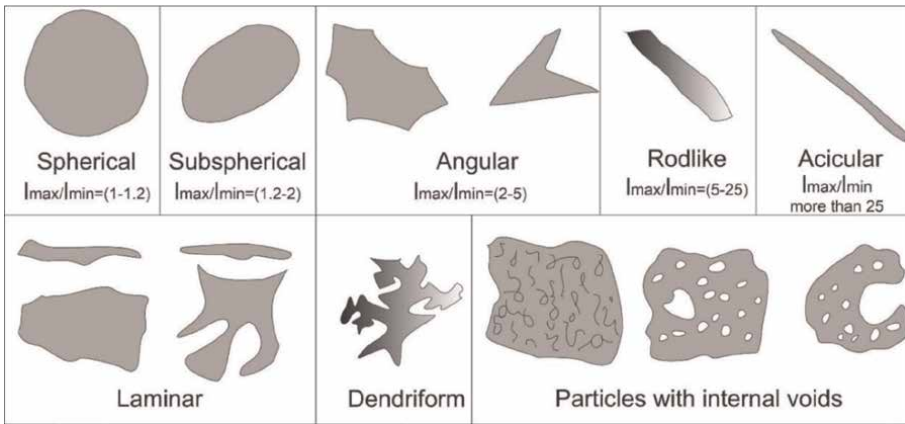


Figure 11. Powder particle form classification.

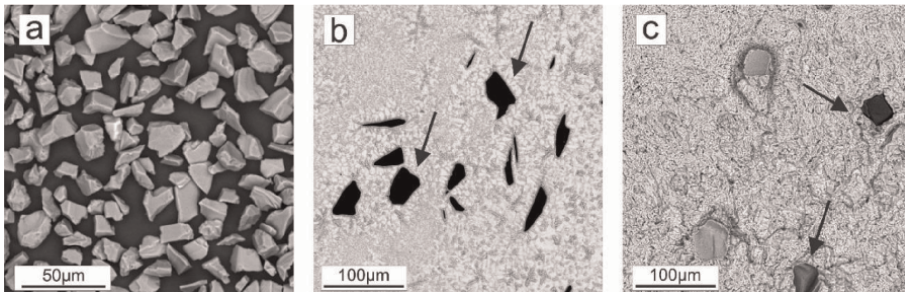


Figure 12. L-DED of metal composite material Ti-6Al-4 V/SiC SEM image (a) SiC powder, (b) cross section of deposited composite, and (c) fracture surface of deposited composite.

Powders that are spherical or subspherical and have large number of satellites or internal porosity on the surface are undesirable to use. It has been repeatedly experimentally shown that such powders lead to the formation of porosity in L-DED samples to a large extent (**Figure 3**). Powders consisting entirely of rod-like, acicular, laminar, and dendriform (irregular) particles are unacceptable for L-DED technology. However, particles of this shape are found in spherical powders and its content should be only 10% of such particles in the total mass of the powder is acceptable.

2.5 Incoming powder inspection

Based on experimental data incoming powder inspection methodology was developed that can use quality control. Incoming powder inspection should be carried out under the documentation developed by the technology manufacturer.

Incoming powder inspection includes several main steps:

1. Acceptance of powder and verification of regulatory documentation. Checking the condition of the package (container) for the absence of mechanical damage and traces of unauthorized opening of the package;
2. Checking the presence and legibility of the marking, the conformity of the name and marking on the product (packaging), and the information in the enclosed documents.
3. Quality control of metal powders.

Quality control of metal powder is an integral part at the initial stage of items development for L-DED process.

The main stages of powder quality control include:

- Powder Particle Surface Analysis.
 - Particle size measurement (determination of particle size distribution).
 - Determining the shape of the particles.
 - Determination of particle defects and their description.
- Analysis of the chemical composition.
 - Determination of the main alloying elements.
 - Determination of the impurities content.
- Powder Fluidity Determination.
- Determination of water content.

SEM or optical images usually using for control of powder particle surface. Particle size measurement methods were discussed in the Section 1.1. Shape of particles is determinate according to classification presented in **Figure 11**, Section 1.4. The number of particles of spherical and other shapes is determined by agreement between the consumer and the supplier.

Particle defects include deviations from the spherical shape of the particles, the presence of satellites, craters, and oxidation spots on the surface, the presence of pores, voids, and inclusions in the particles.

Determination of the main alloying elements is carried out using energy-dispersive spectrometry under ISO 22309:2011 «Microbeam analysis—Quantitative analysis using energy-dispersive spectrometry (EDS) for elements with an atomic number of 11 (Na) or above [24]. Quantitative analysis requires preparation of a cross section of powder particles to provide a plane-parallel surface perpendicularly placed to the electron beam. The content of the main alloying elements of the powder alloys must comply with the requirements of regulatory documents (ASTM, ISO, GOST, technical conditions, etc.).

Determination of the content of oxygen, nitrogen, hydrogen, carbon, sulfur elements is carried out under ASTM E1019-11 [25]. The content of O₂, N₂, and H₂ must comply with the requirements of ASTM, ISO, GOST, technical conditions, etc. If the content of O₂, N₂, and H₂ is not regulated for the powder alloy, the concentrations of these elements are included in the report for information. The content of sulfur and carbon is carried out for individual grades of high-alloy steels and high-temperature nickel alloys under the relevant standards (for example, ASTM-E1941 [26]).

Powder flow rate can be evaluated according to ASTM B213-20 [27]. The recommended powder flow rate for L-DED equipment and laser cladding should not exceed 30 s.

3. Laser direct energy deposition for standard construction alloys

3.1 Steels

At the moment, iron-based alloys are actively used in additive manufacturing. Steels are mainly used in the form of a spherical powder in the DED and PBF technologies [28] and also in the form of a wire in the EBM [29], WAAM [30]. The application of the austenitic stainless steels class for additive manufacturing has been the most attractive. Martensitic transformation in these steels is absent and that allows to use them almost with no problems during deposition in an air atmosphere [31]. It should be noted that the requirements for the chemical composition of steels, especially for the content of light impurity, should be strictly kept. It is also should control oxygen and trying to minimize it in powders to a level of 0.02%. When the porosity high level is observed in L-DED material, it is worth checking a sulfur, phosphorus, and nitrogen content.

Other steels classes, such as high-tensile-strength carbon steels and maraging steels, require more attention before using for manufacturing by the L-DED process. Development of post-processing is also necessary for that steel class. Steels with a high carbon content, which in turn are most often limited or difficult-to-weld, require careful selection of the process mode to avoid cracking because of a high level of stress during uneven heating and cooling [2, 32, 33]. Additional heating may also be required to equalize the temperature field [34].

Steels used for welded structures are best suited for the additive process.

To select the heat treatment parameters for a particular as-deposited alloy, one should rely on data already developed for other technological processes (rolling, casting). However, standard parameters should be considered as a starting point and research should be carried out to correct the modes of annealing, hardening, and tempering. Parameters such as temperature, time, cooling rate may change up or down.

3.1.1 Input control of steel

In order to use steel powder in additive manufacturing, the first step is to ensure that the powder meets several requirements listed in the incoming inspection chapter. Powders got by the PREP and PA methods have the best quality. However, PREP is practically not used to produce steel powders because of the high cost of the process. Plasma atomization will, of course, be the best option (**Figure 13**).

It is worth paying attention to the content of impurities of light elements. The content of sulfur and phosphorus should be only 0.01 wt.%. The oxygen content is often not regulated by guidelines; however, for steel powders for additive manufacturing, it should be controlled, its content in steel should not exceed 0.02 wt.%. An increased amount of oxygen indicates the presence of oxide inclusions on the surface and inside the powder.

As a result, inclusions that were on the surface and inside the powders will be detected in the structure of the grown samples. Their localization may be different, but mainly at the boundary of the layers.

The high content of satellites in steel powders got by gas atomization can lead to the appearance of defects in the form of pores and non-fusion in steels. In general, gas porosity is the most common defect found in steels got with the help of L-DED. However, a small number of individual pores or an accumulation of small pores practically does not affect the mechanical characteristics.

During L-DED of non-stainless steels, it is worth using vacuum drying of powders. In the case of suspected high humidity of powders, for example, in the presence of condensate inside the can or low fluidity of powders in the absence of many satellites on the surface of the particles, it is worthwhile to vacuum dry the powders between 120 and 140°C and at least under low vacuum.

3.2 Nickel-based alloys

Nickel-based alloys are distributed the same as steel for additive manufacturing. But developed nickel alloys quantity list is the leading position for application in industry compared to the nomenclature of steels [35–37]. Main interests are heat-resistant nickel alloys [38–40], the microstructure of which is a complexly alloyed γ -solid solution of nickel and dispersed particles based on intermetallic compounds (γ' -phase $\text{Ni}_3(\text{Al},\text{Ti})$ and γ'' -phase Ni_3Nb).

Multicomponent alloying of the γ -solution and γ' -phase/ γ'' -phase is carried out in such a way as to ensure high phase and structural stability of the alloy [41]. Using

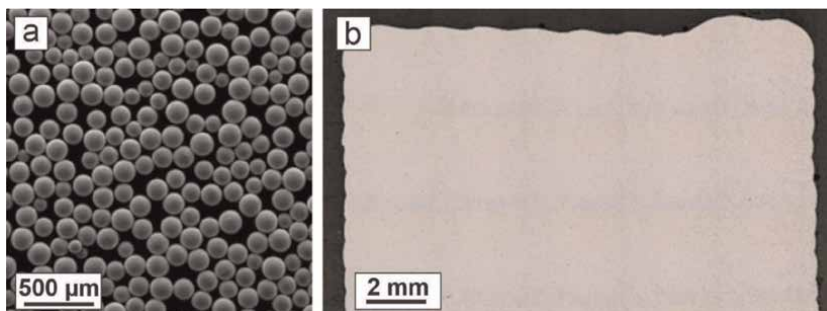


Figure 13.
Additive manufacturing of 304 steel (a) plasma atomized powder, and (b) L-DED 304 steel.

concentrated energy sources introduces their own characteristics into the processes of structure formation and significantly affects the mechanical properties of the material. Al, Ti, Nb, and Ta are responsible for the content of the γ' -phase and γ'' -phase in nickel alloys. However, for materials used in additive manufacturing, it is recommended to use additional heating, for example, induction, if the total amount of Al, Ti in them exceeds 5 wt.%.

Strengthening of the γ -solid solution is achieved by alloying with using Co, Cr, Fe, Mo, W, Ta, Re. Strengthening of the grain boundaries is achieved by separating MC-type carbides based on Nb, Ti, Zr, as well as by selective microalloying of B, N, and rare earth metals (REM Y, La, Ce). High heat resistance of the material, grain boundary precipitates should be globular, have a size of 1 μm or less, and be dispersed along the grain boundaries, but at the same time they should not form a continuous grid. The possibility of formation of undesirable phases (σ -, μ -phases, Laves phases) should be minimized.

Despite the above difficulties, the use of additive methods for the manufacturing of products from heat-resistant nickel alloys is justified.

3.2.1 Input control of nickel-based alloys

Before using nickel-based alloy powders in additive manufacturing, the first step is to ensure that the powder corresponds a number of requirements listed in the incoming inspection chapter. Exclusively PREP and PA processes to avoid high oxide content (**Figure 14**) should produce nickel alloy powders with high Al and Ti content.

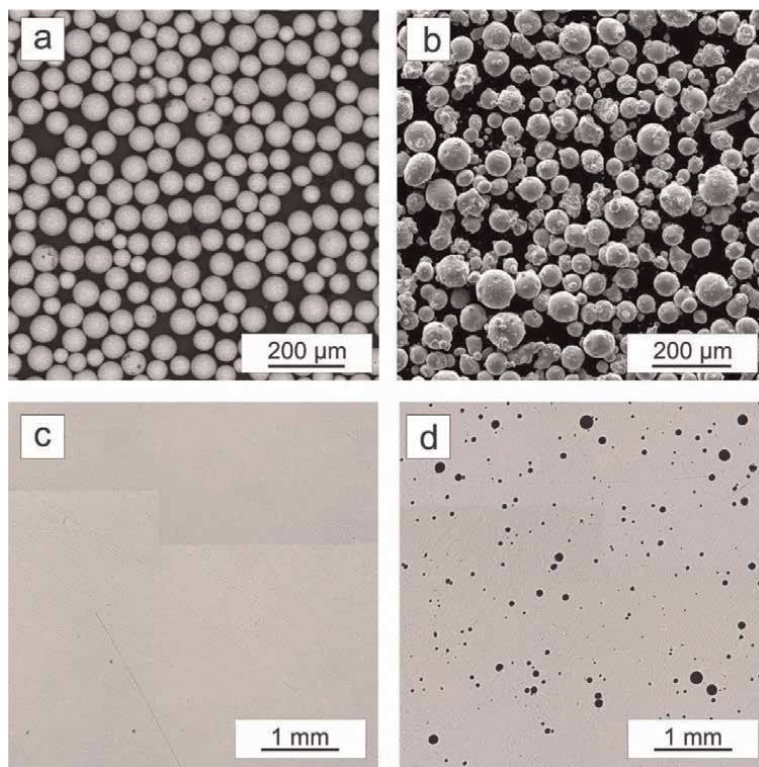


Figure 14. *Inconel 718 powder (a) PREP, (b) GA, (c) L-DED microstructure from PREP powder, and (d) L-DED microstructure from GA powder.*

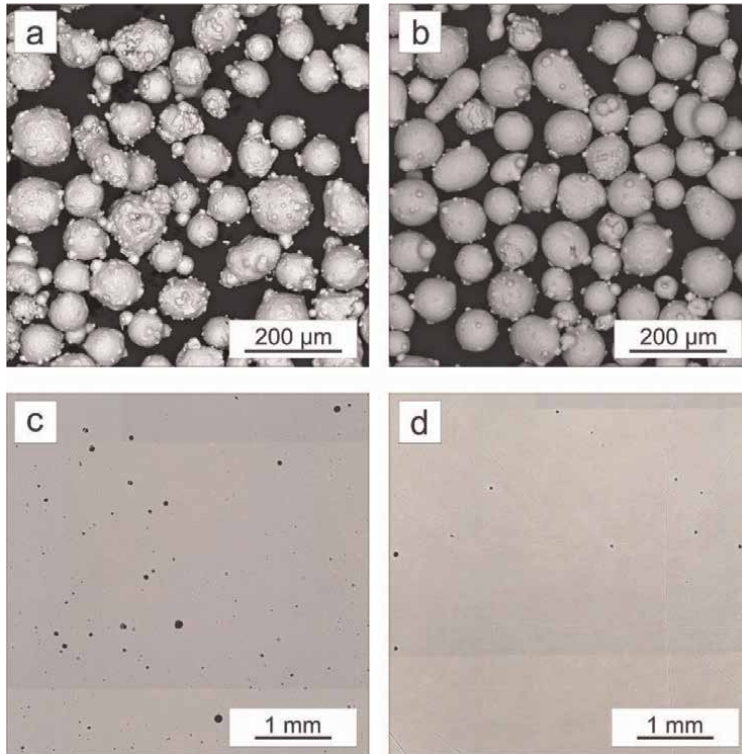


Figure 15. Nickel-based alloy EP648 powder (a) IGA, (b) EIGA, (c) L-DED microstructure from IGA powder, and (d) L-DED microstructure from EIGA powder.

Defects in Nickel Alloys got by the L-DED technology.

For nickel alloys, as well as for steels, the content of some light elements should be strictly regulated: no more than 0.01 wt.% S and P, no more than 0.02% O. An increased amount of oxygen is usually associated with the presence of oxide inclusions on the surface and inside the powder. As a result, inclusions that were on the surface and inside the powders will be detected in the structure of the deposited samples. Their localization can be different, but mainly they are localized at the layer's boundaries. Also, the internal porosity of the powder, which occurs in powders got by the GA method, will negatively affect (Figure 15).

3.3 Titanium alloys

Wide interest in the titanium and titanium alloys associated with a unique range of characteristics. At the same time, they are difficult to process. As a result, they are widely used in additive manufacturing.

Features of titanium alloys also appear in the production of powders. Only inert gases can be used for protection and as energy carriers in the production of powders.

The most studied and widespread titanium alloy is Ti-6Al-4 V alloy [41–44]. However, there are also works by the authors on the use of other titanium powders in additive manufacturing [45–47].

Many studies have shown dependence of the L-DED process parameters on the structure and properties formation in titanium alloys [48–51].

3.3.1 Input control of titanium alloys

The main attention in the input control of titanium powders is paid to the content of light impurities. Input control is carried out under the methodology presented in Section 1.6. Also, basic information on titanium powders can be found in ASTM B988–13 [51].

Opposed from steels and nickel superalloys, the low thermal conductivity of titanium causes the particle size of the powder to affect the grain size in the L-DED structure. This was shown in Section 1.1.

Since powders of titanium alloys are got by plasma atomization and PREP, they are characterized by a low content of satellites on the surface. The main problem encountered in such powders is the variation in chemical composition.

Figure 16 shows SEM images of the surface of various powders, numbered respectively A1, A2, B1, B2.

The results of the study of L-DED material obtained from the considered powders showed that the most significant influence is exerted by light impurities in the powder [18]. **Figure 17** shows that powder B1 has an increased hydrogen content. This high hydrogen content has a significant effect on increasing hardness and reducing ductility, and porosity has also been found in the structure.

As can be seen from the L-DED figures, a sample made from a powder with a high hydrogen content has low ductility. No significant effect of the fraction on the properties was found.

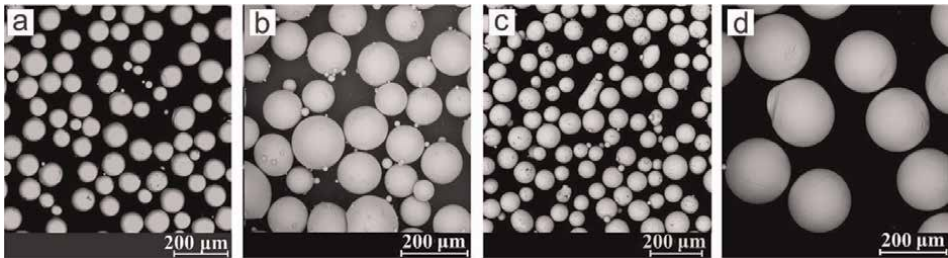


Figure 16. Images of the powder surface from a scanning electron microscope in BSE mode: (a) A1 powder (45–100 μm), (b) A2 powder (106–180 μm), (c) B1 powder (45–100 μm), and (d) B2 powder (160–200 μm).

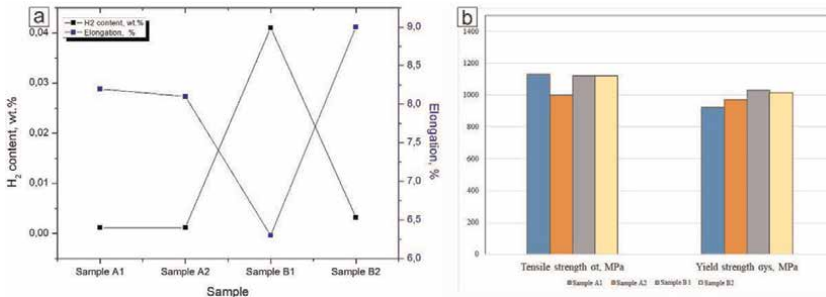


Figure 17. Light impurities content influence on properties of L-DED Ti-6Al-4 V.

3.4 Mechanical properties of L-DED material got from various powders

Practical experience in implementing of L-DED technology has demonstrated good results in terms of material properties in a wide range of nomenclature. **Tables 5–7** present the chemical composition of powders that have been successfully used to produce products using the L-DED technology.

Alloy	C	S	P	Mn	Cr	Si	Ni	Cu	V	Mo	W	Fe
09CrNi2MoCu	0.08	<0.01	0.0015	0.6	0.7	0.37	2.2	0.7	0.15	0.35	0.03	base
06Cr15Ni4CuMo	0.06	0.015	0.015	0.9	15.5	0.40	4.4	1.5	—	0.28	—	
316 L	0.03	0.015	0.02	0.8	17	0.6	16	—	—	3	—	
08MnCuNiV	0.1	0.04	0.035	1	0.3	0,4	—	1.2	—	—	—	
28Cr3SiNiMoWV	0.31	<0.01	0.01	0.8	3.2	1.2	1.2	<0.15	0.15	0.5	1.2	
09Cr16Ni4Nb	0.12	0.015	0.03	0.5	16.5	0.6	4.5	0.3	0.2		0.2	
15-5P	0.07	0.03	0.04	1	15.5	1	5.5	4.5	—	—	—	

Table 5.
 Chemical composition of steel powders.

Alloy	Al	V	Zr	V	Mo	Fe	O	Si	C	N	H	Ti
Ti-7Al-2,5Zr-2,5 V-2Mo	7	2.5	2.5	2.5	2	0.25	0.15	0.15	0.1	0.05	0.015	base
Ti-6Al-4 V	6.8	5.3	—	5.3	—	0.6	0.2	0.1	0.1	0.05	0.015	
CP-Ti	—	—	—	—	—	0.25	0.2	0.1	0.07	0.04	0.01	
Ti-5Al-2 V	5	2,5	0.3	2.5	—	0.25	0.15	0.12	0.1	0.04	0.006	

Table 6.
 Chemical composition of titanium powders.

Alloy	Cr	Mo	Fe	Nb	W	Mn	Si	Al	Ti	C	B	V	Cu	Co	Ni
EI 698	13–16	2.8–3.2	<2	1.8–2.2	—	<0.4	<0.6	1.3–1.7	2.35–2.75	<0.08	—	—	—	—	base
Inconel 718	21	3.3	base	5.5	—	—	—	0.8	1.15	0.08	0.006	—	0.3	—	55
Inconel 738	16.3	2	0.5	1.1	2.8	0.2	0.3	3.7	3.7	0.2	0.015	—	—	9	base
EK 61	18.5	5	16	5.5		0.7	0.5	1.3	1	—	—	0.6			
BSh159	28	7.8	3	3.4		0.5	0.8	1.55		0.08	0.005	—	1		
EP 648	35	3.3	4		5.3	0.5	0.4	1.1	1.1	0.1	0.008	1.1			
Hynes 230	22	2	<3	0.5	14	0.5	0.4	0.3	0.1	0.1	0.015	—			
GS32	5	5	—	5	10	—	—	8	—	0.15	0.3	—		9.3	
Inconel 625	23	10	5	4,15	—	0.5	0.5	0.4	0.4	0.1	—	—	—	1	

Table 7.
 Chemical composition of nickel-based powders.

Most of the difficulties in deposition are solved by selecting technological parameters. The structure of L-DED materials has several features, but as a rule, heat treatment solves the problems that arise (**Table 8**).

Material	State	Tensile strength σ_B , MPa	Yield strength $\sigma_{0,2}$, MPa	Elongation δ , %	Powder
Steels					
09CrNi2MoCu	L-DED	685	616	21,5	Gas atomized
	L-DED + HT	665	598	21	Gas atomized
06Cr15Ni4CuMo	L-DED	1086	888	8,35	Gas atomized
	L-DED + HT	810	515	20	Gas atomized
08MnCuNiV	L-DED	755	725	14	Gas atomized
	L-DED + HT	517	444	26,5	Gas atomized
316 L	L-DED	602	427	48,5	Gas atomized
	L-DED + HT	575	392	66	Gas atomized
316 L	L-DED	607	409	48,4	Plasma atomized
	L-DED + HT	545	245	84,6	Plasma atomized
28Cr3SiNiMoWV	L-DED	1667,2	1068,9	11,3	Gas atomized
09Cr16Ni4Nb	L-DED	1451	1167	13,5	Gas atomized
15-5P	L-DED	1123	1088	12,5	Gas atomized
Titanium alloys					
Ti-7Al-2,5Zr-2,5 V-2Mo	L-DED	968,0	882,0	6,6	PREP
Ti-7Al-2,5Zr-2,5 V-2Mo	L-DED	1076,7	1056,7	1,4	Plasma atomized
	L-DED + HT	1159,2	1100,5	9,8	Plasma atomized
Ti-6Al-4 V	L-DED	1060	963	7	Plasma atomized
Ti-6Al-4 V	L-DED	1047	983	10,3	PREP
	L-DED + HT	1026	925	14,2	PREP
CP-Ti	L-DED	675	620	23,4	PREP
PT3V	L-DED	912	877	14,5	PREP
	L-DED + HT	872	834	15,3	PREP
Nickel-based alloy					
EI 698	L-DED	884	565	41	PREP
	L-DED + heat treatment	1100	781	24	PREP
Inconel 718	L-DED	452,4	339	19	PREP
	L-DED + HT	1303	1155	24,6	PREP
Inconel 625	L-DED	811,9	512,8	38,5	PREP

Material	State	Tensile strength σ_B , MPa	Yield strength $\sigma_{0,2}$, MPa	Elongation δ , %	Powder
ZhS32	L-DED	1353,0	1046,0	11,5	PREP
Hynes 230	L-DED	921,3	615,6	27,81	Inert Gas Atomizers
	L-DED + HT	922	429,2	31,92	Inert Gas Atomizers
Inconel 738	L-DED	1379	1088,9	6,44	PREP
EK61	L-DED	858	512	39,7	PREP
	L-DED HT	1152	886	29	PREP
Vsh159	L-DED	880	451	48,7	Inert Gas Atomizers
	L-DED HT	1195	921	9,6	Inert Gas Atomizers
EP 648	L-DED	781	476	38	PREP

Table 8.
 Mechanical properties of L-DED material.

4. Conclusion

Additive manufacturing is of profound interest for various industries. However, a large number of parameters that affect the quality of the final product limit the application at the moment. Including the initial powders properties have a significant influence on the quality L-DED materials. For the L-DED technology, powders manufactured by gas atomization, plasma atomization, and PREP technologies are most widely used. GA powders have a high amount of satellites on the surface, which can lead to porosity in as-deposited samples. Also, a deviation from the required chemical composition has a significant impact on the properties of products. Light impurities also affect the properties of the L-DED material.

To minimize the amount of rejects due to the properties of the powder, the main requirements for powders and the input control measures that must be implemented are considered.

Considering the high influence on the structure and properties of the material of the initial quality of the powder, a method for the input control of the powder is being developed.

Input control of powder for use as feedstock in L-DED technology includes:
 Particle size measurement (determination of particle size distribution).

- Determining the shape of the particles;
- Determination of particle defects and their description.

Analysis of the chemical composition:

- Determination of the main alloying elements;
- Determination of the impurities content.

Powder Fluidity Determination.


The totality of implementing measures to control the quality of the powder will reduce the number of defective products.

Author details

Marina Gushchina, Olga Klimova-Korsmik* and Gleb Turichin
Institute of Laser and Welding Technologies, St. Petersburg State Marine Technical
University, St. Petersburg, Russia

*Address all correspondence to: o.klimova@ltc.ru

IntechOpen

© 2023 The Author(s). Licensee IntechOpen. This chapter is distributed under the terms of the Creative Commons Attribution License (<http://creativecommons.org/licenses/by/3.0>), which permits unrestricted use, distribution, and reproduction in any medium, provided the original work is properly cited. 

References

- [1] Shapiro AA, Borgonia JP, Chen QN, Dillon RP, McEnerney B, Polit-Casillas R, et al. Additive manufacturing for aerospace flight applications. *Journal of Spacecraft and Rockets*. 2016;**53**(5): 952-959
- [2] Korsmik R, Tsybulskiy I, Rodionov A, Klimova-Korsmik O, Gogolukhina M, Ivanov S, et al. The approaches to design and manufacturing of large-sized marine machinery parts by direct laser deposition. *Procedia CIRP*. 2020;**94**: 298-303
- [3] Mahale RS, Shamanth V, Hemanth K, Nithin SK, Sharath PC, Shashanka R, et al. Processes and applications of metal additive manufacturing. *Materials Today: Proceedings*. 2022;**54**(2):228-233
- [4] Liu M, Kumar A, Bukkapatnam S, Kuttolamadom M. A review of the anomalies in directed energy deposition (DED) processes & potential solutions-part quality and defects. *Procedia Manufacturing*. 2021;**53**:507-518
- [5] Vildanov AM, Babkin KD, Alekseeva EV. Macro defects in direct laser deposition process. *Materials Today: Proceedings*. 2019;**30**(c):523-527
- [6] Wycisk E, Solbach A, Siddique S, Herzog D, Walther F, Emmelmann C. Effects of defects in laser additive manufactured Ti-6Al-4V on fatigue properties. *Physics Procedia*. 2014;**56**: 371-378
- [7] Dietrich S, Wunderer M, Huissel A, Zaeh MF. A new approach for a flexible powder production for additive manufacturing. *Procedia Manufacturing*. 2016;**6**:88-95
- [8] *Encyclopedia of Materials: Science and Technology* ISBN: 0-08-0431526 pp. 387±393 A. Lawley
- [9] Sun P, Fang ZZ, Zhang Y, Xia Y. Review of the methods for production of spherical Ti and Ti alloy powder. *JOM*. 2017;**69**:1853-1860
- [10] Iams AD, Gao MZ, Shetty A, Palmera TA. Influence of particle size on powder rheology and effects on mass flow during directed energy deposition additive manufacturing. *Powder Technology*. 2022;**396**:316-326
- [11] Ermakov SB. Regulation of powder particles shape and size at plasma spraying. *Vektor nauki Tolyattinskogo gosudarstvennogo universiteta*. 2021;**10**: 7-15. DOI: 10.18323/2073-5073-2021-1-7-15
- [12] Pan H, Ji H, Liang M, Zhou J, Li M. Size-dependent phase transformation during gas atomization process of Cu–Sn alloy. *Powders Materials*. 2019;**12**:245. DOI: 10.3390/ma12020245
- [13] Baskoro AS, Supriadi S, Dharmanto. Review on Plasma Atomizer Technology for Metal Powder MATEC Web of Conferences. IOP Publishing Ltd. Vol. 269. 2019. p. 05004. DOI: 10.1051/mateconf/201926905004
- [14] Xie B, Fan Y, Zhao S. Characterization of Ti6Al4V powders produced by different methods for selective laser melting. *Materials Research Express*. 2021;**8**:076510
- [15] Liu Z, Huang C, Gao C, Liu R, Chen J, Xiao Z. Characterization of Ti6Al4V powders produced by different methods for selective electron beam melting. *Journal of Mining and Metallurgy*. 2019;**55**(1):121-128. Section B: Metallurgy
- [16] Cui Y, Zhao Y, Numata H, Bian H, Wako K, Yamanaka K, et al. Effects of

plasma rotating electrode process parameters on the particle size distribution and microstructure of Ti-6Al-4 V alloy powder. *Powder Technology*. 2020;**376**:363-372

[17] Shalnova SA, Klimova-Korsmik OG, Sklyar MO. Influence of the roughness on the mechanical properties of Ti-6Al-4V products prepared by direct laser deposition technology. *Solid State Phenomena*. 2018;**284**(SSP):312-318

[18] Gushchina MO, Shalnova SA, Gerasimov NI, Lebedeva NV, Klimov GG. Comparison of titanium powders and products manufactured by the direct laser deposition method key. *Engineering Materials*. 2019;**822**:473-480

[19] Prasad HS, Brueckner F, Kaplana AFH. Powder incorporation and spatter formation in high deposition rate blown powder directed energy deposition. *Additive Manufacturing*. 2020;**35**:101413

[20] A276-98b 321 Standard Specification for Stainless Steel Bars and Shapes. United States: ASTM International; 2015

[21] Yu LX, Sun WR, Zhang ZB, Zhang WH, Liu F, Xin X, et al. The role of primary laves phase on the crack initiation and propagation in thermo Span alloy. *Materials Research Innovations*. 2015;**19**(Sup 4):S68-S72

[22] Stein F, Leineweber A. Laves phases: A review of their functional and structural applications and an improved fundamental understanding of stability and properties. *Journal of Materials Science*. 2021;**56**:5321-5427

[23] Shalnova SA, Volosevich DV, Sannikovally MI, Magidov S, Mikhaylovskiy KV, Turichin GA, et al. Direct energy deposition of SiC

reinforced Ti-6Al-4V metal matrix composites: Structure and mechanical properties. *Ceramics International*. 2022; **48**(23):35076-35084

[24] ISO 22309:2011 «Microbeam analysis—Quantitative analysis using energy-dispersive spectrometry (EDS) for elements with an atomic number of 11 (Na) or above»

[25] E1019-11 Standard Test Methods for Determination of Carbon, Sulfur, Nitrogen, and Oxygen in Steel, Iron, Nickel, and Cobalt Alloys by Various Combustion and Fusion Techniques by the Method of Reducing Melting. United States: ASTM International; 2018

[26] E1941 Standard Test Method for Determination of Carbon in Refractory and Reactive Metals and Their Alloys by Combustion Analysis; United States: ASTM International; 2016

[27] ASTM. B213-20 Standard Test Methods for Flow Rate of Metal Powders Using the Hall Flowmeter Funnel. United States: ASTM International; 2020

[28] Feng J, Zhang P, Jia Z, Yu Z, Fang C, Yan H, et al. Microstructures and mechanical properties of reduced activation ferritic/martensitic steel fabricated by laser melting deposition. *Fusion Engineering and Design*. 2021; **173**:112865

[29] Lin Z, Dadbakhsh S, Rashid A. Developing processing windows for powder pre-heating in electron beam melting. *Journal of Manufacturing Processes*. 2022;**83**:180-191

[30] Guo L, Zhang L, Andersson J, Ojo O. Additive manufacturing of 18% nickel maraging steels: Defect, structure and mechanical properties: A review. *Journal of Materials Science & Technology*. 2022;**120**:227-252

- [31] Wang D, Cheng D, Zhou Z, Wang W, Hu B, Xie Y, et al. Effect of laser power on the microstructure and properties of additive manufactured 17-4 PH stainless steel in different fabrication atmosphere. *Materials Science and Engineering: A*. 2022;**839**:142846
- [32] Sergei Y, Ivanov, Vildanov A, Golovin PA, Artinov A, Karpov I. Effect of inter-layer dwell time on distortion and residual stresses of laser metal deposited wall. *Key Engineering Materials*. 2019;**822**:445-451
- [33] Golovin PA, Vildanov AM, Babkin KD, Ivanov SY, Topalov IK. Distortion prevention of axisymmetric parts during laser metal deposition. *Journal of Physics: Conference Series*. 2018;**1109**:012065
- [34] Dalae MT, Gloor L, Leinenbach C, Wegener K. Experimental and numerical study of the influence of induction heating process on build rates induction heating-assisted laser direct metal deposition (IH-DMD). *Surface and Coatings Technology*. 2020;**384**:125275
- [35] Shao S, Khonsari MM, Guo S, Meng WJ, Lib N. Overview: Additive manufacturing enabled accelerated design of Ni-based alloys for improved fatigue life. *Additive Manufacturing*. 2019;**29**:100779
- [36] Shahwaz M, Nath P, Sen I. Critical review on the microstructure and mechanical properties correlation of additively manufactured nickel-based superalloys. *Journal of Alloys and Compounds*. 2022;**907**:164530
- [37] Park J-U, Jun S-Y, Lee BH, Jang JH, Lee B-S, Lee H-J, et al. Alloy design of Ni-based superalloy with high γ' volume fraction suitable for additive manufacturing and its deformation behavior. *Additive Manufacturing*. 2022;**52**:102680
- [38] Ghiaasiaan R, Poudel A, Ahmad N, Muhammad M, Gradl PR, Shao S, et al. Room temperature mechanical properties of additively manufactured Ni-base superalloys: A comparative study. *Procedia Structural Integrity*. 2022;**38**:109-115
- [39] Rashkovets M, Nikulina A, Turichin G, Klimova-Korsmik O, Sklyar M. Microstructure and phase composition of Ni-based alloy obtained by high-speed direct laser deposition. *Journal of Materials Engineering and Performance*. 2018;**27**(12):6398-6406
- [40] Chuan Guo, Gan Lia, Sheng Li, Xiaogang Hu, Hongxing Lu, Xinggang Li, Zhen Xu, Yuhan Chen, Qingqing Li, Jian Lu, Qiang Zhu, Additive Manufacturing of Ni-based Superalloys: Residual Stress, Mechanisms of Crack Formation and Strategies for Crack Inhibition, *Nano Materials Science*. KeAi Communications Co. Ltd; 2022. In press
- [41] Clare AT, Mishra RS, Merklein M, Tan H, Todd I, Chechik L, et al. Alloy design and adaptation for additive manufacture. *Journal of Materials Processing Technology*. 2022;**299**:117358
- [42] Palmer TA, Beese AM. Anisotropic tensile behavior of Ti-6Al-4V components fabricated with directed energy deposition additive manufacturing/B.E. Carroll. *Acta Materialia*. 2015;**87**:309-320
- [43] Yu J. Marleen rombouts gert maes filip motmans material properties of Ti6Al4 V parts produced by laser metal deposition. *Physics Procedia*. 2012;**39**: 416-424
- [44] Wua X, Liang J, Junf Mei C, Mitchell PS, Goodwin W. Voice

microstructures of laser-deposited Ti-6Al-4V 5. *Materials and Design*. 2004;25(2):137-144

[45] Guo S, Meng Q, Liao G, Hu L, Zhaon X. Microstructural evolution and mechanical behavior of metastable β -type Ti-25Nb-2Mo-4Sn alloy with high strength and low modulus. *Progress in Natural Science: Materials International*. 2013;23(2):174-182

[46] Attar H, Calin M, Zhang LC, Scudino S, Eckert J. Manufacture by selective laser melting and mechanical behavior of commercially pure titanium. *Materials Science and Engineering*. 2014; A593:170-177

[47] Shalnova SA, Klimova-Korsmik OG, Arkhipov AV, Yunusov FA. Structure and properties of near- α titanium products obtained by direct laser deposition and heat treatment. *Journal of Physics: Conference Series*. 2021; 2077(1):012018

[48] Gushchina MO, Kuzminova YO, Kudryavtsev EA, Babkin KD, Andreeva VD, Evlashin SA, et al. Effect of scanning strategy on mechanical properties of Ti-6Al-4V alloy manufactured by laser direct energy deposition. *Journal of Materials Engineering and Performance*. 2022; 31(4):2783-2791

[49] Ivanov S, Gushchina M, Artinov A, Khomutov M, Zemlyakov E. Effect of elevated temperatures on the mechanical properties of a direct laser deposited ti-6al-4v. *Materials*. 2021; 14(21):643

[50] Shalnova SA, Klimova-Korsmik OG, Turichin GA, Gushchina M. Effect of process parameters on quality of Ti-6Al-4V multi-layer single pass wall during direct laser deposition with beam oscillation. *Solid State Phenomena*. 2020;

299(SSP):716-722. DOI: 10.1007/s11665-021-06407-7

[51] ASTM. International B988-13, Standard Specification for Powder Metallurgy (PM) Titanium and Titanium Alloy Structural Components. West Conshohocken, PA: ASTM International; 2013

Section 2

Wettability of Powders

Chapter 3

An Application of Bio-Inspired Superwetting Surfaces: Water Collection

Chang Li, Zhongshi Ni and Ying Li

Abstract

On a superwetting surface, droplet behaviour can be manipulated. Utilising the directional motion and coalescence of water, water collection (including fog harvesting) is a significant application of superwetting surfaces. In the plant and animal kingdom, many biological surfaces show excellent water-collecting function. This chapter summarises the development and recent progress of the natural and bio-inspired surfaces that can collect water. The biomimetic models, i.e., the model of spider silks, cactus, and desert beetles are introduced. The corresponding mechanism, raw materials or approaches to mimic natural surfaces and optimised structures which show improved water-collecting performance are explained. Future directions for the water-collecting material are forecasted.

Keywords: super-wetting surface, bio-inspired, water transport, spider silk, cactus, desert beetle

1. Introduction

Water plays a crucial role in most creatures alive in nature, covering requests for organismic daily consumptions, agricultural irrigation, and industrial production. Water shortage is an acute problem in many areas of the world. Collecting water with satisfactory efficiency from a humid/foggy atmosphere is deemed as a fundamental step to release the tough issue, which is also a hot and significant research direction.

In water collection, fog-water capturing and water droplet transport for collection are two main steps. A single superhydrophilic or superhydrophobic surface could not meanwhile accelerate both courses. For example, hydrophilicity can speed up fog-water capturing. However, it may cause water retention, which may slow down water transport and further water harvesting. On a hydrophobic surface, droplets can roll easily for collection while the efficiency of fog-water capturing is very low. To handle the dilemma, researchers have paid attention to the natural superwetting surfaces which have an exciting ability to manipulate liquid behaviours [1, 2]. They possess special wettability designs or/and unique micro/nano-structures.

Creatures surviving in droughty environments usually have a special ability to collect water. For example, some desert plants and animals can capture water from the

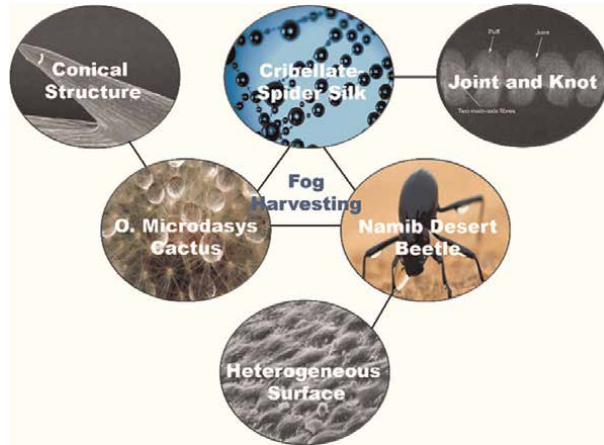


Figure 1. Biological surface that can collect water: spider silk with joint and knot, cactus with conical structure, desert beetle with heterogeneous surface.

humid air during nightfall caused of temperature differences. Creatures living in highly humid environments also have the ability to manipulate water droplets or flow. For example, on spider silk, morning dews are spontaneously collected. This chapter will respectively introduce the water collection ability of spider silks, cactus, and desert beetles (**Figure 1**). The natural surface and bio-inspired model to mimic the surface structure are involved. The strategies to enhance water collecting efficiency by designing special wettability or micro/nano-structure are detailly introduced.

2. Spider silks inspired spindle-knot fibre

2.1 Biological model and theoretical analysis of spindle-knot fibre

The ability to harvest fog is determined by the fog-water catching performance at the surface together with the removal efficiency of the captured water from the surface [3, 4]. One-dimensional (1D) fog collectors usually make use of some hydrophilic composition or/and water-loving structure to rapidly seize the water from a humid environment. Subsequently, small droplets hang on the 1D material and accumulated into larger droplets gradually. Finally, large droplets can fall into a container due to growing gravity.

Spider web has been well-known for its excellent mechanical, biochemical and pharmaceutical properties because of its network structure and the composition of biological proteins [5–8]. In the recent decade, a single spider silk was deeply studied and has been deemed as a perfect model for designing artificial water collector. The periodic spindle-knot structure on spider silk (similar to bead-on-string fibre) is useful. This structure can give rise to driving forces on dew based on Laplace pressure difference and probable surface energy gradient. These forces drive the droplet moving to the spindle knot, where the combined droplet is released and collected [9]. The Laplace pressure difference (**Figure 2(a)**) can be calculated by the following formula,

$$F_L \sim \gamma \left(\frac{1}{R_1'} - \frac{1}{R_2'} \right) \frac{\sin \beta}{R_1 - R_2} V \quad (1)$$

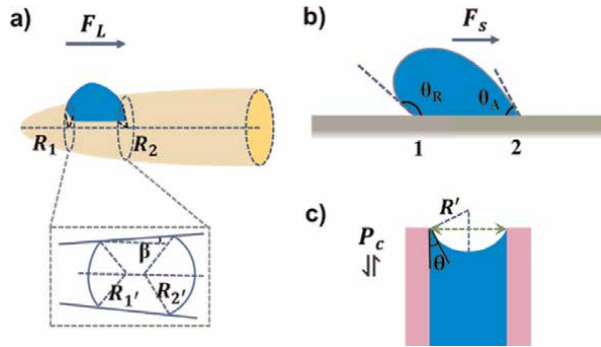


Figure 2.
 Sketch of force analysis on the bio-inspired water-collecting units.

where γ is the surface tension of water droplet, R_1' and R_2' indicates the local curvatures of the contact lines at two opposite sides of droplet along the spindle knot, R_1 and R_2 indicate the local radius of the spindle knot. Angle β is the half apex angle of the knot, which is related to the size and shape of the knot. V is volume of water droplet on knot, which can be approximate estimated by the formula $V = \pi R_0^3 / 12$, where R_0 indicates the radius of the droplet.

The spindle knot usually had a higher axial-parallel roughness than the other area on the fibre, contributing to a smaller contact angle. Therefore, the spindle knot is more hydrophilic and has a higher surface energy. The consequent driving force resulting from surface energy gradient (**Figure 2(b)**) can be described as follow,

$$F_S = \int_{L_j}^{L_k} \gamma (\cos \theta_A - \cos \theta_R) dl \quad (2)$$

where θ_A and θ_R , respectively indicate the advancing and receding angle of the water droplet on spider silk, and dl is the integrating variable from original silk joint (L_j) to the spindle knot (L_k).

Capillary pressure (result from small holes or probable grooves on spindle-knot) gradient can also be introduced into this system to speed up the water combination or transportation rate. The capillary force P_c (**Figure 2(c)**) is estimated by the Young–Laplace formula [10],

$$P_c = 2\gamma / R' \quad (3)$$

where R' indicates the curvature radius of surface of water in small holes or grooves.

2.2 Featured structures made by multi-methods using various materials

When aiming at mimicking the biological spindle-knot structure (**Figure 3(a)**) with consequent water-collecting function, diverse biomimetic methods are employed. For example, dip-coating, electro-dynamic, fluid-coating, and microfluidics have been developed or utilised [8, 16]. As shown in **Figure 3(b–j)**, diverse spindle-knot structures can be prepared.

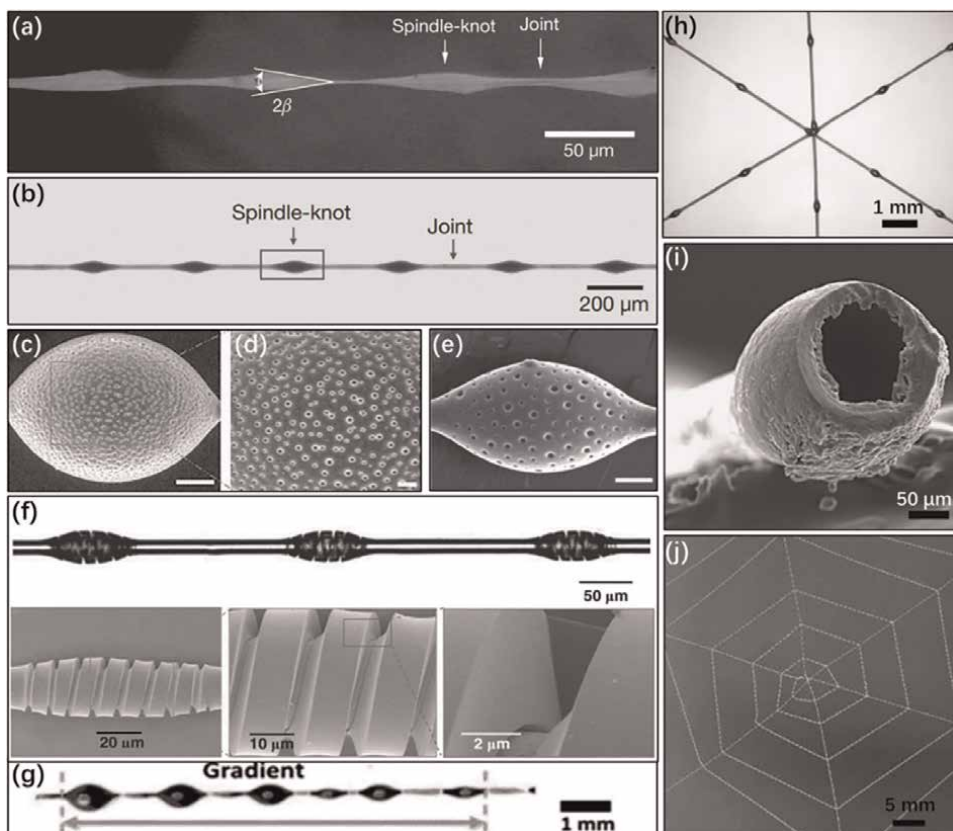


Figure 3. Spider silk and diverse artificial spider silks. (a) SEM image of spider silk in nature [9], scale bar 50 μm . (b) Optical image of artificial spider silk via traditional dip-coating [7], scale bar 200 μm . (c, d) SEM images of micro-porous bead on string fibre via dip-coating with breath figure method [11], scale bar 10 μm . (e) SEM images of gradient-porous bead on string fibre via dip-coating with breath figure method [11], scale bar 10 μm . (f) Optical image and SEM images of helical spindle-knot fibre via deep-coating and sequent calcination [12], scale bar 50 μm . (g) optical image of a gradient-sized spindle knot fibre via fluid-coating at an increasing drawn-out rate [13], scale bar 1 mm. (h) Photo of magnetic assembly integrated artificial spider silks [14], scale bar 1 mm. (i) SEM image of hollow artificial spider silk via microfluidics using nitrogen as inconsecutive phase [15], scale bar 50 μm . (j) Photo of integrated topological artificial spider silk to mimic spider web [15], scale bar 5 mm.

2.2.1 Dip-coating

Dip-coating is the earliest-developed, frequently-used, convenient and mature approach to mimic spider silk with fog harvest ability. In a typical process, a Nylon fibre (usually 50 ~ 300 μm in diameter) was immersed deeply into a polymer solution which had been prepared in advance. Afterwards, it was drawn out horizontally and a tubular membrane composed of the polymer solution wrapped the fibre uniformly. The membrane broke up into several ellipsoids on account of Rayleigh instability and then turned into a periodic spindle knot on fibre while getting dried (**Figure 3(b)**).

According to the Eqs. (1) and (2) mentioned above, the actuating force for droplet directional transportation depends on the shape and size of the spindle knots together with the interval of each two periodic knots. These factors can be optimised by changing the processing parameters such as the viscosity or volatility of polymer solution, drawn-out velocity, and desiccation condition [17].

In order to improve fog-water capturing efficiency, the spindle knot can be further designed and manufactured into a porous spindle knot due to the high specific surface area and enhanced absorbability. For example, breath-figure method [11, 18] was utilised to achieve steerable micro-pores (**Figure 3(c and d)**), and gradient pores (**Figure 3(e)**).

Some spindle knot with ring or helical grooves (**Figure 3(f)**) which show better performance has been developed [12]. To fabricate such periodic ring or helical grooves spindle knot on 1D material, an added procedure of calcination or desiccation under a high temperature (more than 800 K) was essential. Conventional polymer fibres such as Nylon could not stay non-deformation or unshrink at such high temperature. Hence, Glass Fibre or Carbon Fibre (usually 7–15 μm in diameter), with greater high-temperature resistance properties and other mechanical performance, were employed as host fibre material in these studies [11, 12]. Furthermore, rather than the organic polymer solution, some inorganic compounds and materials with ameliorate biocompatibility, such as Titanium salt/oxide [12, 19], would be used if environment conservation or other intention was taken into consideration.

2.2.2 Fluid-coating

Dip-coating is capable of fabricating fine accurate structure (usually 7 ~ 300 μm diameter fibre with minimum feature size about 5 μm) on the fibre. However, it is difficult for dip-coating to realise large scale preparation. Fluid-coating was developed and continuously massive coating comes true [20]. Artificial spider silks in random length are likely to be synthesised via this approach, which is a promising method for the industry.

The principle and operating steps of fluid-coating to prepare spindle knot are similar to dip-coating. As is reported in previous work [21], a Nylon fibre (about 70 μm in diameter) was steadily fastened in a polymer solution reservoir (width: 2 cm, length: 3.5 cm, height: 3 cm, with one edge attached to a motor) through two capillary tubes (400 μm inner diameters). The motor drew the fibre out at the desired speed and the polymer solution (parallel to the solution in dip-coating method, **Table 1**) moved with the fibre thanks to the viscous force. Then the fluid covered the fibre to become a cannular polymer membrane and it broke up into droplets on account of Rayleigh instability, which ultimately turned into periodic spindle knots on fibres after evaporation.

The unique feature of fluid-coating lies in the alterable and steerable drawn-out rate. It is reported that by drawing out at a monotone increasing velocity, gradient in thickness of polymer film emerged and gradient-size spindle knots (**Figure 3(g)**) were generated on fibre eventually [13]. Researchers also tried fishing-line fibres, copper fibres and carbon fibres to be the host fibres (**Table 1**) and obtained a satisfactory mechanical property.

2.2.3 Electrodynamic

Electrodynamic technology is another strategy for large-scale preparation of artificial spider silks. This method is good at preparing slender (200 nm ~ 12 μm in diameter) silk with fat spindle or even ellipsoid knot (usually 3 ~ 6 times of the slender silk in diameter, the whole artificial silk namely bead-on-string fibre).

Pervious works [22–24] justified the practicability of a coaxial electrospinning method (namely core-shell electrospinning), which developed from conventional

Ref.	Method	Host fibre	Polymer solution	Structural feature
[9, 17]	DC	Nylon	DMF, PMMA	First-made and similar to real spider silk
[11]	DC	Carbon fibre	DETA, ER	Different porous structure on knot
[12]	DC	Glass fibre	TiBO-P123 sol gel	Helical crack on spindle knot
[21]	FC	Nylon	DMF, PVDF	Surface with different roughness
[21]	FC	Fish-line fibre	DMF, PMMA	Gradient-sized spindle knot
[21]	FC	Copper fibre	DMF, PMMA	Gradient-sized spindle knot

DMF: *N, N*-dimethyl formamide, PMMA: polymethyl methacrylate, PVDF: polyvinylidene fluoride, DMAc: *N, N*-dimethyl acetamide, DETA: Diethylenetriamine, ER: Epoxy resin-44, TiBO: titania butoxide, P123: HO(CH₂CH₂O)₂₀(CH₂CH(CH₃)O)₇₀(CH₂CH₂O)₂₀H.

Table 1. Materials and polymer solutions are used in dip-coating (DC) and fluid-coating (FC) to make artificial spider silk.

Ref.	Outer fluid (shell)		Inner fluid (core)	
	Solution (wt)	Solvent (w/w)	Solution (wt)	Solvent (vol/vol)
[27]	20% PEG	1:1 MC and DMF	35% Polystyrene	DMF
[28]	25% PMMA	7:3 THF and DMF	30% Polystyrene	DMF
[29]	10% PNIPAM	1:1 THF and DMF	16% PVDF	3:2 DMF and Acetone
[30]	PVDF-HSP-FPOSS ^a	1:1 THF and DMAc	PVDF-HSP-FPOSS ^b	1:1 THF and DMAc

^asol-gel: 2 g PVDF-HEP and 1 g FPOSS in 16 mL solvent.

^bsol-gel: 2 g PVDF-HEP and 1 g FPOSS in 32 mL solvent.

PEG: polyethylene glycol, MC: methylene chloride, DMF: *N, N*-dimethyl formamide, PMMA: polymethyl methacrylate, THF: tetrahydrofuran, PNIPAM: poly(*N*-isopropylacrylamide), PVDF: polyvinylidene fluoride, PVDF-HSP-FPOSS: poly(vinylidene fluoride-co-hexafluoropropylene) with fluorinate polyhedral oligomeric silsesquioxane, DMAc: *N, N*-dimethyl acetamide.

Table 2. Chemical reagents are used for outer and fluid polymer solutions in different electrodynamic studies to make artificial spider silk.

coaxial electrospinning and electrospinning. In this method, heterogeneous liquids with different viscosity and vapour pressure-filled two different channels of jet. Dilute solution in the outer channel was electro-sprayed into micro-particles (finally acting as spindle knots) due to Rayleigh instability (or combined with wet-assembly technique) [19, 25]. The inner viscous liquid channel was electrospun to micro- or nano-fibres [26].

As is displayed in **Table 2**, multifarious chemical substances were used to prepare inner and outer solutions to meet the request for wettability, finance, or environment-protecting [27–30]. To exemplify it, poly-L-lactic acid (PLLA) was chosen as a raw material on the basis of being degradable, whose solution (6 wt% PLLA dissolved in Chloroform and DCM: dichloromethane with different volume rates ranging from 95/5 to 65/35 and stirring at room temperature) electrospun bead-on-string fibre exhibited a higher directional transport performance compared with PVA solution (10 wt% polyvinyl alcohol dissolved in hydrothermal water containing 17 wt% glutaraldehyde) [31].

Albeit electrodynamic approaches can enable relatively large-scale production of bead-on-string hierarchical nanofibres with satisfactory fog-harvesting (normally ~5 g water, fog flow ~25 mL per hour), mechanical properties such as tensile strength should be improved to prolong the lifespan of fibres. To achieve this, adding postprocessing (e.g., carbonation procedures to transfer it into carbon fibre) can be a decent measure.

2.2.4 Microfluidics

Microfluidics was a relatively recent developed technology to continuously fabricate artificial spider silk. By adjusting the relative location of syringe needles in convention microfluidic devices, artificial spider silk could be synthesised via imitating the authentic spinning process of nature spiders [32].

In a coaxial microfluidic device, there are two flows of liquids (**Table 3**) with different feeding rates. In a typical synthesis [33], a micropipette was employed where an Alginate-based composite solution (ABC solution) served as the continuous phase and liquid Paraffin served as the dispersed phase, respectively consisting of the host fibre and spindle-knot of artificial spider silk after dehydration. The diameter of host fibre and geometry size of periodic spindle knot as well as the distance between two adjacent spindle knots can be altered by optimising the parameter of feeding speed of two flows (and their feeding speed ratio).

To achieve the porous surface of joint or spindle-knot of artificial spider silk to get enhanced fog-captured performance, add a component with distinct solubility (salt such as NaCl or CaCl₂) into the liquids and then remove it by washing or soaking in aqueous solution [26]. Analogously, Fe₃O₄ nanoparticles can be added to the volatile oil drops during microfluidic operation to obtain magnetic property of spindle knot. The synthetic 1D materials can then be assembled or patterned (**Figure 3(h)**) into the multidimensional structure under an external magnetic field [14]. Additionally, gas (e.g., nitrogen [15]) can be used as a dispersed phase and bioinspired cavity-microfibres (**Figure 3(i and j)**) can be fabricated.

2.3 Water collecting efficiency of artificial spider silks

By optimising the geometry of periodic spindle knots, artificial fibres could show enhanced performance in fog-harvesting tests (**Figure 4**). As is demonstrated in **Figure 4(a)**, five small water drops moved and combined rapidly within 4.39 s on a PMMA spindle-knot Nylon fibre. It is recorded that when the vertical downward fog

Ref.	Continuous phase	Dispersed phase	Feature
[33]	Sodium Alginate	Liquid Paraffin	Improved microfluidics preparation
[14]	Calcium Alginate	Oil drop+ Fe ₃ O ₄ nanoparticles	Magnetic 2D or 3D assembly fibre
[15]	ABC solution ^a	Nitrogen	Hollow fibre (with topological weave) ^b

^aAlginate based composite (other salts) solution.

^bTopological structure by postprocessing.

Table 3.

Substance employed in microfluidics to produce artificial spider silks and their corresponding feature.

flow was ~ 0.75 m/s, the artificial fibre which is 1.5 mm in length could collect 40 nL of water within 12 s in comparison with 17 nL of natural spider silk under a similar circumstance [21].

Distinct types of spindle knot may give rise to different impact on fog-harvesting function. The in-situ observation and optical images of water collecting test on artificial fibre with gradient-size spindle knots (**Figure 4(b)**) showed that droplet coalescence with a special mode could be implemented. Under $\sim 90\%$ humidity using ultrasonic humidifier, 7.35 mm fibre with gradient-size spindle knots was capable of harvesting water at a rate of 509.4 $\mu\text{L}/\text{h}$, while 156.7 $\mu\text{L}/\text{h}$ of water was collected using similar fibre with uniform sized periodic spindle knots under the same condition [13]. Porous surface morphology also brings in increasing efficiency of water collecting. As illustrated in **Figure 4(c)**, under same $\sim 100\%$ high humidity condition using humidifier, water collecting efficiency had the following rank: gradient porous structured $>$ homogenous porous structured $>$ smooth spindle-knot fibre [11]. Additionally, spindle knots do play a significant role in improving the water-harvesting efficiency (**Figure 4(d)**).

Intersection would gain an easier access to capture and harvest fog-water (**Figure 4(e)**). In an updated research, two intersectional silks (8.25 μL in 60 s) tended to harvest more water than two parallel silks (4.57 μL in 60 s) in 60s under a 0.408 mL/min fog flow. Topological network bioinspired by spider web exhibited

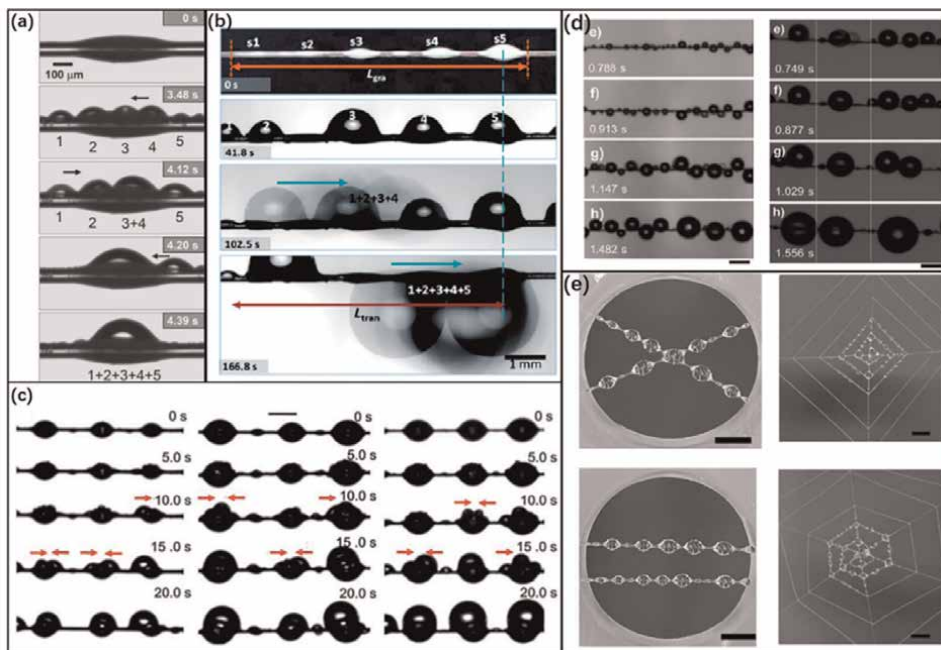


Figure 4. Fog-collecting characterisation images of diverse artificial spider silks. (a) In-situ observation of directional fog harvesting of conventional PMMA spindle-knot (by fluid-coating) on Nylon fibre [21], scale bar 100 μm . (b) Optical images of water collecting on gradient sized PMMA spindle-knot (by fluid-coating) on Nylon fibre [13], scale bar 1 mm. (c) Optical images of aggregation of water droplet of ER knots (all by deep-coating) with smooth, homogenous porous and gradient porous structure on carbon fibres [11], scale bar 50 μm . (d) Optical images of PMMA-PS bead on string (right) fibre and smooth PS (left) fibre (all by electrodynamic) [28], scale bar 20 μm . (e) Photos of fog harvesting on Alginate based cavity (all by microfluids) fibres [15], scale bar 5 mm.

much higher fog-harvesting efficiency: 150 mm topological networks with two radius were able to collect 53.297 μL in 120 s and with three radius, the volume is 68.957 μL in 120 s [15].

By comparing the water collecting performance of diverse artificial spider silks (Figures 4 and 5), it can be summarised that appropriate shape (slenderness ratio: 1 ~ 10), size (gradient sized spider-knot) and morphology (knot with porous microstructure especially gradient porous microstructure) of artificial spider silks, resulted from optimised processing parameters (Figure 5(a)), will contribute to better fog-harvesting performance. Diverse materials with different structural or wettability design differs in water-harvesting style and efficiency (Figure 5(b and c)). Temperature, humidity or flow rate in the water-collecting test may also affect water-collecting volume (Figure 5(c and d)).

In addition, 2D or 3D intersectional arrangement of artificial fibre to mimic the real topological spider web in nature turns out to own an larger-scale fog-harvesting capacity than 1D spider silk [4]. For example, combined with advanced multi-directional braiding technology, multidimensional integrated spider silks can be acquired with relatively large scale fog harvesting capacity [34, 35]. These 2D or 3D

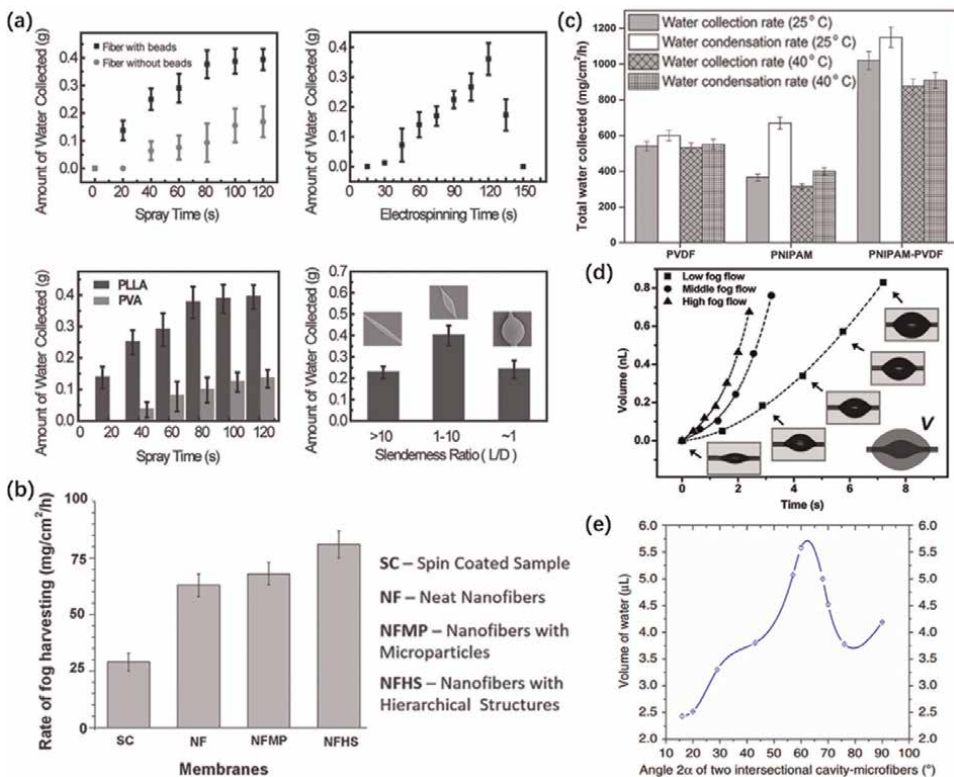


Figure 5. Various factors which may exert influences on fog-harvesting performance of artificial spider silks. (a) Impacts of spray times, electrospinning times in electrodynamic method slenderness ratio, materials and fibre with/without beads on fog-harvesting [31]. (b) Influences of postprocessing and hierarchical structure of fibre on fog-harvesting [30]. (c) Effects of temperature, materials and core-shell structure on water condensation and water harvesting [29]. (d) Impacts of fog flow rate in water-harvesting [17]. (e) Influence of intersectional angle of two artificial spider silk on fog-harvesting [15].

network materials were estimated to harvest up to 0.5 ~ 1.5 ton/day (per square meter of material) fog-water in foggy environment (e.g., industrial cold-water tower). To prepare artificial fibre in industrial scale and to harvest water in much larger scale should be future research topics [36].

3. Cactus inspired conical structure

3.1 Biological model and theoretical analysis of cone

Plants survived in extraordinarily droughty conditions tend to have advanced fog-harvesting ability inevitably. Inspired by a cactus [37], conical structures were developed as a perfect model for water collecting. Agaves [38] and wheat awns [39], which have similar needle-like construction, also can harvest fog. The geometry of cone can be deemed as half of a spindle knot to some degree when analysing driving force. The Laplace force is an attraction to gather fog-water, which can be calculated by Eq. (1). Also, roughness gradient (Eq. (2)) can be introduced.

By integrated the cones into oblique conical micro- and/or nano- array (or barbed array, bioinspired by *Eremopyrum orientale* or ryegrass leaves) [40, 41] on 2D planar materials, anisotropy surface with enhanced water-collecting property from foggy atmosphere were developed. As for the mechanism, oblique array with anisotropy gives rise to a difference in concomitant retention force (F_r) on hindering water transport to two directions. When the droplet moves, the retention force can be estimated by [42]

$$F_r = w\gamma(\cos \theta_{RO} - \cos \theta_{AO}) \quad (4)$$

where w is the width of water droplet, θ_{RO} and θ_{AO} indicate the intrinsic contact angle. Moving along the oblique direction, decreasing solid-liquid contact width is beneficial to postpone the water meniscus resulting in water release, while moving against, increasing solid-liquid contact width causing pinning of water droplet. Experiment also illustrates that the retention forces of the droplet against the oblique direction are larger than those along the oblique direction [40, 43]. As a result, the distinction of retention force along two opposite direction can ultimately lead to water directional removal.

3.2 1D and 2D patterns via different methods using distinct materials

With regards to 1D pattern, research was frequently carried on metals with hydrophilicity. Thanks to the electroconductivity of metals, electrochemical method (e.g., controlled electrochemical corrosion or gradient anodic oxidation) can be employed [44, 45]. For instance, a copper wire (usually ~800 μm in diameter) was placed vertically and attached to the anode of a 10 V DC power with a curled copper sheet connected with the cathode. For one thing, a container filled with CuSO_4 solution (electrolyte) pumps from a syringe pump which increases the liquid level of electrolyte at a constant velocity, causing a gradient of electrochemical corrosion of the copper wire and thus producing a conical shape. For another, controlled by a periodic current (from 0.05 to 0.8 A, pondered for 5 s, and then declined to 0.05 A) using the DC power, the roughness gradient was obtained.

In terms of 2D planar model, an interesting method called soft lithography [40, 41, 44, 45] was developed to directly copy biological surfaces. Primarily, fresh biological sample was fixed flat on a petri dish. Non-fizzy PDMS mixture (10:1 polydimethylsiloxane and its curing agent after uniform stir and vacuum treatment) was decanted into the dish and heated at 325 ~ 353 K for 3 ~ 5 hours (heating temperature and time contributing to hardness and flexibility of as-prepared PDMS model). After free cooling to room temperature, PDMS model was apart from biological sample with caution. Whereupon, the mirror symmetric PDMS mould of target architecture had been prepared. Eventually, an analogous step was repeated to get the target structured model. If the material of target model must be PDMS, original PDMS mirror was fluoridized (fluorination in vacuum at 363 K for 5 h) beforehand. As for PVDF material, PDMS mirror was pressed on the PVDF powders (which has spread on a clean glass slide and heated to 543 K until the organic material were fully melting in advance) at 2×10^6 Pa for 10 seconds. Microstructure of biological sample can be easily copied by such patent. In addition, for conical array surface pattern without using biological sample, the mirror mould mentioned above can also be manufacture via machine spotting, drilling or punching on PE (polyethylene) or PVC (polyvinyl chloride) board [46]. By adding magnetic powders (such as Co) into PDMS before curing, flexible magnetic PDMS pattern was made whose cone array could tilt at desirable angles under controllable external magnetic field [43, 46, 47].

3.3 Fog-harvesting efficiency of cactus inspired structure

Multi-gradient copper wire shows a satisfying efficiency in fog-harvesting tests. As illustrated in **Figure 6(a)**, the first three water drops transported and combined into one droplet within 0.18 s directly the first water drop was formed on the cone copper wire [44]. In another research [45], oxidised copper wire with multi-gradient was compared with the original copper wire, showing a unidirectional movement and enhanced (increasing ~70%, in 60 s) fog harvesting efficiency (**Figure 6(b)**). Fog harvesting performance of such 1D cone sample is associated with the tilt angles of placing sample. As demonstrated in **Figure 6(c)**, the collecting efficiency peaked at 0.36 mg/s (experiment done in temperature 288 K, and fog flow velocity 1.8 m/s) when gradient cone copper wire was placed horizontally [44].

2D biomimetic models also show high efficiency or show larger-scale water-collecting capacity. As demonstrated in **Figure 6(d)**, PDMS surface with vertical needle-like array showed a fog harvesting function at 80% humidity air while magnetic cone with flexibility under alternating magnetic field exhibited 50 times higher fog-harvesting efficiency (at about 0.2 g/h under the quasistatic foggy environment) in 1 hour than the static cone [46]. Biomimetic copied artificial leaf with oblique barbed array on surface involves a fog-harvesting capacity of 95.4 g/m²/h (air flow rate of 10 L/min and 3.5 bar pressure delivering a water nebulization rate of 0.4 mL/min at 296 K) and it was improved to 136.8 g/m²/h after an initiated chemical vapour deposition of hydrophobic surface nanocoating. It is worth noting that by integrated 18 copper wire 1D patterns (fixed on a 6.5 × 6.5 × 0.5 cm Teflon frame, side-to-side horizontally setup) into a tiny water-collecting device, the highest value of fog-harvesting rate can reach up to surprisingly 6180 g/m²/h under 2.4 m/s fog velocity in temperature 288 K [44].

From what is cited above, it is safe to draw a summary that different gradient in surface morphology or shape of cone structure, arrangement of cone or cone array, and wettability of materials will affect fog-harvesting performance.

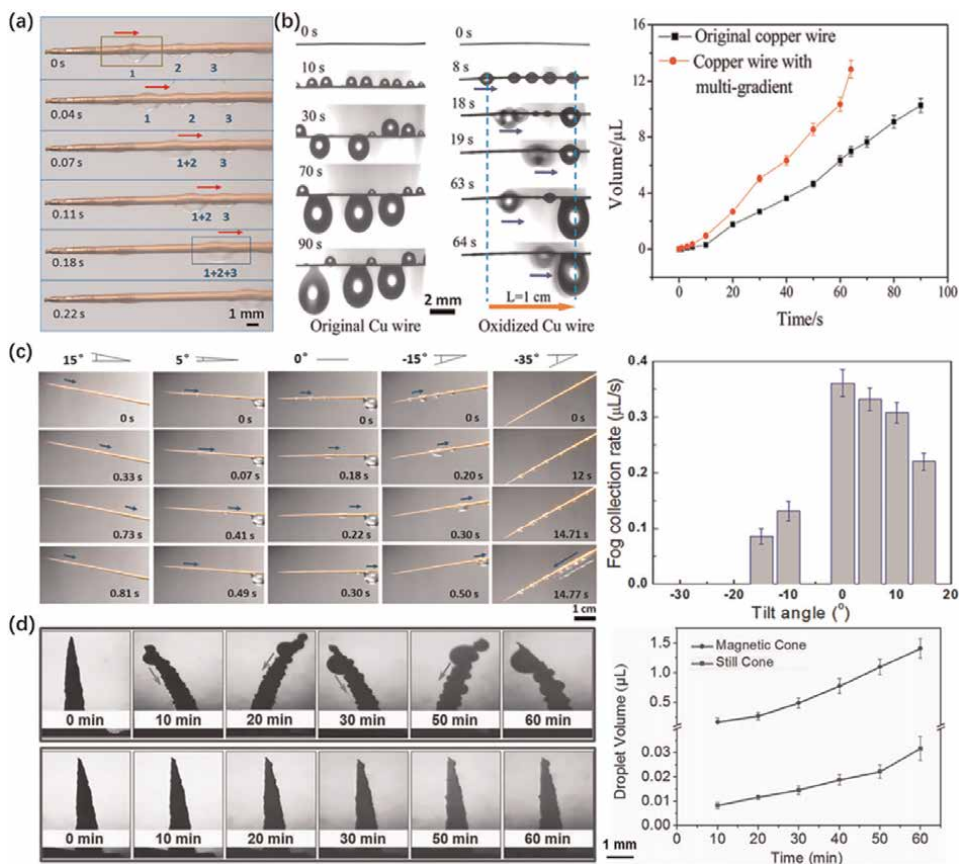


Figure 6. Water-collecting of diverse cone structured patterns. (a) Transport process of first three drops on a multi-gradient cone copper wire (by controlled electrochemical corrosion) [47], scale bar 1 mm. (b) Fog-water collection behaviour between an original copper wire and a multi-gradient copper wire (by gradient anodic oxidation) [45], scale bar 2 mm. (c) Fog-water unidirectional transport properties of a multi-gradient cone copper wire (by controlled electrochemical corrosion) at different tilt angles [44]. (d) Water harvesting of a magnetic cone with and without the external magnetic field in the same chamber [41].

4. Desert beetle inspired heterogeneous surface

4.1 Biological model and theoretical analysis of wettability paradox

Namib desert is one of the oldest and driest existing desert in the world. Plenty of species died out while others which have been adapted to the arid conditions (such as Namib desert beetle, spider, snack, grass, cactus) enjoy a good life. Desert beetle, with superhydrophilic wax-free texture (peaks) and hydrophobic wax-coated array (groove) on its back, has long been imitated for fog collecting [48, 49].

Heterogeneous wettability architecture has also been found in the plant kingdom, i.e., the *Salvinia*. *Salvinia* effect [50, 51] represents the stabilisation of an air layer upon a submerged superhydrophobic surface with hydrophilic pins array (which might be a new model for fog-harvesting in the future studies). *Salvinia* wettability paradox further indicates the phenomenon of a functional entirety with discrete wettability, similar to the heterogeneous construction of Namib desert beetle back.

The principle of its fog-harvesting ability is the fact that superhydrophilicity makes it easier to seize water and superhydrophilic texture combined with hydrophobicity groove gives an appointed route for water drop to transport. The discrete driving force of wettability imbalance can be calculated by Eq. (2), further describing as

$$F_w = \gamma(\cos \theta_{\text{hydrophilic}} - \cos \theta_{\text{hydrophobic}}) \quad (5)$$

where $\theta_{\text{hydrophilic}}$ and $\theta_{\text{hydrophobic}}$ are contact angle of water on two opposite sides with two distinct wettability. If the $\theta_{(\text{super})\text{hydrophobic}} > 150^\circ$ and $\theta_{(\text{super})\text{hydrophilic}} < 5^\circ$, a large driving force caused by wettability imbalance will impel water droplet into more hydrophilic region, which can be further designed as fog-harvesting model.

4.2 Various wettability paradox obtained by diverse advanced technology

In order to obtain an entirety with discrete wettability, scientists with distinct research backgrounds may utilise diverse advanced approaches. A facile avenue is to composite (in a macroscopic scale) another material with distinct wettability onto the surface of original material. For example, a superhydrophobic copper oxide gauze can be incorporating onto the surface of a hydrophilic PS flat sheet through thermal pressing [52].

Another strategy is to fabricate by various coating or corrosion technology on a basic material (e.g., glass slide) to selectively change the wettability (e.g., via a mask). For instance, primarily, a superhydrophilic surface composed of TiO₂ nanoparticles was obtained on a bare glass substrate via a spin-coating method. Then, it was superhydrophobically treated using heptadecafluorodecyl-trimethoxysilane (FAS). Last but not least, the functional pattern was realised by illuminating the FAS-modified film under UV light with a photomask. The FAS-treated superhydrophobic TiO₂ surface becomes superhydrophilic again owing to the photocatalytic decomposition of the FAS monolayer after being exposed to UV light [53]. Via this approach, circle-pattern, 4-, 5-, 6-, 8-pointed star-patterns, and other graphic patterns was manufactured on surface (**Figure 7(a)**). The graphic patterns depend on the geometry of photomask.

Laser treatment can be used in manufacturing wettability gradient. For example, a superhydrophilic-superhydrophobic surface on Pyrex wafer was prepared using femtosecond lasers, through the processes of Teflon-like polymer (CF₂)_n depositing and Femtosecond laser ablation to selectively remove the superhydrophobic coating [55]. Similarly, selective plasma corrosion [56], electrochemical etching [57], and inkjet printing [54], with similar designed procedures, have been developed to obtain micropatterns with wettability paradox.

4.3 Fog-harvesting efficiency of bioinspired heterogeneous surface

The strategy of fog-harvesting inspired by desert beetle turns out to be very effective. As is displayed in **Figure 8(a)**, a high-contrast (superhydrophobic array) wetting glass collected more (60%) fog within 30 min than a blank glass [55]. In another research, by changing the size and arrangement density of superhydrophobic array, ~ 400% improvement in fog-harvesting test (**Figures 7(b) and 8(b)**) was realised (increasing from 149 g/m²/h to 618 g/m²/h, at about 295 K environmental temperature and ~ 0.1 m/s fog rate using humidifier, the surface temperature of sample: 277 K and air around sample: 90–95% humidity, vertically placed) [54].

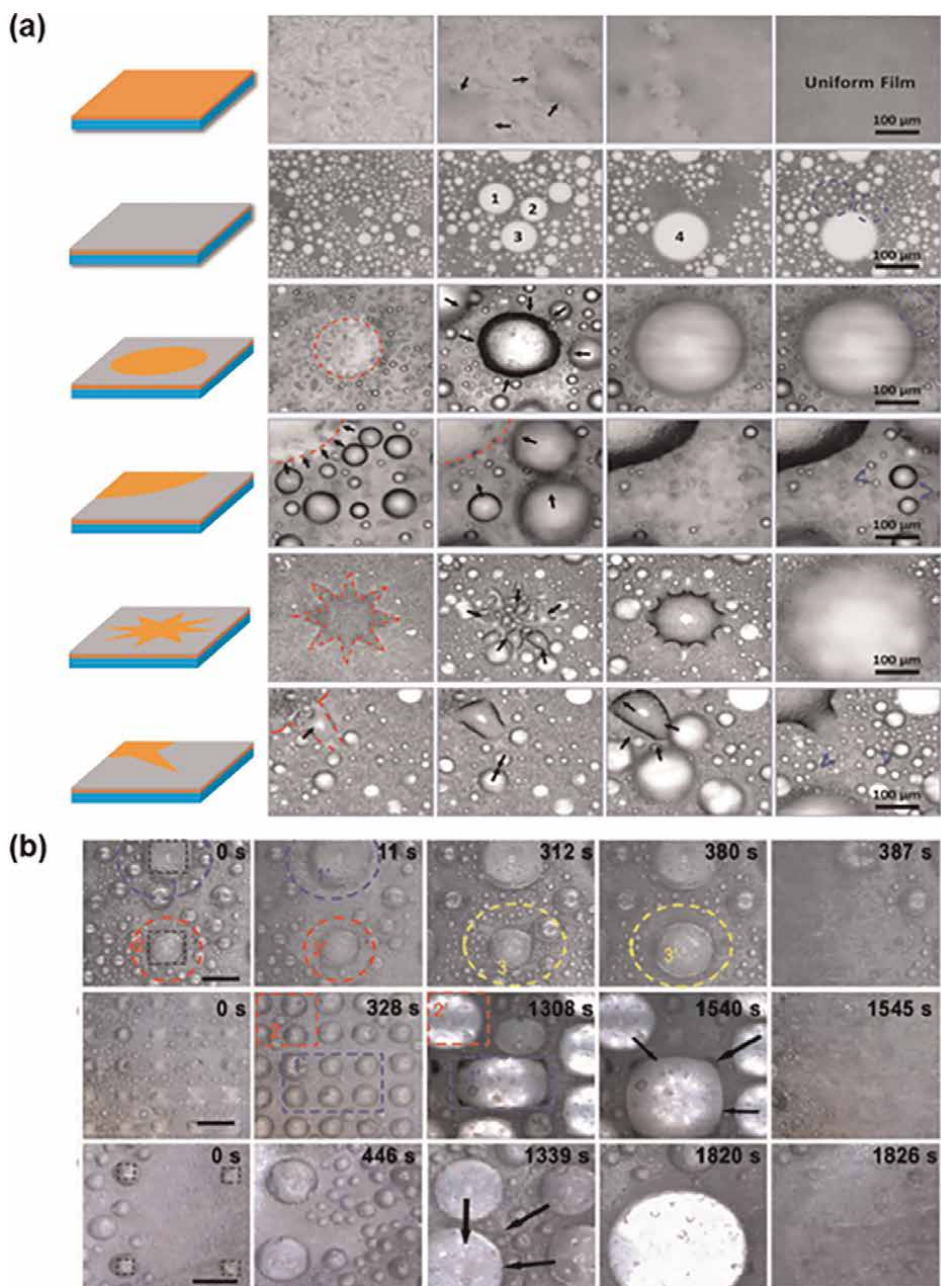


Figure 7. Water collection processes on various kinds of surfaces inspired by desert beetle. (a) Observation of water collecting behaviour on wettability-paradox surface with distinct graphic pattern (fabricated via FAS-modifying and UV selective photocatalytic decomposition): from top to bottom: superhydrophilic surface, superhydrophobic surface, circle-shaped pattern surface, circle-shaped edge surface, star-shaped edge surface, star-shaped circle surface [53], scale bar 100 μm. (b) Observation of water collecting behaviour on wettability-paradox surface with distinct arrangement density and size (fabricated via dopamine ink-jet printing), from top to bottom: superhydrophobic surface with 500/200/200 mm polydopamine patterns and respectively corresponding 1000/400/1000 mm separation [54], scale bar 500 μm.

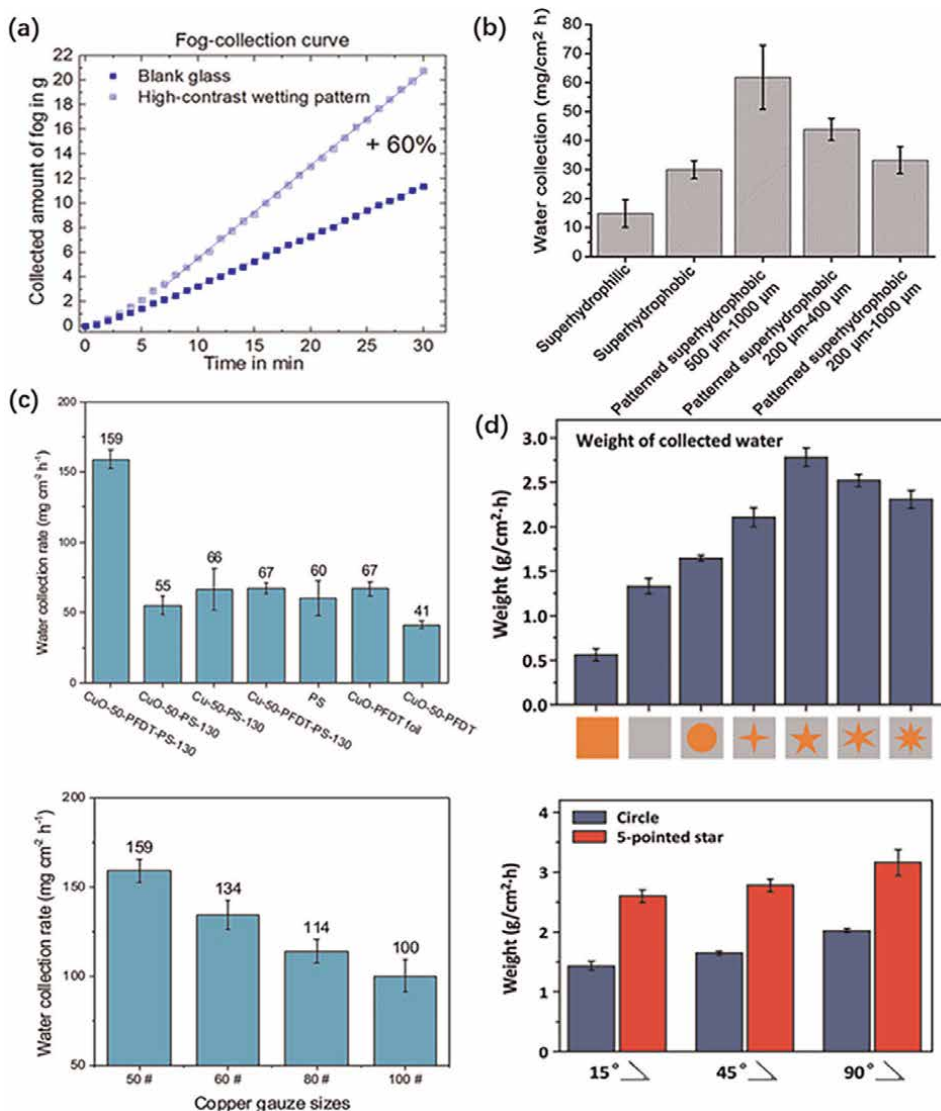


Figure 8. Distinct factors which may exert influences on fog-collecting efficiency of wettability-paradox surfaces inspired by desert beetle. (a) fog harvesting comparison of a piece of blank glass and a piece of glass with wettability-paradox surface [55]. (b) Influence of arrangement density and size on water collecting efficiency [54]. (c) Impacts of materials and density of composite on water collecting efficiency [52]. (d) Effects of pattern shapes and placed incline-angle upon fog-harvesting efficiency [53].

As composite can be made of different materials and density, how these factors affect water-collecting property had been investigated. As demonstrated in **Figure 8(c)**, component and gauze size exert considerable influences on fog harvesting (due to the distinct contact degrees of the hydrophobic gauzes), where the maximum fog collecting rate was 1590 g/m²/h at ambient conditions (a simulated flow of fog about 0.12 m/s, relative humidity around the samples: 90–95% and temperature: 295 K, vertically placed) [52].

Fog harvesting performance is also linked to the graphic pattern on wettability paradox surface. Different fog-collecting processes was found on surfaces with various wettability features (**Figure 7a**). On uniformly superhydrophilic surface, the water droplet spread over surface while on total superhydrophobic surface, individual water droplets coalesced in disorder. However, water droplets gathered directionally toward the superhydrophilic place on bioinspired surfaces with wettability pattern. Diverse wettability pattern offers different route for water to combine and move away, resulting in distinct fog harvesting performance. Generally speaking, the fog collecting processes are relative continuous because immediately after a fog-water droplet move away, another one can be captured. Consequently, directional motion of tiny water droplets enhances the fog-collecting efficiency. In terms of fog-harvesting efficiency, the highest value occurred in 5-pointed star wettability pattern, which peaked at amazing 27,800 g/m²/h (fog flow 0.75 m/s in velocity under room temperature, inclined by 45° from the horizontal plane). In addition, the placed incline-angle also affects the collecting rate and simply by placing it vertically, the efficiency climbed to ~32,000 g/m²/h (**Figure 8(d)**) [53].

5. Conclusion

In conclusion, fog-collecting function can be obtained by employing various biomimetic patterns inspired by diverse natural organisms. The water collection performance is firmly associated with the ability to seize fog-water from wet environment and the ability of directional droplet transport after the fog-water being captured. What on earth is more important may depend on the different foggy environment (e.g., the humidity or fog-flow rate of the environment). This question should be perfectly solved via simulated calculation and experimental verification in future research. Additionally, it is difficult to compare the absolute value of water-collecting efficiency since the fog-harvesting tests was carried out in different foggy environment (e.g., difficult humidity, fog-flow rate, temperature, and/or pressure) by researchers. However, the above sections have explained and concluded how to change the processing parameter to improve the water-collecting performance.

In terms of the raw materials of the fog harvester, both organic (including but not limited to various polymers and biomaterials) and inorganic (containing metals, glass, silicon slice, etc.) materials were employed. As for the wettability, appropriate hydrophilicity is beneficial to fog-water capturing while water transport can be accelerated using micro/nano-structured or/and hydrophobic surfaces.

Not only was the fog-harvesting efficiency significant, but also the mechanical property, durability, economy, degradability, and biocompatibility should be considered. It also merits noting that magnetic, light, electric, thermal, and pH responds of specific materials are possible to be designed as driving force for accelerating the speed of water direction removal, which would be a promising research direction in the future [2, 58].

The studies concerning bio-inspired fog-harvesting performance involves a multi-subject course. On the one hand, brand-new chemical, physical, and mechanical routes to manufacture pattern with fog-harvesting capacity has been developed. On the other hand, these findings are most likely to be put into practice in various domains such as fluidics, hydraulics, environment-protecting, pharmaceuticals, mechanics and textile.

Acknowledgements

Chang Li is supported by China Scholarship Council (No. 202008060076).

Conflict of interest

The authors declare no conflict of interest.

Author details

Chang Li^{1*}, Zhongshi Ni² and Ying Li³


1 Department of Mechanical Engineering, Imperial College London, London, UK

2 College of Engineering, University of Massachusetts Amherst, Amherst, MA, USA

3 School of Education, University of Glasgow, Glasgow, UK

*Address all correspondence to: c.li19@imperial.ac.uk; hamster@188.com

IntechOpen

© 2022 The Author(s). Licensee IntechOpen. This chapter is distributed under the terms of the Creative Commons Attribution License (<http://creativecommons.org/licenses/by/3.0>), which permits unrestricted use, distribution, and reproduction in any medium, provided the original work is properly cited. 

References

- [1] Li M, Li C, Blackman BRK, Saiz E. Energy conversion based on bio-inspired superwetting interfaces. *Matter*. 2021; 4(11):3400-3414
- [2] Li M, Li C, Blackman BRK, Eduardo S. Mimicking nature to control bio-material surface wetting and adhesion. *International Materials Reviews*. 2022;67(6):658-681. DOI: 10.1080/09506608.2021.1995112
- [3] Seo D, Lee J, Lee C, Nam Y. The effects of surface wettability on the fog and dew fog-water harvesting performance on tubular surfaces. *Scientific Reports*. 2016;6:24276
- [4] Li C, Liu Y, Gao C, Li X, Xing Y, Zheng Y. Fog harvesting of a bioinspired nanocone-decorated 3D fiber network. *ACS Applied Materials & Interfaces*. 2019;11(4):4507-4513
- [5] Tsuchiya K, Ishii T, Masunaga H, Numata K. Spider dragline silk composite films doped with linear and telechelic polyalanine: Effect of polyalanine on the structure and mechanical properties. *Scientific Reports*. 2018;8:3654
- [6] Xiang P, Wang S, He M, Han Y, Zhou Z, Chen D, et al. The in vitro and in vivo biocompatibility evaluation of electrospun recombinant spider silk protein/PCL/gelatin for small caliber vascular tissue engineering scaffolds. *Colloids and Surfaces B-Biointerfaces*. 2018;163:19-28
- [7] Michalik M, Surmacka M, Stalmach M, Wilczek G, Kowalska T, Sajewicz M. Application of thin-layer chromatography to ecotoxicological study with the steatoda grossa spider web. *JPC-Journal of Planar Chromatography-Modern TLC*. 2018; 31(1):7-12
- [8] Chen Y, Zheng Y. Bioinspired micro-/nanostructure fibers with a water collecting property. *Nanoscale*. 2014;6(14):7703-7714
- [9] Zheng Y, Bai H, Huang Z, Tian X, Nie F, Zhao Y, et al. Directional water collection on wetted spider silk. *Nature*. 2010;463(7281):640-643
- [10] Liu H, Cao G. Effectiveness of the Young-Laplace equation at nanoscale. *Scientific Reports*. 2016;6:23936
- [11] Feng S, Hou Y, Chen Y, Xue Y, Zheng Y, Jiang L. Water-assisted fabrication of porous bead-on-string fibers. *Journal of Materials Chemistry A*. 2013;1(29):8363-8366
- [12] Wang L, Ji X, Wang N, Wu J, Dong H, Du J, et al. Biaxial stress controlled three-dimensional helical cracks. *NPG Asia Materials*. 2012;4:e14
- [13] Xue Y, Chen Y, Wang T, Jiang L, Zheng Y. Directional size-triggered microdroplet target transport on gradient-step fibers. *Journal of Materials Chemistry A*. 2014;2(20):7156-7160
- [14] He X, Wang W, Liu Y, Jiang M, Wu F, Deng K, et al. Microfluidic fabrication of bio-inspired microfibers with controllable magnetic spindle-knots for 3d assembly and water collection. *ACS Applied Materials & Interfaces*. 2015;7(31):17471-17481
- [15] Tian Y, Zhu P, Tang X, Zhou C, Wang J, Kong T, et al. Large-scale water collection of bioinspired cavity-microfibers. *Nature Communications*. 2017;8:1080

- [16] Zhu H, Guo Z, Liu W. Biomimetic water-collecting materials inspired by nature. *Chemical Communications*. 2016;**52**(20):3863-3879
- [17] Bai H, Ju J, Sun R, Chen Y, Zheng Y, Jiang L. Controlled Fabrication and Water Collection Ability of Bioinspired Artificial Spider Silks. *Advanced Materials*. 2011;**23**(32):3708
- [18] Chen Y, Wang L, Xue Y, Jiang L, Zheng Y. Bioinspired tilt-angle fabricated structure gradient fibers: micro-drops fast transport in a long-distance. *Scientific Reports*. 2013;**3**:2927
- [19] Zhao L, Song C, Zhang M, Zheng Y. Bioinspired heterostructured bead-on-string fibers via controlling the wet-assembly of nanoparticles. *Chemical Communications*. 2014;**50**(73):10651-10654
- [20] Quere D, Dimeglio JM, Brochardwyart F. Spreading of liquids on highly curved surfaces. *Science*. 1990;**249**(4974):1256-1260
- [21] Bai H, Sun R, Ju J, Yao X, Zheng Y, Jiang L. Large-scale fabrication of bioinspired fibers for directional water collection. *Small*. 2011;**7**(24):3429-3433
- [22] Loscertales IG, Barrero A, Guerrero I, Cortijo R, Marquez M, Ganan-Calvo AM. Micro/nano encapsulation via electrified coaxial liquid jets. *Science*. 2002;**295**(5560):1695-1698
- [23] Sun ZC, Zussman E, Yarin AL, Wendorff JH, Greiner A. Compound core-shell polymer nanofibers by co-electrospinning. *Advanced Materials*. 2003;**15**(22):1929
- [24] Li D, McCann JT, Xia YN. Use of electrospinning to directly fabricate hollow nanofibers with functionalized inner and outer surfaces. *Small*. 2005;**1**(1):83-86
- [25] Song C, Zhao L, Zhou W, Zhang M, Zheng Y. Bioinspired wet-assembly fibers: From nanofragments to microhumps on string in mist. *Journal of Materials Chemistry A*. 2014;**2**(25):9465-9468
- [26] Zhang M, Zheng Y. Bioinspired structure materials to control water-collecting properties. *Materials Today- Proceedings*. 2016;**3**(2):696-702
- [27] Tian X, Bai H, Zheng Y, Jiang L. Bio-inspired heterostructured bead-on-string fibers that respond to environmental wetting. *Advanced Functional Materials*. 2011;**21**(8):1398-1402
- [28] Dong H, Wang N, Wang L, Bai H, Wu J, Zheng Y, et al. Bioinspired electrospun knotted microfibers for fog harvesting. *ChemPhysChem*. 2012;**13**(5):1153-1156
- [29] Thakur N, Ranganath AS, Agarwal K, Baji A. Electrospun bead-on-string hierarchical fibers for fog harvesting application. *Macromolecular Materials and Engineering*. 2017;**302**(7):1700124
- [30] Ganesh VA, Ranganath AS, Baji A, Raut HK, Sahay R, Ramakrishna S. Hierarchical structured electrospun nanofibers for improved fog harvesting applications. *Macromolecular Materials and Engineering*. 2017;**302**(2):1600387
- [31] Du M, Zhao Y, Tian Y, Li K, Jiang L. Electrospun multiscale structured membrane for efficient water collection and directional transport. *Small*. 2016;**12**(8):1000-1005
- [32] Melin J, Quake SR. Microfluidic large-scale integration: The evolution of design rules for biological automation.

Annual Review of Biophysics and Biomolecular Structure. 2007;**36**: 213-231

[33] Ji X, Guo S, Zeng C, Wang C, Zhang L. Continuous generation of alginate microfibers with spindle-knots by using a simple microfluidic device. *RSC Advances*. 2015;**5**(4): 2517-2522

[34] Li X, Liu Y, Zhou H, Gao C, Li D, Hou Y, et al. Fog collection on a bio-inspired topological alloy net with micro-/nanostructures. *ACS Applied Materials & Interfaces*. 2020;**12**(4): 5065-5072

[35] Liu Y, Yang N, Li X, Li J, Pei W, Xu Y, et al. Water harvesting of bioinspired microfibers with rough spindle-knots from microfluidics. *Small*. 2020;**16**(9):1901819

[36] Zhong L, Zhu L, Li J, Pei W, Chen H, Wang S, et al. Recent advances in biomimetic fog harvesting: Focusing on higher efficiency and large-scale fabrication. *Molecular Systems Design & Engineering*. 2021;**6**(12):986-996

[37] Ju J, Bai H, Zheng Y, Zhao T, Fang R, Jiang L. A multi-structural and multi-functional integrated fog collection system in cactus. *Nature Communications*. 2012;**3**:1247

[38] Martorell C, Ezcurra E. The narrow-leaf syndrome: A functional and evolutionary approach to the form of fog-harvesting rosette plants. *Oecologia*. 2007;**151**(4):561-573

[39] Elbaum R, Zaltzman L, Burgert I, Fratzl P. The role of wheat awns in the seed dispersal unit. *Science*. 2007; **316**(5826):884-886

[40] Guo P, Zheng Y, Liu C, Ju J, Jiang L. Directional shedding-off of water on

natural/bio-mimetic taper-ratchet array surfaces. *Soft Matter*. 2012;**8**(6): 1770-1775

[41] Gursoy M, Harris MT, Carletto A, Yaprak AE, Karaman M, Badyal JPS. Bioinspired asymmetric-anisotropic (directional) fog harvesting based on the arid climate plant *Eremopyrum orientale*. *Colloids and Surfaces A-Physicochemical and Engineering Aspects*. 2017;**529**:959-965

[42] Gleiche M, Chi LF, Gedig E, Fuchs H. Anisotropic contact-angle hysteresis of chemically nanostructured surfaces. *ChemPhysChem*. 2001;**2**(3): 187-191

[43] Li D, Feng S, Xing Y, Deng S, Zhou H, Zheng Y. Directional bouncing of droplets on oblique two-tier conical structures. *RSC Advances*. 2017;**7**(57): 35771-35775

[44] Xu T, Lin Y, Zhang M, Shi W, Zheng Y. High-efficiency fog collector: Water unidirectional transport on heterogeneous rough conical wires. *ACS Nano*. 2016;**10**(12):10681-10688

[45] Xing Y, Wang S, Feng S, Shang W, Deng S, Wang L, et al. Controlled transportation of droplets and higher fog collection efficiency on a multi-scale and multi-gradient copper wire. *RSC Advances*. 2017;**7**(47):29606-29610

[46] Peng Y, He Y, Yang S, Ben S, Cao M, Li K, et al. Magnetically induced fog harvesting via flexible conical arrays. *Advanced Functional Materials*. 2015; **25**(37):5967-5971

[47] Dan L, Zheng Y. Self-propelled droplet movement on micro/nano anisotropic structures surface. *Chemical Journal of Chinese Universities-Chinese*. 2018;**39**(1):109-114

- [48] Parker AR, Lawrence CR. Water capture by a desert beetle. *Nature*. 2001; **414**(6859):33-34
- [49] White B, Sarkar A, Kietzig A. Fog-harvesting inspired by the *Stenocara* beetle-An analysis of drop collection and removal from biomimetic samples with wetting contrast. *Applied Surface Science*. 2013; **284**:826-836
- [50] Barthlott W, Schimmel T, Wiersch S, Koch K, Brede M, Barczewski M, et al. The salvinia paradox: Superhydrophobic surfaces with hydrophilic pins for air retention under water. *Advanced Materials*. 2010; **22**(21):2325-2328
- [51] Yang Y, Li X, Zheng X, Chen Z, Zhou Q, Chen Y. 3D-printed biomimetic super-hydrophobic structure for microdroplet manipulation and oil/water separation. *Advanced Materials*. 2018; **30**(9):1704912
- [52] Wang Y, Zhang L, Wu J, Hedhili MN, Wang P. A facile strategy for the fabrication of a bioinspired hydrophilic-superhydrophobic patterned surface for highly efficient fog-harvesting. *Journal of Materials Chemistry A*. 2015; **3**(37):18963-18969
- [53] Bai H, Wang L, Ju J, Sun R, Zheng Y, Jiang L. Efficient water collection on integrative bioinspired surfaces with star-shaped wettability patterns. *Advanced Materials*. 2014; **26**(29): 5025-5030
- [54] Zhang L, Wu J, Hedhili MN, Yang X, Wang P. Inkjet printing for direct micropatterning of a superhydrophobic surface: toward biomimetic fog harvesting surfaces. *Journal of Materials Chemistry A*. 2015; **3**(6):2844-2852
- [55] Lee DG, Lee D. Electro-mechanical properties of the carbon fabric composites with fibers exposed on the surface. *Composite Structures*. 2016; **140**: 77-83
- [56] Wu J, Zhang L, Wang Y, Wang P. Efficient and anisotropic fog harvesting on a hybrid and directional surface. *Advanced Materials Interfaces*. 2017; **4**(2):1600801
- [57] Yang X, Song J, Liu J, Liu X, Jin Z. A twice electrochemical etching method to fabricate superhydrophobic-superhydrophilic patterns for biomimetic fog harvest. *Scientific Reports*. 2017; **7**:8816
- [58] Li C, Li M, Ni Z, Guan Q, Blackman BRK, Saiz E. Stimuli-responsive surfaces for switchable wettability and adhesion. *Journal of the Royal Society Interface*. 2021; **18**(179): 20210162

Wettability of Probiotic Powders: Fundamentals, Methodologies, and Applications

*Mohamed Amin Ali, Joël De Coninck
and Hary L. Razafindralambo*

Abstract

Wettability is a macroscopic consequence of microscopic phenomena occurring at the fluid-solid interfaces. This functional property is crucial for the formulation of wettable powders in food and non-food sectors. Basically, powder wettability is mostly assessed through the contact angle measurements of solid particles reacting with dispersing media, by either the sessile drop method or the capillary rise technique. Among the most popular bioactive agents nowadays are probiotics and their metabolites, which are receiving a growing interest for their beneficial effects on our ecosystem health. As live functional ingredients, probiotics are mainly available in a powder form that is sensitive to the environmental stress factors during processing and storage steps. It is therefore crucial to understand and control their wettability, regarding their performance, dispersibility, and stability when probiotic particles come into contact with dispersing media and body fluids. The proposal chapter aims to review: (1) the theoretical aspects of powder wettability by considering compact and porous materials; (2) the analytical tools and methodologies of measurement, including sessile drop and capillary rise methods using models Lucas-Washburn equation and Darcy's law; and (3) the applications to probiotic powders as functional ingredients in food and agricultural sectors.

Keywords: wettability, probiotic powders, contact angle measurement, capillary rise method, porosity, cell surface hydrophobicity, cell viability

1. Introduction

Wettability is a functional property that represents the wetting degree of a solid. Among the macroscopic consequences of nano- and microscopic phenomena occurring at fluid-solid interfaces, it is governed by the balance between adhesive and cohesive forces, representing the assembly strength of different and identical surfaces, respectively [1]. Such phenomena are naturally encountered in our daily life, or technologically shaped for our necessities [2]. The common examples of solid wettability are observed with drops of water standing out on lotus leaves or repelling on waterproof materials, as well as with agrochemical dispersion preparations spreading

on plant surfaces [3–7]. Adhesives, anti-icing, bio-mimicking, boiling, coatings, fibers, freeze-casting, inks, micro/nanoelectromechanical systems, paper, and petrochemicals also take part of a non-exhaustive list of applications involving wettability [8–15].

When an amount of liquid (e.g. drop of water) comes into contact with a porous or nonporous solid surface (e.g. flat or granular solid), its displacement until an equilibrium position depends on the force resulting from the interfacial tensions at the contact line of three immiscible phases (solid/liquid/gas) (**Figure 1**). The changes in the resulting interfacial tension or free energy define the contact angle (CA), which expresses the wetting degree of the solid surface by the liquid phase [16]. When the CA is lower than an arbitrary value (e.g. $\theta < 90^\circ$), the surface is qualified as hydrophilic whereas it is known as hydrophobic for high CA (e.g. $\theta > 90^\circ$). A value superior to 150° is a characteristic of a superhydrophobic surface [17].

For powder materials, the wettability is often quantified by the contact angle (θ) of compressed disc- or packed bed-prepared particles, which depends on the surface and bulk properties, composition of particles, wetting liquid characteristics, and physico-chemical conditions such as the temperature, pH, ionic strength, and so on [18]. The powder wettability plays a crucial role in coating, dispersion as a precursor step to dissolution, and powder processing such as granulation and other practical usages. Several techniques are available for powder wettability determination through the contact angle measurement of solid particles reacting with dispersing media by the static and dynamic sessile drop method or by the capillary rise technique [19].

Most food and non-food (e.g. pharmaceuticals, detergents, minerals) ingredients and products are in powder form, which is constituted by numerous particles and granules, in pure or mixture form of multiple components [20, 21].

There are many powder wettability case studies of either organic or inorganic-based compounds reported in the scientific literature over the last five years (**Table 1**). However, less investigations have been conducted on powders that contain microorganisms such as probiotics and derivative products.

Probiotics are live microorganisms, when administered in adequate doses and under appropriate conditions, and can be benefits for the host through different action mechanisms [33]. In fact, they can act as (1) competitors for nutrients and adhesion sites with intestinal or plant pathogens; (2) metabolite producers, including bacteriocins, organic acids, antioxidants, enzymes, and biosurfactants; and (3) immunomodulators [34]. Often used as functional ingredients, probiotics find their potential applications in foods, feeds, cosmetics, pharmaceuticals, and agriculture sectors [35–39]. Belonging mainly to lactic acid bacteria (LAB) such as *Lactobacilli* and

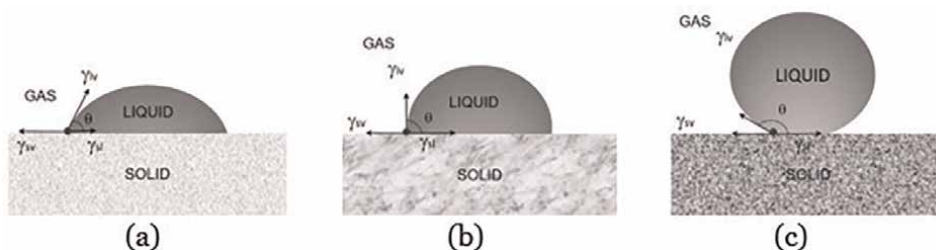


Figure 1. Illustration of liquid drop formed between three immiscible phases with different contact angles θ : (a) hydrophilic $\theta < 90^\circ$, (b) hydrophobic $\theta = 90^\circ$, and (c) superhydrophobic surfaces.

Materials	References
Coffee powder	[22]
Wheat/cereal flours	[23]
Detergent granules	[24]
Pectin agglomerates	[25]
Cocoa beverage powder	[26]
Milk powder	[27]
Excipients	[28]
Drugs	[29]
Silica particles	[30]
Limestone	[31]
Talc	[32]

Table 1.
Examples of wettability studies on various organic and inorganic powders.

Bifidobacteria, or yeasts, probiotics are among the most investigated research topics today, owing to their beneficial effects on our overall ecosystem, involving activities and interactions among human, animal, and plant species, soils and the environment [40].

Their external surfaces are surrounded of components with different molecular classes (e.g. proteins, polysaccharides, peptidoglycans, etc.) and specific structures (e.g. pili), which are responsible for their most surface properties and functionalities such as hydrophobicity, adhesion, and aggregation capacities. Microbial cell surfaces are vital to their survival for interacting with the environment. It is assumed that microbial cells adhere to surfaces through the interactions between extracellular compounds biosynthesized by cells or from external (e.g. coatings) and surfaces [41]. It is generally recognized that there exists a correlation between cell adhesion capacity and surface hydrophobicity, which can be indirectly measured by the water contact angle [42]. Microorganisms are considered hydrophilic for values less than 20° and hydrophobic for values superior to 50° [43, 44].

Moreover, probiotic-based products are industrially manufactured and commercially available in powder particles, in most cases under various solid states rather than dispersed in liquid forms, by successive fermentation, liquid–solid phase separation, and drying processes [45]. It is therefore important to focus scientifically and technologically on the probiotic powder wettability, which is a performance indicator, directly or indirectly in terms of (1) cell capacity in adhering to surfaces; (2) product dispersibility in a fluid for some preparations before use in formulations or uptake as diet supplementation; (3) cell viability and product stability for limiting the contact with humidity and air through the powder porosity or permeability; and (4) coating material compatibility and processing efficiency for cell protection.

The current chapter deals successively with (1) the theoretical aspects of powder wettability; (2) the practical methods and techniques of wettability determination; and (3) the applications to probiotic powder wettability for food and agricultural products.

2. Theoretical aspects on powder wettability

2.1 Basics on contact angle

When a water drop enters in contact with a surface, or a liquid comes in contact with a vertical and infinitely wide plate or porous solid and powders, and rises by capillary effect, the contact angle gives an insight of these wetting phenomena. With a macroscopic view, the contact angle represents the angle formed at the intersection of the interfaces liquid-solid and liquid-vapor by applying a tangent line at a point from the so-called “three-phase contact line”, where the solid, liquid, and vapor phases co-exist (see **Figure 1a**). Contact angles are not only limited to the liquid-vapor interface on a solid but also applicable to the liquid-liquid interface on a solid. Depending on the media (surface or porous structure), the contact angle measurement and the tool to be used are different.

2.2 Flat surface (Young’s equation)

On an ideal flat surface (partial wetting), Young’s equation allows the determination of the liquid contact angle in equilibrium θ_e . It represents the static contact angle value based on the interfacial energy balance between the solid, liquid, and gas surrounding the liquid at the triple line contact (**Figure 2**). Young described first the entire phenomenon in 1805, which was mathematically formalized by Dupré while also discovered elsewhere by Laplace. Thus, this Young-Dupré law is commonly called “Young-Laplace equation” [46–49].

2.3 Rough surfaces (Wenzel model & Cassie-Baxter model)

In the case of non-ideal flat surfaces (roughness added), two contact angle measurements are involved. On the one hand, the Wenzel model adds roughness to



Figure 2. Flat solid surface cases: (a) Young’s equation; (b) liquid drop with an equilibrium contact angle (θ_e).

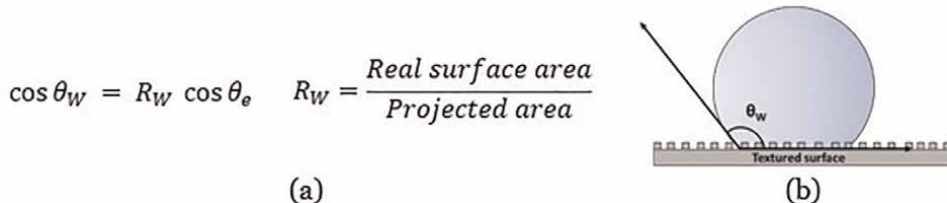
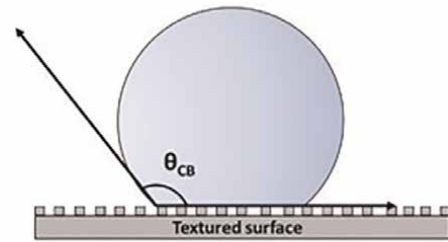


Figure 3. Rough surfaces described by the Wenzel model: (a) apparent contact angle θ_w determination, θ_e being the equilibrium value used in Eq. (1), and $R_W \geq 1$ represents the ratio between the real surface area over the projected area; (b) drop in Wenzel state.

$$\cos \theta_{CB} = f_A \cos \theta_A + f_B \cos \theta_B \text{ (Eq.2)}$$

$$f_A + f_B = 1$$

$$\cos \theta_{CB} = f_A (1 + \cos \theta_A) - 1$$



(a)

(b)

Figure 4. Rough surfaces described by the Cassie-Baxter model: (a) Cassie-Baxter contact angle θ_{CB} determination, f_A and f_B being the fractions of surfaces A and B; (b) drop in Cassie-Baxter state.

complete Young equation (Eq. (1)), and on the other hand, the Cassie-Baxter model depicts surfaces with chemical heterogeneities.

2.3.1 Wenzel model

The Wenzel model illustrates how the drop is in contact through the roughness of surfaces that Young's equation does not take into account. Thus, the drop is pinned on the surface, forming an apparent value of contact angle, which is different to the equilibrium one (**Figure 3**). This angle is modified by a factor called the Wenzel roughness R_w [50–54].

Such phenomenon appears when the solid surface is completely in contact with liquid under the droplet. However, air can be trapped below the drop that tends to lower its energy (e.g. fakir and nails board). In this situation, the drop contact angle is described by the Cassie-Baxter model.

2.3.2 Cassie-Baxter model

The Cassie-Baxter model describes the rough surface as a succession of two different surfaces SA and SB with a resulting wettability that depends on two contact angles θ_A and θ_B [53, 55, 56]. In this case, the contact angle θ_{CB} is a function of the fractions of surfaces A, a first-level roughness feature with solid width and air spacing structure, and surfaces B, a second level roughness at the base of a second-level capillary bridge (**Figure 4**), as defined in Eq. (2).

Theoretical studies show the importance of roughness and its impact on the Wenzel to Cassie-Baxter transition. In fact, the double scale roughness is not always the key parameter to enhance the transition. This also depends on R_w factor and the decrease of f_A [57–59].

2.4 Capillary rise phenomenon (Washburn & Darcy models)

Trees, oil extracting, ink absorption, liquids and sponge, sugar and coffee are among common applications where one can witness a capillary rise phenomenon. It has been described many years, even centuries, ago. When a both-side opened tube is approached to a liquid reservoir surface, the liquid tends to fill the tube. The thinner the tube, the higher the liquid rises inside. The height or height square (or the

equivalent mass) versus time is always monitored. This curve has two parts, a dynamic component (rising) and a steady state component. At certain time, the liquid reaches a limit height (h) represented by Jurin's law (Steady state) represented by Eq. (3) [48, 60].

$$h = \frac{2\gamma \cos \theta_e}{\rho g R} \quad (1)$$

where θ_e is the contact angle, R the radius of the tube, ρ the density of the liquid, γ the surface tension, and g the gravity.

2.4.1 Lucas-Washburn model

The dynamic part of the capillary rise is driven by the Lucas-Washburn equation (LWE). As it is a time-dependent phenomenon [5, 48, 61–66], the equation analytical expression including the gravity and inertia parts is:

$$\frac{2}{R} \gamma \cdot \cos(\theta_e) = \rho g h + \frac{8}{R^2} \eta h \cdot \frac{dh}{dt} + \rho \cdot \left(h \frac{d^2h}{dt^2} + \left(\frac{dh}{dt} \right)^2 \right) \quad (2)$$

where R represents the radius of the tube, ρ the density of the liquid, γ the surface tension, g the gravity, and η : viscosity.

By neglecting the gravity and inertia and assuming h to 0 when time equals 0, and using the Taylor's expansion [67], the LWE is obtained from the above equation:

$$h = \sqrt{\frac{2t}{b}} \quad (3)$$

where

$$b = (8/R^2) / \rho \cos(\theta_e)$$

By replacing the height h with the mass m of the liquid through the relation $m = \rho \cdot \pi R^2 h$ [68, 69], the following equation can be obtained:

$$m(t) = \frac{\rho 2\pi R^5 \gamma \cos \theta}{2\eta} \cdot t \quad (4)$$

This Lucas-Washburn's equation possesses limitation because the inertial forces are neglected.

2.4.2 Darcy model

The capillary rise previously presented does not take into account the permeability, even though there is a capillary constant in the LWE (geometry of the porous material). However, the approximation done with the critical radius is not enough to determine the permeability of materials (porosity). Darcy's law describes thus the wicking in porous media.

Darcy's discovery in 1856 was based on the study of the Dijon fountains, the ground water, and permeability by defining through theoretical and experimental works a universal formula related to the flux of water in sand [48, 70–72]. By changing the pressure (height of the reservoir), a linear relation between the flux and the pressure was observed, which was at the origin of Darcy's law, as follows:

$$h(t) \cdot \frac{dh(t)}{dt} = \frac{k}{\eta} \cdot \frac{\gamma}{R} \quad (5)$$

where k being the porous material permeability (can be related to viscosity), R : radius of the section, η : viscosity, and γ : surface tension.

By integrating the Darcy equation, it is easy by using the previous arguments to write

$$h = \sqrt{\frac{2 \cdot t}{b_{eff}}} \quad (6)$$

where

$$b_{eff} = \frac{\eta R}{k \cdot \gamma} = \frac{\frac{8}{R^2} \eta}{\frac{2}{R} \gamma \cdot \cos(\theta_c)} = \frac{4\eta}{\gamma \cdot R \cdot \cos(\theta_c)} \quad (7)$$

From Eqs. (8) and (9), we can deduce

$$h = \sqrt{\frac{2 \cdot k \cdot \gamma \cdot t}{R \cdot R_{eff}}} \quad (8)$$

This equation indicates that the permeability k is proportional to h^2 and R_{eff} represents the effective radius. From the kinematics of the imbibition in a porous media, the effective radius can thus be extracted, characterizing its permeability or equivalently its porosity.

3. Practical methods for powder wettability determination

The wettability of powders can be determined by various techniques described in detail by Alghunaim et al. [19]. These include the sessile drop, Wilhelmy plate, and liquid penetration methods. In this section, only two practical methods of contact angle measurements based on the sessile drop and capillary rise are briefly described for their possible application to probiotic powders (Section 4).

3.1 Sessile drop method

The sessile drop method can be applied to solid surface prepared after compacting powder in a disc or pellet under well-defined conditions of high pressure (70–700 MPa). It is the most common technique for determining the wettability of powders. The static contact angle measurement is performed by depositing a small amount of liquid drop on the disc or pellet while recording its spreading. A software is always

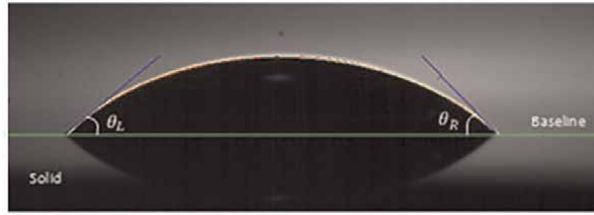


Figure 5.
Drop of water fitted by a software.

used for analyzing the contact angles (edge detection) with the programmed functions (i.e. straight line, circle or Laplace fitting). In this way the contact angle is extracted by fitting the baseline between the drop/the substrate (interface liquid/solid) and the shape of the drop as represented in **Figure 5**. The method provides the right and left contact angles θ_R and θ_L .

For hydrophobic and superhydrophobic surfaces, other methods like Johnson and Dettre [73] and the sliding method can be used, respectively [74–78]. A hysteresis representing the difference between the advancing and the receding contact angle can be deduced in dynamic measurements [79].

3.2 Capillary rise method

Powder samples are introduced into a glass tube for preparing a packed-bed column with support at the bottom (e.g. filter paper). The tube is then put in contact to a liquid surface, and the liquid penetration front is monitored as a function of time. The change in mass of the sample attached to a microbalance is recorded and plotted against time to obtain the contact angle information. In practice, the packed-bed column is first tested with a completely wettable solvent ($\cos \theta = 1$) for determining the capillary constant R_C from the equation in Section 2.4.1. Once R_C is known, the desired liquid can be used to evaluate the contact angle θ . This method has a limitation because one assumes that the porous material is comparable to a succession of fine tube each one having a critical radius R_C (**Figure 6**). Assuming this fact is not representative for all porous materials [80–84]. Indeed, powder and fiber bundles are more complicated because the pores are not always vertical. The porous material possesses

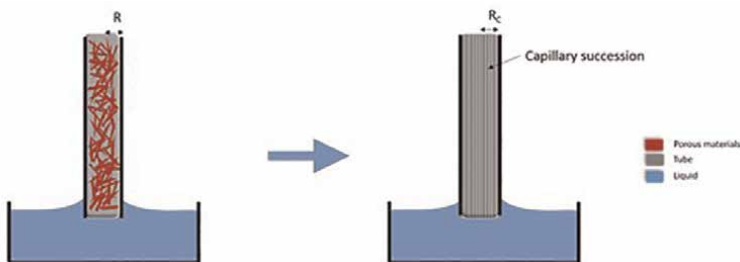


Figure 6.
Analogy between real porous material and capillary succession approximation.

its own distribution inside the tube. Therefore, the way how the powder and the fibers are compact plays a key role in the robustness and the repeatability of the results.

4. Applications to probiotic powders

The wettability of probiotic powders is first a good indicator of surface cell hydrophobicity, and therefore the cell adhesion capacity through liquid contact angle measurements. Such a functional property is also important for powder product dispersibility and compatibility with coating materials.

Probiotic powders are heterogeneous and complex solid materials that generate high variability data of water contact angle measurements. Therefore, the determination of their wettability is a difficult task and needs a judicious choice of available techniques and methods. In this section, we first describe and discuss the different methodologies used for probiotic powders before illustrating their practical importance in food and agricultural areas.

4.1 Surface wettability

A first approach is to prepare a compact surface by compressing the probiotic powder sample under high pressure conditions for making pellets, and then measuring the liquid contact angle by the sessile drop method. This method has been used for the first time for determining the water angle contact of the cell surface of the probiotic multistrain sample [85]. Neither visible cracks nor chemical alteration has been observed before and during the measurement of the static contact angle. This method has provided similar results compared to the static advancing water contact angle technique used for the same sample [45]. The combination of the sessile drop method with the compressed disc preparation under well-defined press conditions provides reproducible data and appears as a very practical methodology for determining the probiotic surface contact angles.

A second approach is to prepare a multilayer or lawn of probiotics by passing through an appropriate filter a liquid dispersion of powder particles under vacuum. The filter on which the probiotic lawn adheres is then treated by a first step of moisture equilibration time for several minutes, followed by a second one of air drying. This is the most commonly used method for determining the liquid contact angle, and distinguishing hydrophobic microorganisms to hydrophilic ones [43]. It has some advantages in preparing smooth and homogenous microorganism layers, and is more convenient for fragile cells [86]. Such a procedure has been optimized to lower the variability in the results of contact angles by searching the best moisture equilibrium time and moisturizing medium [43]. Through this method, it has, for instance, recently been shown the contribution of two main probiotic components (*L. bulgaricus* and *S. thermophilus*) of a multistrain sample (vivomixx) for their respective surface hydrophilicity [45]. Some water contact angle data measured by this technique are available in the literature for some bacterial probiotics such as *L. acidophilus* (66–80°), *L. rhamnosus* (33–86°), *L. plantarum* (25–79°), and *S. thermophilus* (23°).

4.2 Bulk wettability

A third approach to assess the wettability of probiotic powder is the use of the capillary rise technique measuring the amount of liquid penetrating a bed column of

sample over time, and applying a mathematical model that fits the penetrating rate profile of a liquid up a tube packed. Even though the capillary rise technique is by far the popular method for determining contact angles of powders or porous materials [69], it has rarely been applied to probiotic powders. Such a method has, for instance, been used for characterizing the wettability of a multistrain powder sample of probiotics, showing two regimes of the liquid penetrating rate profile [85]. The first one is a power law regime for the first few moments while the second one can be described using Darcy's law. The use of this modeling approach has led to the possibility of assessing the particle-packed bed permeability and porosity through an effective radius determined by the semi-empirical Kozeny-Carman approach [85]. These physical properties are interesting for predicting some performance of probiotic strain such as product stability and cell viability during the powder storage. In fact, high powder porosity or permeability promotes the presence of air (oxygen) and/or moisture in inter- and intra-particle pores, accelerates the oxidative process of cell membranes, and reduces rapidly the cell viability rate.

4.3 Practical use in food and agricultural areas

Most ingredients used in product formulations are available in a powder form, owing to many practical advantages in transportation, handling, processing, formulation, packaging, and stability [20].

The wettability of powders plays important roles in product preparation, engineering, stability, and performance, since it is the first step of powder dispersion that is of crucial importance for the process of making a dispersion [87].

4.3.1 Food applications

For probiotic-based food products and ingredients used in the preparation of fermented foods and diet supplements, the degree of wetting needs to be at the right value for ensuring both good preparation during the hydration and high stability during the storage. Some examples of commercialized products are listed in **Table 2**. Probiotic powders are currently formulated with a mixture of components, including mono- or multistrain microorganisms and other active and functional ingredients and excipients (e.g. prebiotics, antioxidants, cryoprotectors, anti-agglomerates, diluents, lubricant, colorant, binder, coating agent, sweetening agent, anti-caking agent, binders, etc.) (**Table 3**). Binders are, for instance, adhesives that provide the cohesiveness essential for the bonding of solid particles during the process of agglomeration [88]. Consequently, their wettability is an important criterion for the powder dispersibility when rehydrate or reconstituted, and powder stability related to porosity during the storage. This also impacts the viability of probiotic strains, which are sensitive to the environmental conditions such as humidity and temperature.

The wettability of probiotic powders may vary as a function of other components within their formulations. When the latter contain prebiotics, mainly carbohydrate-based compounds, the products are called synbiotics. It has been demonstrated that prebiotics can change the probiotic surface properties, and therefore would impact the wettability of whole products [89]. It is also well known that free fats in the surface reduce wettability whereas some surface-active agents, especially those exhibiting dispersing capacity commonly improve wettability in dried containing fat products [88].

Products	Microbial probiotics
Infant milk formulation	<i>Lactobacillus rhamnosus</i> <i>Bifidobacterium longum</i>
Oat and rice powder	<i>Bifidus</i> BL
Baking mix	<i>Bacillus coagulans</i>
Passion fruit juice powder	<i>Lactobacillus plantarum</i> S20
Synbiotic goji berry powder	<i>Bifidobacterium animalis</i> subsp. <i>lactis</i> (Bb12), <i>B. longum</i> (Bb46), and <i>Lactobacillus casei</i>
Spray-dried raisin powder	<i>B. coagulans</i>
Almond milk powder	<i>L. plantarum</i> ATCC 8014
Tubers-Cassava	<i>Saccharomyces cerevisiae</i> , <i>L. bulgaricus</i>
VSL#3	<i>Lactobacillus acidophilus</i> , <i>L. plantarum</i> , <i>L. casei</i> , <i>Lactobacillus delbrueckii</i> subsp. <i>bulgaricus</i> , <i>B. breve</i> , <i>B. longum</i> , and <i>B. infantis</i> , <i>Streptococcus salivarius</i> subsp. <i>Thermophilus</i>

Table 2.
 Some examples of commercialized products of probiotic powders.

Excipients in probiotic powders	Functions
Microcrystalline cellulose	Binder/diluent
Rice maltodextrin	Binder/diluent
Silicon dioxide	Gliding/anti-caking agent
Magnesium stearate	Lubricant
Hydroxy propyl methyl cellulose	Suspending/viscosity agent

Table 3.
 Some excipients in probiotic powder formulations.

4.3.2 Agricultural applications

Agricultural applications of probiotic powders include animal and plant health and growth, as illustrated with some examples in **Table 4**. Probiotics have been recognized to be benefits to the host animal as feed supplements and animal products (e.g. poultry, ruminant, pig, and aquaculture) in improving food safety. Their use aims at reducing, even substituting antibiotics to control pathogens in poultry production [90].

For probiotic-based agriproducts such as microbial feed supplements, pesticides, and anti-weeds, an optimum powder wettability is required for ensuring high dispersibility in the liquid media preparation, but also for maximizing the spreading and penetrating properties with regards to the target materials (e.g. plant leaves).

In aquaculture, probiotic activities mainly result from the production of antimicrobial metabolites and the attachment or adhesion to intestinal mucus for competing with pathogens.

Microorganism	Name of product	Plant pathogens/photosystem
<i>Ampelomyces quisqualis M-10</i>	AQ10 Biofungicide	Powdery mildew on fruits
<i>Azospirillum spp.</i>	Biopromoter	Paddy, millets, oilseeds, fruits, vegetables
<i>Bacillus subtilis GB03</i>	Kodiak	Growth promotion; Rhizoctonia
<i>Bacillus pumilus</i>	YieldShield	Soil-born fungal pathogens
<i>Delftia acidovorans</i>	Bioboost	Canola
<i>Pseudomonas chlororaphis</i>	Cedomon	Leaf strip, net blotch
<i>Streptomyces griseoviridis K61</i>	Mycostop	<i>Phomopsis spp.</i> , <i>Botrytis spp.</i>
<i>Trichoderma harzianum T22</i>	RootShield	<i>Pythium spp.</i> , <i>Rhizoctonia solani</i>
<i>Pseudomonas spp.</i>	Proradix	<i>Rhizoctonia solani</i>

Table 4. Applications of probiotic powders in agriculture (adapted from [39]).

Plant health benefits and growths in using probiotics involve direct mechanisms through beneficial microbes-host plant interactions, including adherence and colonization steps, or indirect ones due to the antagonistic activity against plant pathogens. Probiotic plant antagonism includes inhibition, competition for nutrients, and degradation of pathogenicity factors [91].

4.3.3 Probiotic viability and survival applications

Probiotics can provide health benefits when they reach the targets with a high number of viable cells. In fact, many microbial probiotic strains are sensitive to external environmental conditions such as high acidity, moisture, temperature, and oxygen level. Two main strategies can be employed in maintaining the viability, or reducing the mortality of probiotic strains: (1) using additional ingredients such as prebiotics in a synbiotic formulation for supporting cell viability throughout processing, storage, distribution, gastrointestinal, and environmental stress conditions; (2) protecting cells by using encapsulation technology or coating processes.

4.3.3.1 Synbiotic formulations

It is recognized that combining prebiotics and probiotics together in synbiotic powder formulations may boost the viability of probiotic strains [89]. Prebiotics are substrates that serve as probiotic nutrients, and mainly consist of carbohydrate compounds such as inulin, oligosaccharides (e.g. GOS, XOS), and fructooligosaccharides [92]. Thus, the wettability of their mixture is an important indicator for ensuring the synbiotic performance, either in synergism or in complementary [93], dispersibility in a fluid, and stability during storage.

4.3.3.2 Encapsulation and coating processes

Encapsulation and coating processes are often used for protecting the probiotics and synbiotics against environmental stress conditions in order to maintain a high level of viability, stability, and performance [94]. It uses various food-grade

biopolymers, mostly derived from polysaccharides (e.g. gum Arabic, alginate, chitosan, resistant starch, etc.) and proteins (e.g. milk and soy proteins), and different technologies, including the bulk or microscale matrix encapsulation systems and the individual cell encapsulation via nanocoatings [95]. The first method is based on the immobilization of probiotics into a gel matrix (e.g. hydrogel systems) whereas the second one is based on the formation of nanofilms around individual probiotic cells (e.g. cytoprotective approaches based on silica, graphene, metal-polyphenol nanoshells, etc.).

In both cases, the wettability of probiotic powders before and after encapsulation or coating processes appears important for operating convenient choices of coating agents and processes but also for the final product performance. In fact, the microbial probiotic surface properties such as hydrophobicity and polarity as well as the permeability/porosity of the powder have an impact on the compatibility and interactions with the coating or encapsulation materials for ensuring an appropriate stability and permeability of the formulated products. Based on several investigations, the survival rate of probiotic strains may vary between 68 and 94% during the storage and digestion, depending on the coating or encapsulating materials and methodologies used [94]. Nevertheless, such protective processes are not necessary for the spore-forming bacteria such as *Bacillus* strains which convert from vegetative into resistant spore forms by naturally producing a protective shell under harsh conditions, including high temperature, pressure, and acidity, as well as heat, desiccation, radiation, and oxidation conditions [95]. It might also be the case of *Lactobacillus* strains through self-encapsulation mechanisms by producing a thicker layer of EPS, when the environmental factors and stress conditions of fermentation are modified [96].

5. Conclusion

The wettability of probiotic powders deserves a great scientific and technological attention, as for other food and non-food ingredients and products in various sectors. Beyond its evident importance in the dispersibility and stability of the powder containing live microorganisms and other components in contact with fluids, it is a crucial indicator of the cell adhesion capacity and cell viability improvement through encapsulation and coating processes. Its accurate determination with the appropriate techniques and data processing models is the key to progress in getting insight into the probiotic action mechanisms, and in improving the probiotic containing product qualities and performance. However, there are only a few available scientific data from probiotic powder wettability studies in the literature compared to contact angle measurements with various techniques. Three sample preparation and measurement techniques such as powder compact discs and microbial lawns by sessile drop, and a packed-bed column using rise capillary, can be distinguished. Subsequently, two fitting models based on Washburn equation and Darcy's law may be used based on the experimental recorded data. In particular, Darcy's law combined with the semi-empirical Kozeny-Carman approach provides a potential prediction of powder porosity or permeability. This methodology will open a new research route on the impact of the microbial powder particle size, shape, aggregation, adhesion, biofilm formation on the formulation performance and product stability, as well as on the cell viability and activities for human, animal, plant, and environment, in short, on our ecosystem health.

Acknowledgement

This work has received funding by the European Union's Horizon Europe Research, innovation programme through URBANE under the grant Agreement 101059232.

Author details

Mohamed Amin Ali¹, Joël De Coninck¹ and Hary L. Razafindralambo^{2,3*}


1 Physics of Surfaces and Interfaces Laboratory, UMONS, Belgium

2 ProBioLab, Campus Universitaire de la Faculté de Gembloux Agro-Bio Tech/ Université de Liège, Gembloux, Belgium

3 BioEcoAgro Joint Research Unit, TERRA Teaching and Research Centre, Microbial Processes and Interactions, Gembloux Agro-Bio Tech/Université de Liège, Gembloux, Belgium

*Address all correspondence to: h.razafindralambo@uliege.be

IntechOpen

© 2022 The Author(s). Licensee IntechOpen. This chapter is distributed under the terms of the Creative Commons Attribution License (<http://creativecommons.org/licenses/by/3.0>), which permits unrestricted use, distribution, and reproduction in any medium, provided the original work is properly cited. 

References

- [1] Ravera F. The contact angle as an analytical tool. In: *Colloid and Interface Chemistry for Nanotechnology*. Boca Raton, FL: CRC Press; 2016. pp. 271-286
- [2] Dhyani A, Wang J, Halvey AK, Macdonald B, Mehta G, Tuteja A. Design and applications of surfaces that control the accretion of matter. *Science*. 2021;**373**: eaba5010. DOI: 10.1126/science.aba5010
- [3] Blossey R. Self-cleaning surfaces—Virtual realities. *Nature Materials*. 2003; **2**:301-306. DOI: 10.1038/nmat856
- [4] Cassie ABD, Baxter S. Large contact angles of plant and animal surfaces. *Nature*. 1945;**155**:21-22. DOI: 10.1038/155021a0
- [5] Liu M, Wang S, Jiang L. Nature-inspired superwettability systems. *Nature Reviews Materials*. 2017;**2**:1-17. DOI: 10.1038/natrevmats.2017.36
- [6] Lm SJ, Kim D, Kim Y, Jeong S, Pang C, Ryu S, et al. Hydrophobicity evolution on rough surfaces. *Langmuir*. 2020;**36**: 689-696. DOI: 10.1021/acs.langmuir.9b02292
- [7] Tian X, Verho T, Ras RHA. Moving superhydrophobic surfaces toward real-world applications. *Science*. 2016;**352**: 142-143. DOI: 10.1126/science.aaf2073
- [8] Bertrand E, Coninck TB. Dynamics of dewetting. *Colloids and Surfaces A: Physicochemical and Engineering Aspects*. 2010;**369**:141-147
- [9] Bharathidasan T, Kumar V, Bobji M, Basu BJ, Chakradhar R. Effect of wettability and surface roughness on ice-adhesion strength of hydrophilic, hydrophobic and superhydrophobic surfaces. *Applied Surface Science*. 2014; **314**:241-250
- [10] Bourdon B, Rioboo R, Marengo M, Gosselin E, De Coninck J. Influence of the wettability on the boiling onset. *Langmuir*. 2012;**28**:1618-1624
- [11] Davarpanah A, Zarei M, Nassabeh M. An overview of wettability measurements in fractured carbonated reservoir and investigate the effects of wettability changes in the optimization of enhanced oil recovery techniques. *International Journal of Petroleum and Petrochemical Engineering*. 2017;**3**:54-59
- [12] Bernard-Granger G, Deville S. Influence of surface tension, osmotic pressure and pores morphology on the densification of ice-templated ceramic. *Journal of the European Ceramic Society, Elsevier*. 2011;**6**:983-987
- [13] Kubiak K, Wilson M, Mathia T. Methodology for metrology of wettability versus roughness of engineering surfaces. *Wear*. 2011;**271**: 523-528
- [14] Phan HT, Caney N, Marty P, Gavillet J, Colasson S. Surface wettability control by nanocoating: The effects on pool boiling heat transfer and nucleation mechanism. *International Journal of Heat and Mass Transfer*. 2009;**52**:5459-5471
- [15] Schneider M. *Wettability Patterning in Microfluidic Systems and Applications in the Petroleum Industry*. Diss. Université Pierre et Marie Curie-Paris VI. 2011
- [16] Lazghab M, Saleh K, Pezron I, Guigon P, Komunjer L. Wettability assessment of finely divided solids. *Powder Technology*. 2005;**157**:79-91
- [17] Yamamoto M, Nishikawa N, Mayama H, Nonomura Y, Yokojima S,

Nakamura S, et al. Theoretical explanation of the lotus effect: Superhydrophobic property changes by removal of nanostructures from the surface of a lotus leaf. *Langmuir*. 2015; **31**:7355-7363. DOI: 10.1021/acs.langmuir.5b00670

[18] Xue C, Lott JT, Kolachalama VB. Estimation of size and contact angle of evaporating sessile liquid drops using texture analysis. *Langmuir*. 2019;**35**: 3672-3679. DOI: 10.1021/acs.langmuir.8b04043

[19] Alghunaim A, Kirdponpattara S, Newby BZ. Techniques for determining contact angle and wettability of powders. *Powder Technology*. 2016;**287**: 201-215

[20] Bhandari BR. Introduction to food powders. In: *Handbook of Powders*. Woodhead Publishing; 2013. pp. 1-25

[21] Buckton G. Solid-state properties. In: Aulton ME, editor. *Aulton's Pharmaceutics: The Design and Manufacture of Medicines*, 3rd ed. Edinburgh, New York: Churchill Livingstone; 2007

[22] Vimercati WC, Araújo C d S, Macedo LL, Correa JLG, Pimenta CJ. Encapsulation of coffee silverskin extracts by foam mat drying and comparison with powders obtained by spray drying and freeze-drying. *Journal of Food Science*. 2022;**87**:1767-1779. DOI: 10.1111/1750-3841.16102

[23] Roman-Gutierrez A, Sabathier J, Guilbert S, Galet L, Cuq B. Characterization of the surface hydration properties of wheat flours and flour components by the measurement of contact angle. *Powder Technology*. 2003;**129**:37-45

[24] Germaná S, Simons S, Bonsall J, Carroll B. LAS acid reactive binder:

Wettability and adhesion behaviour in detergent granulation. *Powder Technology*. 2009;**189**:385-393

[25] Hirata TAM, Dacanal GC, Menegalli FC. Effect of operational conditions on the properties of pectin powder agglomerated in pulsed fluid bed. *Powder Technology*. 2013;**245**:174-181

[26] Abdelaziz IB, Sahli A, Bornaz S, Scher J, Gaiani C. Dynamic method to characterize rehydration of powdered cocoa beverage: Influence of sugar nature, quantity and size. *Powder Technology*. 2014;**264**:184-189

[27] Hammes MV, Englert AH, Noreña CPZ, Cardozo NSM. Study of the influence of soy lecithin addition on the wettability of buffalo milk powder obtained by spray drying. *Powder Technology*. 2015;**277**:237-243

[28] Oka S, Emady H, Kašpar O, Tokárová V, Muzzio F, Štěpánek F, et al. The effects of improper mixing and preferential wetting of active and excipient ingredients on content uniformity in high shear wet granulation. *Powder Technology*. 2015; **278**:266-277

[29] Puri V, Dantuluri AK, Kumar M, Karar N, Bansal AK. Wettability and surface chemistry of crystalline and amorphous forms of a poorly water soluble drug. *European Journal of Pharmaceutical Sciences*. 2010;**40**:84-93

[30] Ouabbas Y, Chamayou A, Galet L, Baron M, Thomas G, Grosseau P, et al. Surface modification of silica particles by dry coating: Characterization and powder ageing. *Powder Technology*. 2009;**190**:200-209

[31] Diederich P, Mouret M, de Ryck A, Ponchon F, Escadeillas G. The nature of limestone filler and self-consolidating

- feasibility—Relationships between physical, chemical and mineralogical properties of fillers and the flow at different states, from powder to cement-based suspension. *Powder Technology*. 2012;**218**:90-101
- [32] Lefebvre G, Galet L, Chamayou A. Dry coating of talc particles with fumed silica: Influence of the silica concentration on the wettability and dispersibility of the composite particles. *Powder Technology*. 2011;**208**:372-377
- [33] Hill C, Guarner F, Reid G, Gibson GR, Merenstein DJ, Pot B, et al. Expert consensus document: The International Scientific Association for Probiotics and Prebiotics consensus statement on the scope and appropriate use of the term probiotic. *Nature Reviews Gastroenterology & Hepatology*. 2014; **11**:506
- [34] Oelschlaeger TA. Mechanisms of probiotic actions—A review. *International Journal of Medical Microbiology*. 2010;**300**:57-62
- [35] Chaucheyras-Durand F, Durand H. Probiotics in animal nutrition and health. *Beneficial Microbes*. 2009;**1**:3-9. DOI: 10.3920/BM2008.1002
- [36] Puebla-Barragan S, Reid G. Probiotics in cosmetic and personal care products: Trends and challenges. *Molecules*. 2021;**26**:1249. DOI: 10.3390/molecules26051249
- [37] Razafindralambo H, editor. *Trends in Probiotic Applications*. Studium Press LLC; 2018
- [38] Schisler DA, Slininger PJ, Behle RW, Jackson MA. Formulation of *Bacillus* Spp. for biological control of plant diseases. *Phytopathology*. 2004;**94**: 1267-1271. DOI: 10.1094/PHYTO.2004.94.11.1267
- [39] Song D, Ibrahim S, Hayek S. Recent application of probiotics in food and agricultural science. In: *Probiotics*. London, UK: IntechOpen; 2012. pp. 3-36
- [40] Ebenso B, Otu A, Giusti A, Cousin P, Adetimirin V, Razafindralambo H, et al. Nature-based One Health approaches to urban agriculture can deliver food and nutrition security. *Frontiers in Nutrition*. 2022;**9**:1-9
- [41] Dubiel EA, Martin Y, Vermette P. Bridging the gap between physicochemistry and interpretation prevalent in cell-surface interactions. *Chemical Reviews*. 2011;**111**:2900-2936
- [42] Busscher HJ, Weerkamp AH, van der Mei HC, Van Pelt AW, de Jong HP, Arends J. Measurement of the surface free energy of bacterial cell surfaces and its relevance for adhesion. *Applied and Environmental Microbiology*. 1984;**48**: 980-983
- [43] Eschlbeck E, Kulozik U. Effect of moisture equilibration time and medium on contact angles of bacterial spores. *Journal of Microbiological Methods*. 2017;**135**:1-7
- [44] Rijnaarts HH, Norde W, Bouwer EJ, Lyklema J, Zehnder AJ. Bacterial adhesion under static and dynamic conditions. *Applied and Environmental Microbiology*. 1993;**59**:3255-3265
- [45] Razafindralambo H, Delvigne F, Blecker C. Physico-chemical approach for characterizing probiotics at the solid and dispersed states. *Food Research International*. 2019;**116**:897-904
- [46] Laplace PS. *Mécanique Céleste*, Suppl. au X. Livre, Coureier: Paris; 1805
- [47] Makkonen L. Young's equation revisited. *Journal of Physics. Condensed Matter*. 2016;**28**:4

- [48] Martic G. Dynamique de la Montée Capillaire. Diss. Faculté Polytechnique de Mons. 2006
- [49] Young T. An essay on the cohesion of fluids. *Philosophical Transactions of the Royal Society*. 1805;**95**:65-87
- [50] Quéré D, Lafuma A. Superhydrophobic states. *Nature Materials*. 2003;**2**:457-460
- [51] Eral HB, ‘t Mannetje DJCM, Oh JM. Contact angle hysteresis: A review of fundamentals and applications. *Colloid and Polymer Science*. 2013;**291**:247-260
- [52] Okumura K, Ishino C. Wetting transitions on textured hydrophilic surfaces. *The European Physical Journal E*. 2008;**25**:415-424
- [53] Shin S, Seo J, Han H, Kang S, Kim H, Lee T. Bio-inspired extreme wetting surfaces for biomedical applications. *Materials*. 2016;**9**:1-26
- [54] Wenzel R. Resistance of solid surfaces to wetting by water. *Industrial and Engineering Chemistry*. 1936;**28**: 988-994
- [55] Cassie A. Contact angles. *Discussions of the Faraday Society*. 1948;**3**:11-16
- [56] Baxter S, Cassie ABD. Wettability of porous surfaces. *Transactions of the Faraday Society*. 1944;**40**:546-551
- [57] Coninck J, Huillet T, Dunlop F. Wetting in 1+1 dimensions with two-scale roughness. *Physica A*. 2015;**438**: 398-415
- [58] Nicola F, Castrucci P, Scarselli M, Nanni F, Crescenzi IC. Multi-fractal hierarchy of single-walled carbon nanotube hydrophobic coatings. *Scientific Reports*. 2015;**5**:1-9
- [59] Thévenin R. Superhydrophobie Active. PhD Thesis, Ecole Polytechnique, Université Paris-Saclay. 2014
- [60] Jurin J. *Disquisitio Physicae de Tubulis Capillaribus. Commentarii Academiae Scientiarum Imperialis Petropolitanae*. 1728;**3**:281-292
- [61] Fries N, Dreyer M. An analytic solution of capillary rise restrained by gravity. *Journal of Colloid and Interface Science*. 2008;**320**:259-263. DOI: 10.1016/j.jcis.2008.01.009
- [62] Hamraoui A, Nylander T. Analytical approach for the Lucas–Washburn equation. *Journal of Colloid and Interface Science*. 2002;**250**:415-421. DOI: 10.1006/jcis.2002.8288
- [63] Lucas R. The time law of the capillary rise of liquids. *Kolloid-Zeitschrift*. 1918;**23**:15-22
- [64] Washburn EW. The dynamics of capillary flow. *Physical Review*. 1921;**17**: 273-283. DOI: 10.1103/PhysRev.17.273
- [65] Zaccardi YV, Belie NA. Lucas-Washburn vs Richards equation for the modelling of water absorption in cementitious materials. In: *MATEC Web of Conferences*. Les Ulis, France: EDP Sciences; 2018
- [66] Zhmud BV, Tiberg F, Hallstensson K. Dynamics of capillary rise. *Journal of Colloid and Interface Science*. 2000;**228**: 263-269. DOI: 10.1006/jcis.2000.6951
- [67] Terzaghi K. *Theoretical Soil Mechanics*. New York: Wiley; 1943
- [68] Dang-Vu T, Hupka J. Characterization of porous materials by capillary rise method. *Physicochemical Problems of Mineral Processing*. 2005; **39**:47-65

- [69] Kirdponpattara S, Phisalaphong M, Newby BMZ. Applicability of Washburn capillary rise for determining contact angles of powders/porous materials. *Journal of Colloid and Interface Science*. 2013;**397**:169-176. DOI: 10.1016/j.jcis.2013.01.033
- [70] Darcy H. *Les fontaines publiques de la ville de Dijon*. Paris: Victor Dalmont éditeur; 1856
- [71] Marle CM. Henry Darcy et les écoulements de fluides en milieu poreux. *Oil & Gas Science and Technology—Revue d'IFP Energies Nouvelles*. 2006; **61**:599-609
- [72] Zerner M. Aux origines de la loi de Darcy. *Documents pour l'histoire des Techniques*. 1856;**20**:29-40
- [73] Rioboo R, Delattre B, Vaillant A, De Cononck J. Superhydrophobicity and liquid repellency of solutions on polypropylene. *Advances in Colloid and Interface Science*. 2012;**175**:1-10
- [74] He H-M, Gao L, Yang X-J, Guo W-H, Li H, Xie T, et al. Studies on the superhydrophobic properties of polypropylene/polydimethylsiloxane/graphite fluoride composites. *Journal of Fluorine Chemistry*. 2013;**156**:158-163
- [75] Jeong D-W, Shin U-H, Kim JH, Kim S-H, Kim J-M, Lee HW. Stable hierarchical superhydrophobic surfaces based on vertically aligned carbon nanotube forests modified with conformal silicone coating. *Carbon*. 2014;**79**:442-449
- [76] Kim J, Ha J, Kim HY. Capillary rise of non-aqueous liquids in cellulose sponges. *Journal of Fluid Mechanics*. 2017;**818**:2. DOI: 10.1017/jfm.2017.165
- [77] Rioboo R, Voué M, Vaillant A, Seveno D, Conti J, Bondar A, et al. Superhydrophobic surfaces from various polypropylenes. *Langmuir*. 2008;**24**: 9508-9514
- [78] Schellenberger F, Encinas N, Butt H-J, D.V. How water advances on superhydrophobic surfaces. *Physical Review Letters*. 2016;**116**: 096101-096106
- [79] Gao L, McCarthy TJ. Contact angle hysteresis explained. *Langmuir*. 2006;**22**: 6234-6237
- [80] Ahadian S, Moradian S, Sharif F, Amani TM, Mohseni M. Prediction of time of capillary rise in porous media using artificial neural network (ANN). *Iranian Journal of Chemistry & Chemical Engineering*. 2007;**26**:71-83
- [81] Alim K, Parsa S, Weitz DA, Brenner MP. Local pore size correlations determine flow distributions in porous media. *Physical Review Letters*. 2017; **119**:144501. DOI: 10.1103/PhysRevLett.119.144501
- [82] Brakel JV. 1975a. *Capillary Liquid Transport in Porous Media*. Ph.D. Dissertation, TH Delft
- [83] Brakel JV. Pore space models for transport phenomena in porous media review and evaluation with special emphasis on capillary liquid transport. *Powder Technology*. 1975b;**11**:205-236. DOI: 10.1016/0032-5910(75)80049-0
- [84] Scheidegger A. *The Physics of Flow through Porous Media*. Toronto: University of Toronto Press; 1974
- [85] Ali MA, Razafindralambo HL, Conti G, De Coninck J. Bulk and surface wettability characteristics of probiotic powders in their compressed disc and packed-bed column forms. *ACS Omega*. 2020;**5**:22348-22355. DOI: 10.1021/acsomega.0c02728

- [86] Van Oss SJ, Gillman CF, Newman AW. Phagocytic Engulfment and Adhesiveness as Cellular Surface Phenomena. New York: Marcel Dekker; 1975
- [87] Freudig B, Hoge Kamp S, Schubert H. Dispersion of powders in liquids in a stirred vessel. *Chemical Engineering and Processing: Process Intensification*. 1999; **38**:525-532. DOI: 10.1016/S0255-2701(99)00049-5
- [88] Dhanalakshmi K, Ghosal S, Bhattacharya S. Agglomeration of food powder and applications. *Critical Reviews in Food Science and Nutrition*. 2011; **51**:432-441
- [89] Pan M, Kumaree KK, Shah NP. Physiological changes of surface membrane in *Lactobacillus* with prebiotics. *Journal of Food Science*. 2017; **82**:744-750. DOI: 10.1111/1750-3841.13608
- [90] Botsoglou NA, Fletouris DJ. *Drug Residues in Foods*. New York: Marcel Dekker; 2000
- [91] Berg G. Plant–microbe interactions promoting plant growth and health: Perspectives for controlled use of microorganisms in agriculture. *Applied Microbiology and Biotechnology*. 2009; **84**:11-18. DOI: 10.1007/s00253-009-2092-7
- [92] Gibson GR, Hutkins R, Sanders ME, Prescott SL, Reimer RA, Salminen SJ, et al. The International Scientific Association for Probiotics and Prebiotics (ISAPP) consensus statement on the definition and scope of prebiotics. *Nature Reviews Gastroenterology & Hepatology*. 2017; **14**:491-502
- [93] Swanson KS, Gibson GR, Hutkins R, Reimer RA, Reid G, Verbeke K, et al. The international scientific Association for Probiotics and Prebiotics (ISAPP) consensus statement on the definition and scope of synbiotics. *Nature Reviews Gastroenterology & Hepatology*. 2020; **17**:687-701
- [94] Rajam R, Subramanian P. Encapsulation of probiotics: Past, present and future. *Beni-Suef University Journal of Basic and Applied Sciences*. 2022; **11**:46. DOI: 10.1186/s43088-022-00228-w
- [95] Centurion F, Basit AW, Liu J, Gaisford S, Rahim MA, Kalantar-Zadeh K. Nanoencapsulation for probiotic delivery. *ACS Nano*. 2021; **15**: 18653-18660. DOI: 10.1021/acsnano.1c09951
- [96] Nguyen T-T, Nguyen P-T, Pham M-N, Razafindralambo H, Hoang Q-K, Nguyen HT. Synbiotics: A new route of self-production and applications to human and animal health. *Probiotics and Antimicrobial Proteins*. 2022; **14**:1-14. DOI: 10.1007/s12602-022-09960-2

Wetting of Solid Iron by Molten FeO-Containing Slag

Volodymyr Shatokha and Yuri Korobeynikov

Abstract

The study aims to contribute the approaches for optimizing the parameters of the cohesive zone in blast furnace, as well as for enhancing the efficiency of novel alternative ironmaking processes. Wetting conditions between primary slag and iron sponge determine carbonization of the latter, thus affecting the position in the blast furnace of the region where slag and metal separate into independent liquid phases. Wetting of solid iron by molten FeO-containing slags representing the primary blast furnace slag was studied experimentally using a sessile drop method. Effects of the FeO content and slag basicity on the contact angle of slag on the iron substrate have been revealed. The opportunities of controlling the wetting conditions between primary slag and solid iron by optimizing the basicity of iron ore materials are discussed.

Keywords: ironmaking, blast furnace, cohesive zone, primary slag, iron, wettability

1. Introduction

In the blast furnace ironmaking, the properties of primary FeO-rich slag determine the process of carbon transfer to the freshly reduced solid iron, followed by separation of slag and metal into the independent liquid phases [1]. In some alternative ironmaking technologies, aimed to substitute blast furnace, an interaction between primary slag and solid iron also plays an essential role [2].

The schematic picture of the blast furnace is shown in **Figure 1**. In the lower part of the shaft of the blast furnace, reduction and heating processes result in forming of a cohesive zone where the layers of partially reduced softened iron ore material (sinter or pellet), impermeable for the ascending gas flow, are pressed between the gas-permeable layers of coke. The form and the thickness of the cohesive zone significantly affect all aspects of the blast furnace operation [4].

In the cohesive zone, chemical reactions take place mostly on the surface of softened material, notably on the lower part of the cohesive layer, where the primary slag, formed by interaction of iron monoxide (FeO) and the gangue compounds of iron ore material (predominantly, such as SiO₂, CaO, Al₂O₃ and MgO), contacts with the hot reducing gas and solid coke [1]. Due to pressure of the materials in the shaft of the blast furnace, FeO-rich primary slag squeezes from the iron sponge (formed due to reduction of iron oxides) to the surface of the cohesive layer.

Initially, high oxidizing potential of FeO-rich primary slag prevents carbonization of the iron sponge. However, while the materials descend to the area of blast furnace

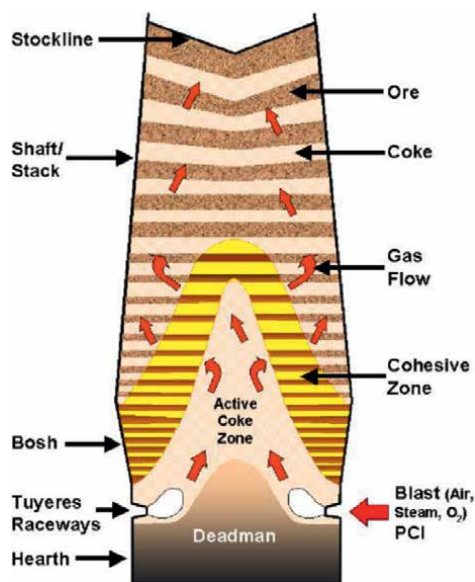


Figure 1.
Schematic picture of blast furnace [3].

with elevated temperature and stronger reducing potential of gas, FeO is gradually reduced from the primary slag and oxidizing potential of the latter decreases. At certain point, change of physicochemical parameters of interaction among the solid iron, the primary slag, the gas atmosphere and the coke, results in very rapid carbonization and melting of iron at the lower part of the cohesive zone. After separation into the independent liquid phases, slag and metal start to drip through the active coke zone (a term applied to the area between the cohesive zone and coke combustion raceways) down to the hearth (cylindrical part at the bottom of blast furnace) where they settle into the layer of hot metal (pig iron) topped with the layer of slag. Pig iron and slag are periodically tapped from the blast furnace [1, 2, 4, 5].

Studies on the quenched blast furnaces, performed in the 1970s in Japan [6], revealed that dripping of metal in the lower part of the shaft of blast furnace starts after its carbonization to 0.8–1.0% C. In the belly (the widest region of the blast furnace below the shaft), the carbon content of metal droplets grows to around 2.0%; further, in the bosh (conic region of blast furnace between the belly and the hearth), it reaches around 4.0% (tapped pig iron contains 3.8–4.5% C). Same pattern was observed for the silicon transfer to metallic phase: In the softened cohesive layer, metal contains less than 0.03% Si, then, just after the onset of carbonization, Si content grows to 0.2%, reaching 2% or more at the top of the bosh—even if a conversion pig iron (a semi-product used to further produce steel) with less than 0.6% Si is produced (for the sake of brevity, the phenomena of partial oxidation of metal components near the raceways are not discussed in this chapter).

Along with the silicon, sulfur is another compound whose concentration in pig iron shall be controlled in blast furnace operation. Samplings performed by Volovik [7] on an operating blast furnace revealed that, although sulfur absorption by the iron ore sinter is observed yet while it descends from the blast furnace top to the middle of the shaft, the freshly reduced solid iron, being enveloped by the primary slag, does not significantly absorb sulfur. After the liquid metal is formed, its sulfur content

drastically increases, reaching 0.3–0.4% S as a maximum (a value then decreases to final content of around 0.03% S in the tapped iron due to desulfurization of metal by slag in the hearth).

The industrial data referred above show that, in the blast furnace, freshly reduced solid iron, enveloped by the primary slag, remains virtually unaffected by chemical reactions within a certain period of time while the materials descend. However, at a certain point, the interplay of complex heating and reduction processes triggers very rapid change in composition and physical state of the metallic phase. Therefore, knowledge of the processes of interaction between the liquid FeO-rich slag and the solid iron is very important for the definition of iron ore materials' composition—either for blast furnace cohesive zone optimization or for more energy-efficient operation of alternative ironmaking processes. However, our analysis reveals very few studies where interaction phenomena between solid iron and liquid primary slag are investigated (most studies focus on wetting phenomena at the interface of slag and metallic melts).

Iguchi et al. [8] studied wettability of solid iron by the slags in various CO₂/CO atmospheres, revealing that the liquid slags with more than 30 mol% FeO content perfectly wet the solid iron surface. It was found that the contact angle increases with the increase in the basicity of slags under the constant oxygen pressure, while addition of Al₂O₃ and MgO has no significant effect.

Hino et al. [9] studied some parameters of interaction between the solid iron and liquid slags representing FeO·2CaO·SiO₂·Al₂O₃ (Gehlenite)-CaO·SiO₂ system with the ratio of Gehlenite/(CaO·SiO₂+ Gehlenite) = 0.3. Good wettability of iron by the studied slags was revealed, with the wetting angle decreasing in the range from 30° to 10° with the increased FeO content in the slag.

In both referred above studies, a sessile drop technique was applied with the temperature level fixed for all experiments—at 1350°C in [9] and at 1450°C in [8]. Noteworthy, these temperatures exceed the liquidus temperature for the slag studied systems and generally correspond to the conditions when the liquid slag phase is already separated from the iron phase—whether it is a lower boundary of cohesive zone in the blast furnace or, for example, an iron nugget, produced in the innovative ITmk3 ironmaking process [10]. In other words, by 1350°C a primary slag should be already long ago separated from the sponge iron, so the data available from the referred above studies [8, 9] are not very relevant to the conditions of sponge iron and primary slag interaction preceding their separation into the flowable phases.

Experimental approach with fixed temperatures, applied in [8, 9], allows for comparison of the wetting conditions in different slag systems. However, in reality, the temperature when primary slag and iron sponge separate into the independent liquid phases depends upon the reducing potential of gas, the reduction degree of the material and the gangue composition.

In our earlier study of the softening and melting properties of iron ore materials [11], it was shown that, in the viscous-plastic state under the load, an impermeable material is formed with the outer part coated by the slag relatively depleted in FeO due to the reduction, while its internal part contains iron sponge and FeO-rich slag. Under such conditions, the development of the physicochemical processes of iron oxides' reduction and carbon transfer to the metallic phase, resulting in slag and metal separation, is to a great extent determined by the slag properties. As far as FeO content in slag determines both fluidity and oxidizing potential of slag, it should play a predominant role in these processes. Kim et al. [12] also found that after the iron oxide in the slag is reduced, the separation of the final slag and the Fe–C melt takes place since the wettability between them decreases.

In the current research, we studied wetting of solid iron by the FeO-rich slag under the temperature conditions close to the temperature of complete melting for the given slag-conditions typical for the blast furnace cohesive zone, where interaction between the heterogeneous phases (liquid slag and solid sponge iron) takes place.

2. Experimental methods

Synthetic CaO-SiO₂-FeO slags were studied. FeO was produced using a mix of iron (purity of 99.99%, fineness <10 μm) and Fe₂O₃ (purity of 99.95%, fineness <5 μm) in a stoichiometric ratio corresponding to the reaction Fe₂O₃ + Fe = 3FeO. Quartz tube with the mix was closed with an iron wire sponge ball to prevent oxidation and purged with an Ar gas, then heated to 1050°C, held for 5 hours and quenched in water. “Pure for analysis” grade SiO₂ and CaO powders were used to prepare ternary CaO-SiO₂-FeO mixtures by weighing, mixing and grinding in a mortar.

Slag compositions (shown in **Table 1**) with relatively low liquidus temperature were chosen from different crystallization fields of a ternary CaO-SiO₂-FeO system (**Figure 2**) representing Wollastonite, Olivine and Wüstite. Noteworthy, in 3D phase diagrams of a quaternary slag systems (with MgO or Al₂O₃ as the fourth slag component), liquidus surfaces in these crystallization fields are plateau-like, in contrast to surrounding steep surfaces of Tridymite and Dicalcium Silicate crystallization fields. Composition of low-melting slags from Wollastonite, Olivine and Wüstite crystallization fields is most relevant to the primary slags, formed in partly reduced iron ore materials.

Wettability of solid iron was studied using a sessile drop method. Experimental setup is demonstrated in **Figure 3**. Slag cone (1) with 5 mm diameter and 5 mm height and average mass of approximately 200 mg was placed on the ARMCO® pure iron

#	Chemical composition, mass %				Contact angle, degrees	Temperature of measurement (complete melting temperature + 20°C), °C	Surface tension at temperature of measurement, calculated using method of Mills [13], mN/m
	SiO ₂ , %	CaO, %	CaO/SiO ₂	FeO, %			
1	50.0	22.0	0.44	28.0	60.0	1200	482
2	43.0	29.0	0.67	28.0	50.0	1200	509
3	38.0	34.0	0.89	28.0	44.0	1200	528
4	43.0	11.0	0.26	46.0	38.5	1150	512
5	38.0	16.0	0.42	46.0	19.0	1150	533
6	26.0	28.0	1.08	46.0	9.0	1150	580
7	38.0	0.0	0.00	62.0	5.5	1250	515
8	32.0	6.0	0.19	62.0	8.5	1150	555
9	25.0	13.0	0.52	62.0	22.2	1150	583

Table 1.
Composition and properties of the studied slags.

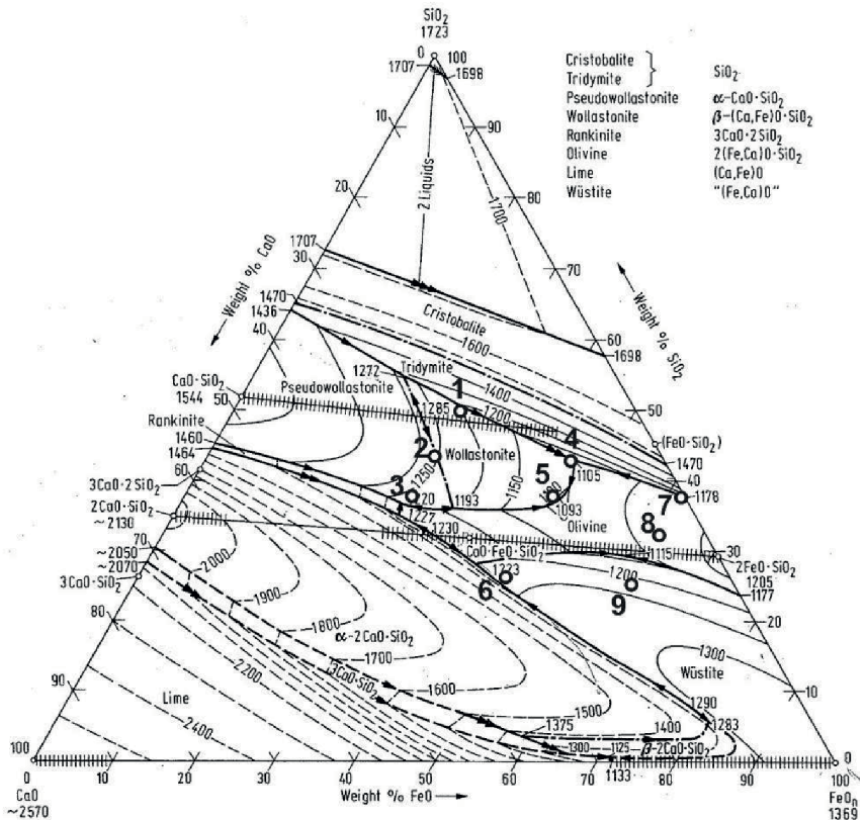


Figure 2. Ternary phase diagram for the CaO-SiO₂-FeO system [14]. Points denote slag compositions for the experiments listed in Table 1.

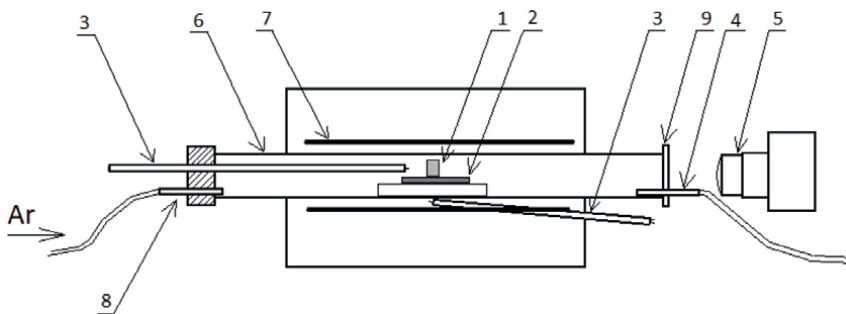


Figure 3. Experimental setup: 1—slag sample, 2—iron substrate, 3—thermocouples, 4—gas outlet, 5—photo camera, 6—quartz tube, 7—SiC heating elements, 8—gas inlet, and 9—quartz glass.

(99.98% Fe) substrate (2) established on the chamotte plate in the quartz glass tube (6) of the horizontal furnace with SiC heating elements (7). Two Pt-Pt/Rh type B thermocouples (9) were used: The first one, used for data recording, was placed near the studied sample and the second one—just under the quartz tube—to control isothermality of the reaction zone.

Technically pure Ar (99.99% Ar, Linde Gas) was constantly supplied to the reactor. Gas was exiting the reactor through the line (4) down to the water lock. Heating rate of 10° C per minute was applied. A digital photo camera was used to record the processes of melting and wetting. Obtained images were digitally processed using ImageJ [15] freeware. When the temperature of complete melting for a given slag was reached (i.e., when the entire sample formed a hemisphere), the temperature in the furnace was allowed to rise by another 20°C and stabilize within 5 minutes, and then, the contact angle was measured.

To ensure that the results are representative, three slag mix samples were studied. Two results with the smallest and the highest contact angle values were excluded, while the remaining result was retained for the analysis.

3. Results and discussion

The results of contact angle measurement are represented in **Table 1** and plotted against FeO content of slag in **Figure 4**. Data from the sources [8, 9] were approximated by the curves and also represented in **Figure 4** (for the data from [8] molar concentration was converted to mass concentration). As can be observed from **Figure 4**, slags with higher FeO content exhibit substantially lower contact angles with iron: Increase of FeO content from 28 to 62% is followed by fivefold drop in contact angle. The obtained results are generally consistent with the trends reported in literature [8, 9]. At the same time, it is interesting to mention that, as seen from **Figure 5**, surface tension of the slag slightly grows with the increasing of FeO content (data were calculated using the spreadsheet available from [13], representing modified partial molar method developed by Mills [16]). Such discrepancy might be explained by better wetting of the solid iron surface (due to chemical interaction of FeO and iron) at higher FeO content, which offsets the slight increase of surface tension.

Although, both in our experiments and in studies of the other authors, contact angle decreases with the increased FeO content in slag, our data show substantially higher values of contact angle for the comparable slag compositions (e.g., around 28% FeO). This difference can be explained by higher temperatures of measurement, applied in the referred studies [8, 9].

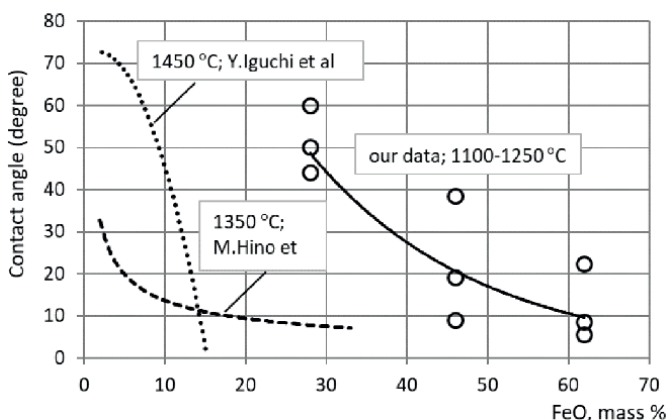


Figure 4. Measured contact angle versus FeO content in slag in comparison with data of Iguchi et al. [8] and Hino et al. [9].

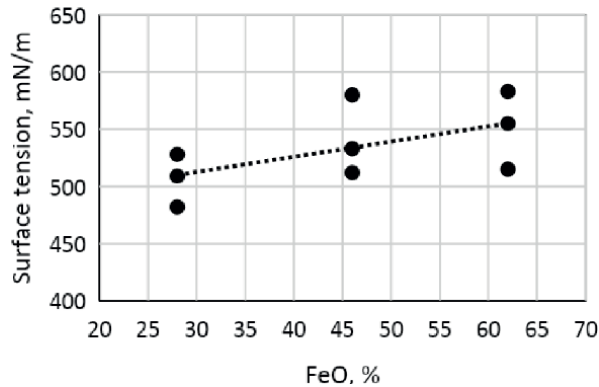


Figure 5. Surface tension calculated using method of Mills [13] versus FeO content in slag.

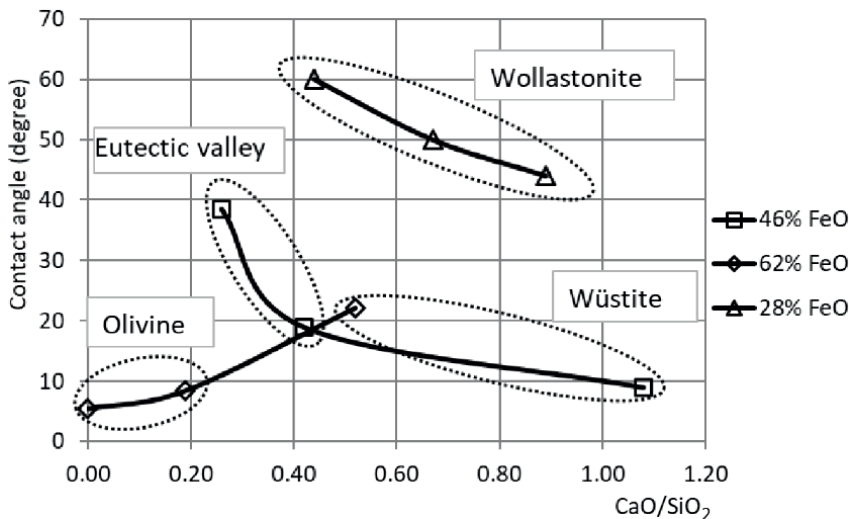


Figure 6. Contact angle versus slag basicity. Slags compositions presented in **Table 1** are grouped here according to crystallization fields as follows: 1, 2 and 3—wollastonite; 4 and 5—eutectic valley between olivine and wollastonite; 7 and 8—olivine; 6 and 9—Wüstite.

At the first sight, the experimental data for dependency of the contact angle upon the slag basicity are substantially scattered; however, as demonstrated in **Figure 6**, after the slags are grouped by the FeO content, it is possible to observe that, for the slags with FeO content of 28% and 46%, the increased basicity enhances wettability of the iron (contact angle decreases). On the contrary, for the slags with 62% FeO, contact angle increases with the increased basicity. Such ambivalent influence of CaO might be explained by the surface tension increase. A similar effect was previously reported by Kozakevitch [17] who studied surface tension of various slag mixes-addition of CaO to pure FeO is initially followed by surface tension's decrease; however, after CaO content in binary FeO-CaO melt reaches approximately 15%, surface tension starts increasing. Our slags with 62% FeO content may follow the behavior of the FeO-CaO binary system. Grouping of the slags by the crystallization fields in the ternary phase diagram (also demonstrated in **Figure 6**) shows that the

wetting conditions in the studied system can be efficiently controlled by tuning the slag composition and adjustment of the reduction degree of iron ore material (resulting in certain FeO content in slag).

In the study of Iguchi et al. [8], increase of the slag basicity was followed by increased contact angle; however, analysis of their data shows that the contact angles for the CaO-SiO₂-FeO slags with the basicity ratios (CaO/SiO₂) of 1.0 and 1.1 (both from the Wollastonite crystallization field) are higher when compared to the slag with the basicity of 0.5 from the Tridymite crystallization field. Therefore, it is possible to presume that the effect of slag basicity on the wettability of solid iron is rather complex and depends upon FeO content in the slag and other parameters of slag composition.

As discussed above in the introduction, wetting conditions between FeO-rich primary slag and the freshly reduced iron sponge determine iron carbonization and its intake of sulfur and silicon. Therefore, the obtained results might be used to develop a method for controlling the composition of metallic phase by tuning the composition of iron ore material and the regime of reduction. In our further studies, we aim to reveal the primary slag compositions (FeO content and basicity) favorable for limiting the transfer to the iron sponge of such elements as silicon, sulfur and probably even phosphorus (the latter under the blast furnace conditions is by 100% reduced to the hot metal), which might be applied for developing of a novel ironmaking method.

Table 2 outlines the expected aspects of such novel technology in comparison with blast furnace (major ironmaking technology within an integrated steelmaking route), Midrex® (major technology in relevant segment of integrated steelmaking) producing Direct Reduced Iron/Hot Briquetted Iron (DRI/HBI) and ITmk3® (one

Product parameters		Blast furnace [18]	DRI/HBI (Midrex®) [19]	ITmk3® [20]	Novel technology (expected)
Product composition	Fe metallic, %	≈94	83–89	97.2	≈99
	C, %	4.0–4.5	1.0–3.5	2.0–2.4	≈0.8
	Si, %	0.3–1.0		≈0.8	≈0.03
	S, %	0.03	0.001–0.03	0.07–0.12	≈0.03
	P, %	<0.2	0.005–0.09	0.01–0.025	≈0.01
	Gangue, %	Removed to slag	2.8–6.0	Removed to slag	Removed to slag
Product temperature, °C		≈1450 (determined by melting points of a product and of low-FeO slag)	≈950 (determined by thermodynamics of the reduction processes)	≈1350 (determined by melting point of a product)	1150–1250 (determined by melting point of Fe-rich slag)
State of product		Liquid (pig iron)	Solid pellets (DRI) or briquettes (HBI)	Liquid, then solidified into “nugget”	Solid (sponge)

Table 2. Parameters of product in ironmaking technologies.

of the alternative ironmaking technologies, commercialized in 2010, so far at a single plant). As shown in **Table 2**, we expect that thermodynamic conditions of iron ore reduction can be adjusted to prevent carbonization of metallic phase as well adsorption of silicon, sulfur and phosphorus. Certain losses of iron with FeO-containing slag are an unavoidable aspect of such approach to some extent, and this can be considered as a rebirth of an ancient bloomery process but on a current technology control level. However, we believe that novel technology should have competitive advantages to offset this drawback. Such advantages include

- superior product composition;
- lower (compared with blast furnace and ITmk3®) temperature level, resulting in lower energy requirement;
- absence of gangue material in the product should allow usage of medium grade iron ore in contrast to Midrex® where gangue material stays in the product, so its amount shall be kept low in order to minimize slag yield in the electric arc furnaces producing steel from DRI/HBI, which requires usage of scarce high-grade ores with >67% Fe [21].

Certainly, the precise aspects and, needless to say, technological layout of the proposed concept are yet to be considered in our further research where study of the wettability phenomena should play substantial role.

4. Conclusions

Interaction between the freshly reduced solid iron and the primary FeO-containing slag considerably determine carbonization of iron and subsequent separation of metal and slag into the independent liquid phases in the blast furnace operation conditions. Transfer of sulfur and silicon among the solid, gaseous and liquid phases is also affected by FeO content in slag which is determined by the wettability phenomena on the slag-metal interface. Wettability of solid iron by molten ternary CaO-SiO₂-FeO slags in an inert atmosphere under the temperature conditions close to the complete melting for the given slags was studied experimentally, and the main results are as follows:

1. The contact angle of a molten FeO-containing slags on the solid iron substrate decreases from 60.0° to 5.5° when the FeO content in slag increases from 28 to 62%. At the same time, surface tension of the slag slightly grows with the increasing of FeO content. Such discrepancy is explained by better wetting of the solid iron surface at higher FeO content due to chemical interaction of FeO and iron, which offsets the slight increase of surface tension.
2. Effect of the slag basicity on the contact angle depends upon the FeO content in slag: For the slag with 28% and 46% FeO, increased basicity ratio (CaO/SiO₂) of slag is followed by enhanced wetting of the solid iron. However, for the slags with 62% FeO, contact angle increases with the increased basicity. Such ambivalent effect of FeO in the ternary slag systems is in the agreement with previous studies of binary FeO·CaO melts.

3. A possibility of controlling the wetting conditions between the primary slag and the solid iron by tuning the composition of slag-forming compounds of iron ore material can be used to optimize the parameters of cohesive zone in blast furnace and to control the composition of hot metal or to design innovative energy-efficient ironmaking processes with limited transfer of sulfur and, possibly, phosphorus to the metallic phase.

Conflict of interest

The authors declare no conflict of interest.

Author details


Volodymyr Shatokha^{1*} and Yuri Korobeynikov²

1 Iron and Steel Institute of the National Academy of Science of Ukraine, Dnipro, Ukraine

2 Arizona State University, Tempe, AZ, United States

*Address all correspondence to: shatokha@gmail.com

IntechOpen

© 2023 The Author(s). Licensee IntechOpen. This chapter is distributed under the terms of the Creative Commons Attribution License (<http://creativecommons.org/licenses/by/3.0>), which permits unrestricted use, distribution, and reproduction in any medium, provided the original work is properly cited. 

References

- [1] Gupta S, French D, Sakurovs R, Grigore M, Sun H, Cham T, et al. Minerals and iron-making reactions in blast furnaces. *Progress in Energy and Combustion Science*. 2008;**34**:155-197. DOI: 10.1016/j.pecs.2007.04.001
- [2] Yan Z, Htet TT, Hage J, Meijer J, Li Z. HIsarna process simulation model: Using FactSage with macro facility. *Metallurgical and Materials Transactions B*. 2023;**54**:163:177. DOI: 10.1007/s11663-023-02732-5
- [3] Wright B, Zulli P, Bierbrauer F, Pankovic V. Assessment of refractory condition in a blast furnace hearth using computational fluid dynamics. In: *Proceedings of 3rd International Conference on CFD in the Minerals and Process Industries*; 10-12 December 2003. Melbourne, Australia: CSIRO; 2006. pp. 645-650
- [4] Ueda S, Kon T, Kurosawa H, Natsui S, Ariyama T, Nogami H. Influence of shape of cohesive zone on gas flow and permeability in the blast furnace analyzed by DEM-CFD model. *ISIJ International*. 2015;**55**:1232-1236. DOI: 10.2355/isijinternational.55.1232
- [5] Dong X, Yu A, Chew S, Zulli P. Modeling of blast furnace with layered cohesive zone. *Metallurgical and Materials Transactions B: Process Metallurgy and Materials Processing Science*. 2010;**41**:330-349. DOI: 10.1007/s11663-009-9327-y
- [6] Sasaki M, Ono K, Suzuki A, Okuno Y, Yoshizawa K, Nakamura T. Formation and melt-down of softening-melting zone in blast furnace. *Transactions of the Iron and Steel Institute of Japan*. 1977;**17**:391-400
- [7] Volovik GA. Sulfur partition between the burden and molten products in the blast furnace. *Stal*. 1961;**11**:967-971
- [8] Iguchi Y, Yamashita S, Innoue M. The wetting between solid iron and liquid slag. *Journal of the Japan Institute of Metals and Materials*. 1987;**51**:543-547
- [9] Hino M, Nagasaka T, Katsumata A, Higuchi KI, Yamaguchi K, Kon-No N. Simulation of primary-slag melting behavior in the cohesive zone of a blast furnace. Considering the effect of Al₂O₃, FeO and basicity in the sinter ore. *Metallurgical and Materials Transactions B: Process Metallurgy and Materials Processing Science*. 1999;**30B**:671-683
- [10] Harada T, Tsuge O, Kobayashi I, Tanaka H, Uemura H. The development of new iron making processes. *Kobelco Technology Review*. 2005;**26**:92-97
- [11] Shatokha V, Velychko O. Study of softening and melting behaviour of iron ore sinter and pellets. *High Temperature Materials and Processes*. 2012;**31**:215-220
- [12] Kim HS, Kim JG, Sasaki Y. The role of iron oxide bearing molten slag in iron melting process for the Direct contact. *ISIJ International*. 2011;**51**:166-168
- [13] Mills K. Slag modelling. *Slag Properties Spreadsheet* [Internet]. 2011. Available from: <https://www.pyrometallurgy.co.za/KenMills/Slags-KenMills.xls>
- [14] Verein Deutscher Eisenhüttenleute (VDEh). *Slag atlas*. 2nd ed. Düsseldorf: Verlag Stahleisen GmbH; 1995. p. 640
- [15] ImageJ. *Image Processing and Analysis in Java* [Internet]. 2022. Available from: <http://rsbweb.nih.gov/ij/>

- [16] Mills K. The estimation of slag properties. Short Course Presented as Part of South African Pyrometallurgy. 2011;**56**:2011. Available from: <https://www.pyrometallurgy.co.za/KenMills/KenMills.pdf>. [Accessed: February 26, 2023]
- [17] Kozakevitch P. Tension superficielle et viscosite des scories synthetiques. *Revista de Metalurgia*. 1949;**XLVI**:505-516
- [18] Peacey JG, Davenport WG. *The Blast Furnace Theory and Practice*. Oxford: Pergamon Press; 1979. p. 266
- [19] Atsushi M, Uemura H, Sakaguchi T. MIDREX ® Processes. *Kobelco Technology Review*. 2010;**29**:50-57
- [20] Kikuchi S, Ito S, Kobayashi I, Tsuge O, Tokuda K. ITmk3® process. *Kobelco Technology Review*. 2010;**29**:77-84
- [21] Direct From Midrex. FIRST QUARTER 2021. Charlotte: Midrex Technologies Inc.; 2021. p. 17. Available from: <https://www.midrex.com/wp-content/uploads/Midrex-DFM-1stQtr2021-Final.pdf>



Section 3

Consolidation of Powders



Chapter 6

Spark Plasma Sintering of NiCrSiBC Alloys

Escarlet Batista da Silva, Márcia Giardinieri Azevedo,

Lioudmila Aleksandrovna Matlakhova,

Bárbara Ferreira de Oliveira and Luciano José de Oliveira

Abstract

Nickel-based alloys of the NiCrSiBC system (colmonoy alloys) are normally deposited on stainless-steel substrates for coating applications, once they present high resistance to wear and corrosion at high temperatures. Typically, deposition occurs through welding processes, such as PTA (plasma transferred arc) or laser cladding. This study mainly aims to evaluate the effectiveness of the spark plasma sintering (SPS) process through the evaluation of the sintered body density, and structural and microstructural analysis of the Colmonoy-5. SPS sintering occurred at 900°C under 50 MPa for 15 minutes. Powder morphology was evaluated by confocal microscopy. The sintered samples were evaluated according to their density (Archimedes' method), phase composition, microstructure, and hardness (Vickers hardness). Results showed that the Colmonoy-5 alloy can be effectively produced through SPS sintering, reaching densification above 90%. Microstructural analysis showed that there was the formation of hardening phases, such as borides and chromium carbides. The same phases are found in colmonoy alloys deposited on the stainless-steel substrate.

Keywords: colmonoy, sintering, spark plasma sintering, microstructure, vickers hardness

1. Introduction

Nickel-based alloys are widely used in various areas of industry, such as chemical, petrochemical, nuclear reactors, warfare, aerospace, food processing devices, and steel production facilities, due to an association of high mechanical strength, good corrosion resistance, and weldability. The performance of these alloys is associated with the face-centered cubic structure of the matrix, which can be hardened by solid solution or by precipitation of intermetallic compounds [1].

There are several hard-facing alloys, the most common of which are Fe-based, Co-based, and Ni-based. Co-based hard alloys have many applications, but they become radioactive in nuclear environments, and this phenomenon has restricted the use of Co-based coatings for high-temperature applications. To minimize workers'

exposure to Co_{60} radiation during handling and maintenance operations, nickel-based hard-facing alloys from the NiCrSiBC family were developed. Colmonoy alloys (NiCrSiBC) have a wide variety of compositions and this consequently makes their use very abundant. It can be said that currently alloys are used preferentially for coating materials [2, 3].

It can be said that Ni-based hard-facing alloys, which still have carbides and borides in their structure formed from alloying elements, are popularly used as coating materials. Among the hard Ni-based alloys, colmonoy can be highlighted, which is widely used, and may also have different NiCrSiBC compositions depending on the alloying elements [4, 5].

Alloys from the NiCrSiBC family, such as colmonoy, have as their main characteristic their high resistance to wear and corrosion at high temperatures. These alloys were basically developed for deposition using some welding processes. Due to their excellent characteristics and lower cost compared to Co superalloys, Ni-based alloys have been deposited by various welding processes, such as plasma transferred arc (PTA), tungsten inert gas (TIG) and laser cladding [6–8].

The strength of colmonoy alloys (NiCrSiBC) can be increased by the formation of precipitates such as borides and carbides. Some studies of the alloys of the NiCrSiBC family deposited by laser cladding on a steel substrate showed the presence predominantly of the intermediate phases formed, in the form of carbides, borides, and silicides: CrB, Cr₅B₃, Ni₄B₃, Cr₅B₃, Cr₇C₃, and Ni₃Si [9, 10].

Although welding deposition processes are widely used and applied, the substrate, which is usually stainless steel, has a high iron content, which can change the composition of the coating, causing the phenomenon known as dilution. The alloys of the NiCrSiBC family are very sensitive to the presence of the iron element, which results in a change in their microstructure and consequently in some mechanical properties, as observed in the works [9, 11, 12].

It should be noted that pulsed plasma sintering (SPS) can also be a processing route for nickel-based alloys, although still little explored, as mentioned in the work by [13]. In addition, there are no reports that clearly show the study of the influence of Fe on SPS-processed Ni-based alloys.

Spark plasma sintering is considered a powder metallurgy technique that features fast manufacturing routes at relatively low temperatures, involving simultaneous applications of pressure and temperature, resulting in engineering components with relatively high density and good mechanical properties, compared to others. Conventional sintering methods [14].

SPS technique stands out for its ease of operation and precision in sintering energy control, high sintering speeds, safety, and reliability [15].

Spark plasma sintering involves the simultaneous application of load as well as heat on the materials to be sintered. SPS is a new method meant for consolidation of nano-structured materials with hindered grain growth, efficient shrinkage in less time, and cleaner grain boundaries for effective interface formation. This technique utilizes high-temperature spark plasma generated by discharging exactly at the gaps of powder particles with an on-off electrical current. At the initial stage of the SPS process, the generated spark plasma induces neck formation and thermal diffusion process on the particles to be sintered. An electric field formed by DC current can also facilitate thermal diffusion process. Therefore, the SPS process involves the densification of poorly sinterable materials at a very short interval of time and at low temperature when compared with the conventional sintering process [16].

Colmonoy alloy properties are strongly related to the microstructure formed after alloy processing. Thus, in this work, greater attention was given to the correlation of the microstructural aspect and some important properties, such as density and hardness of colmonoy alloy, sintered by SPS, maintaining the parameters determined in the work of [5].

Currently, it can be said that there are few published works that report microstructural aspects of SPS-sintered NiCrSiBC alloys. Thus, the current literature basically brings studies of these alloys deposited on steel substrates, which often analyze the effect of Fe dilution on the microstructure of the alloy [17]. In this way, this work intends to show that it is possible to sinter the colmonoy alloy by the spark plasma sintering (SPS) process, and consequently contribute to future studies on the possibility of sintering the colmonoy alloy on a stainless-steel substrate.

2. Methodology

Commercial powders of Colmonoy-5 alloy (Ni-14Cr-3Si-2.5B-0.6C-4,2Fe) produced by the manufacturer WallColmonoy Corporation were used to process the samples. Powders were produced by atomization technique. The atomization process consists of casting system, which performs the fusion raw material for one induction oven under controlled environment where alloys are smelted, refined, and degassed. Refined melt metal is poured through a system crucible in a gas nozzle, where the stream of the melted metal beam is disintegrated from the kinetic energy of high-pressure inert gas flow (Argon). **Figure 1** shows a schematic of the gas atomization technique [18].

The average particle size of the powders was provided by the manufacturer. To analyze the morphology of the powders, images were made via confocal microscopy.

Colmonoy-5 alloys were sintered by spark plasma sintering (SPS) technique, maintaining technological parameters predetermined in the work [5]. SPS sintering occurred at 900°C under 50 MPa for 15 minutes.

The sintered material was subsequently characterized under structural aspects, microstructural, relative density, and Vickers hardness. **Figure 2** shows the general and succinct roadmap of the main stages of the development of the work.

In order to evaluate sintering effectiveness, the densification alloy after sintering was measured. For that, the density (apparent specific gravity) was determined using the Archimedes method, using four samples. The calculation of the apparent specific mass is based on the value of the dry mass of the sintered (MS), the mass of the same immersed in water (MI), and the saturated mass (MA) that is obtained after the sample is boiled for a period of 20 minutes. For this, the density of water is also considered, as shown in eq. 1. The percentage of densification (relative density) was calculated from the values of the experimental density of the sintered material and the theoretical density (eq. 2), that is, it is the ratio between the ASG of the sample and theoretical alloy density of 8,14 g/cm³ [4].

$$ASG = \frac{MS}{(MA - MI)} \times \rho_{H_2O} \quad (1)$$

$$Density(\%) = \frac{ASG}{Density\ Theoretical} \times 100 \quad (2)$$

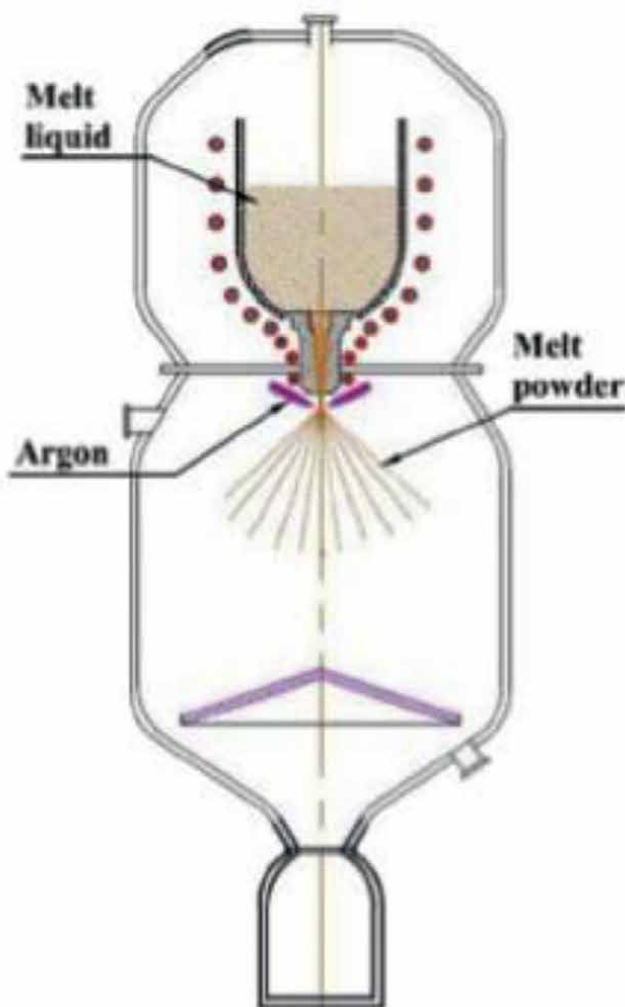


Figure 1.
Gas atomization process [18].

The microstructural aspect of the sintered body after SPS was performed from SEM. Before SEM analysis, the samples were metallographically prepared, first sanded (100 to 1200 mesh), and later polished and subjected to chemical attack. Phase identification was performed through X-ray diffraction analysis, using a Bruker D2 phaser diffractometer. The diffractometer is equipped with a Cu-K α radiation tube, where the samples were scanned in the 2θ range, with an interval between 20° and 90° , under a step of 0.05° for 3 seconds. The characteristic peaks in the diffractions obtained were analyzed, and the results were compared with the ICDD (International Center Diffraction Data) database, to help identify the phases present.

Vickers hardness tests were carried out with the aid of a digital micro hardness tester DHT, HVS – 1000, performing five indentations [19, 20] in each sample and applying a load of 1 kgf in the tests for a time of 10 seconds.

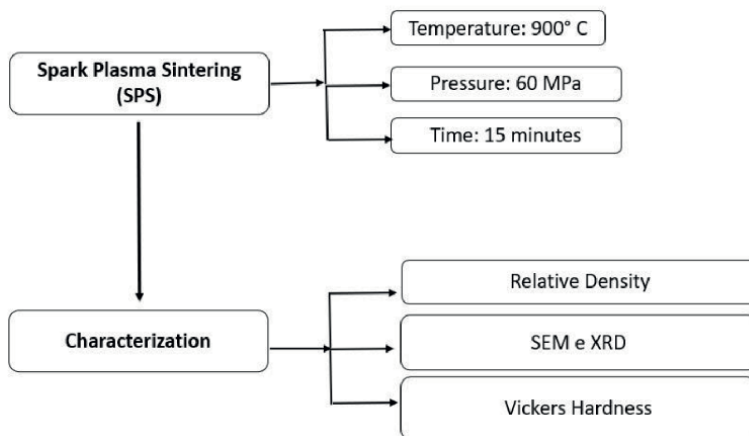


Figure 2.
Processing route, characterization steps, and testing of Colmonoy-5 alloy.

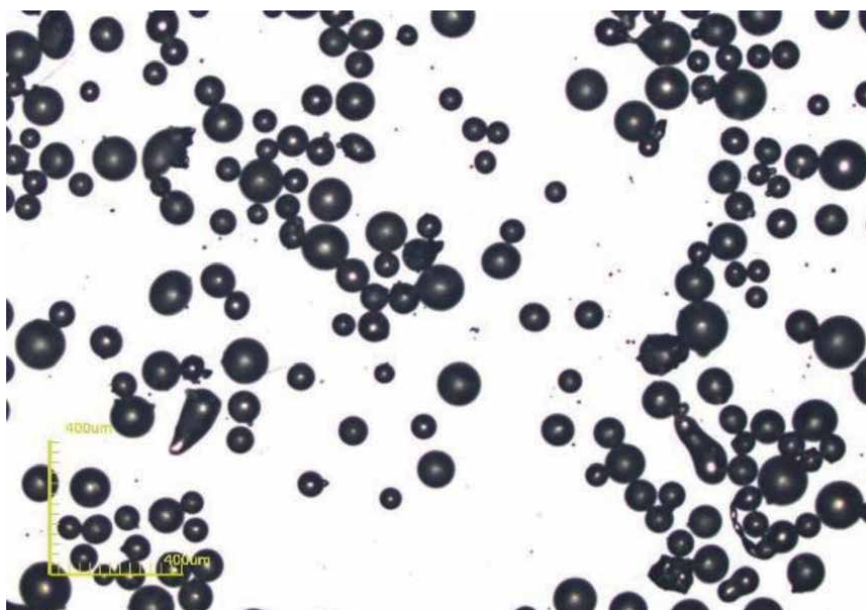


Figure 3.
Colmonoy-5 alloy powders with spherical morphology.

3. Results and discussion

Table 1 shows the mean values of the apparent specific gravity (ASG) measurements of the four samples, and their respective standard deviations. ASG values verified were around 7.5 g/cm^3 on average. Through eq. 2, it was obtained about 92% densification (ASG/theoretical density), indicating that SPS sintering was effective. Density may increase as a function of sintering temperature. Thus, it is believed that we can achieve densification greater than 92% at temperatures higher than those used in this study [19, 20].

Pressão (MPa)	MEA (g/cm ³)	DP
60	7.47	± 0.168

Table 1.
Apparent specific gravity (ASG) is calculated by the Archimedes method.

Figure 3 shows it is possible to observe regular shaped powder particles and predominantly spherical morphology, which is a common characteristic of powders produced by atomization and may also have contributed to the good densification achieved. Evaluation of the average size of the powders revealed an average size of 74 to 149 μm.

Figure 4 shows XRD Colmonoy-5 alloys sintered by SPS. In all sintered samples, in addition to nickel, the presence of several important phases, such as borides (CrB, Ni₂B, Cr₂B, Ni₃B, and Cr₅B₃), as well as Cr₇C₃ chromium carbide. The phases verified in the XRD analysis of the bodies sintered by SPS are the same obtained in the diffractograms of the initial powders, which is in perfect agreement with the works [11, 21, 22].

Figure 5 shows fine precipitated phases and homogeneous distribution. Chromium borides appear in the form of very fine dark modules and small dark blocks. Studies by Ref. [23] on NiCrSiBC alloys indicated in a transmission electron microscope (TEM) analysis that Cr₂B chromium boride can be presented in the form of small dark blocks. There is also an intense formation of laths and small blocks in half-ton (lighter phase) well distributed in the matrix phase, which is probably chromium carbide.

It can be seen in **Figure 6(a)**, again the presence of chromium borides (dark phase) in the form of fine needles and some small blocks. Note also a lighter phase in the form of a butterfly or wing (see circles), which is a precipitated phase rich in chromium. The EDS mapping in these regions, as shown in **Figure 6(b)**, shows a high concentration of chromium in such phases, which actually indicates that it is a chromium-rich precipitate, specifically a Cr₅B₃ chromium boride [10]. It should be

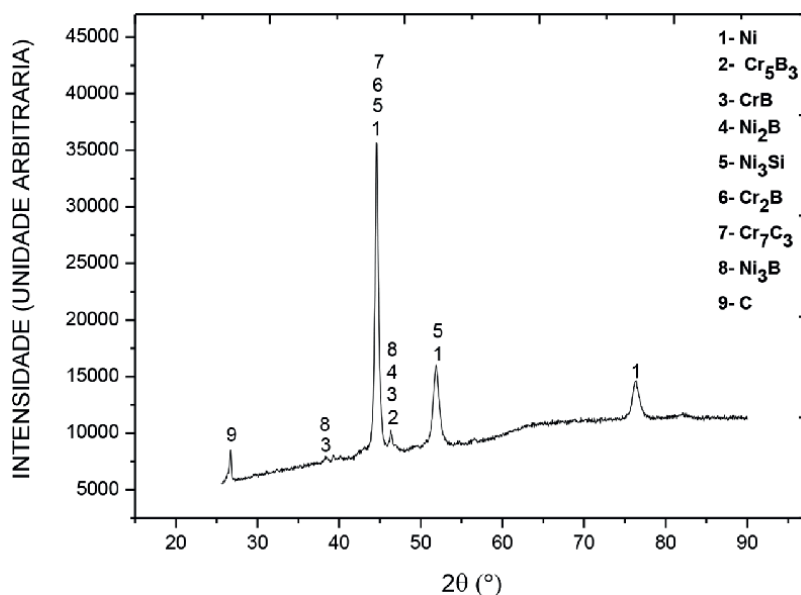


Figure 4.
XRD diffractograms of Colmonoy-5 alloys after SPS.

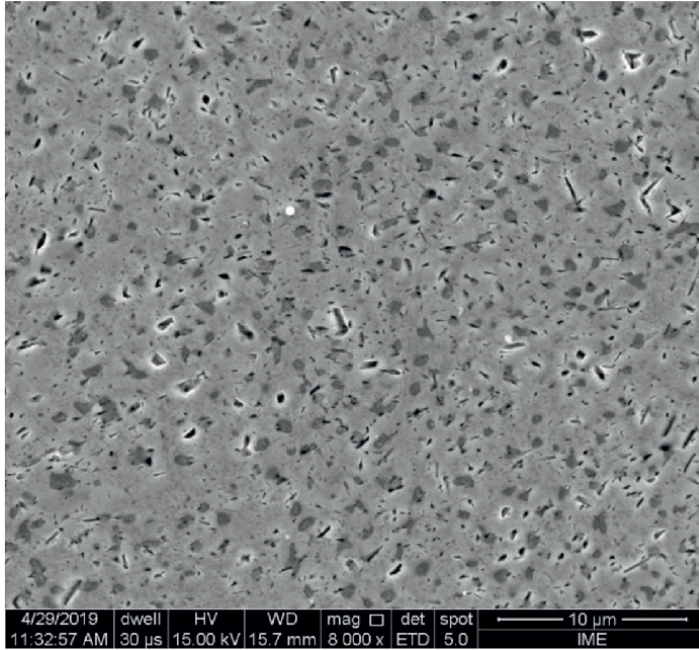


Figure 5.
Microstructure of Colmonoy-5 alloys sintered by SPS.

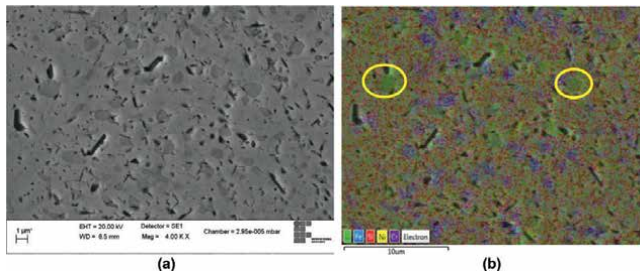


Figure 6.
(a) Microstructure and mapping region e (b) EDS image.

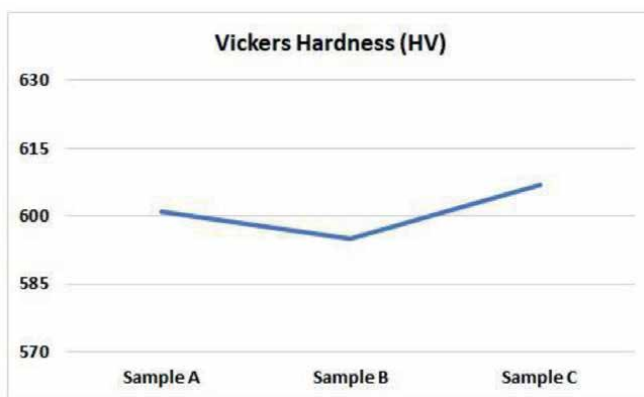


Figure 7.
Average hardness (HV) of the Colmonoy-5 alloy for 3 samples.

noted that it was not possible to capture boron element (B) by the EDS, due to the equipment limitation.

The average value obtained for the Vickers hardness of the Colmonoy-5 alloy sintered by SPS was 601 ± 6 HV, as shown in **Figure 7**. This result is in agreement with studies by Refs. [11, 12, 24].

4. Conclusion

The structural and microstructural analysis showed that phases formed after the SPS are the same as those found for the colmonoy alloy deposited.

The average hardness measured is within the range and in agreement with the literature in studies on colmonoy alloys.

It can be said that the SPS sintering of the Colmonoy-5 alloy was effective since it obtained densification above 90%. Thus, the SPS process can be a processing route for the colmonoy alloy.

Acknowledgements

The authors are grateful for the support of the Brazilian institutions FAPERJ, IME, and IFES campus Vitória/ES throughout the development of this study.

Author details

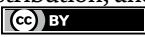
Escarlet Batista da Silva^{1*}, Márcia Giardinieri Azevedo¹,
Lioudmila Aleksandrovna Matlakhova¹, Bárbara Ferreira de Oliveira¹
and Luciano José de Oliveira²

1 Advanced Materials Laboratory, CCT/UENF – State University of Northern Rio de Janeiro, Campos, RJ, Brazil

2 Institute of Society Science, MDM/UFF – Fluminense Federal University, Macaé, RJ, Brazil

*Address all correspondence to: escarletbatistadsilva@gmail.com

IntechOpen

© 2022 The Author(s). Licensee IntechOpen. This chapter is distributed under the terms of the Creative Commons Attribution License (<http://creativecommons.org/licenses/by/3.0>), which permits unrestricted use, distribution, and reproduction in any medium, provided the original work is properly cited. 

References

- [1] Sandes SS et al. Avaliação de Revestimentos de Liga de Níquel 625 Depositados pelo Processo Eletroescória. *Soldagem & Inspeção*. 2016;**1**(4):417-427
- [2] Das CR et al. Effects of dilution on microstructure and wear behaviour of NiCr hardface deposits. *Materials Science and Technology*. 2007;**23**(9):771-779
- [3] Kumar H et al. Friction and wear behaviour of Ni-Cr-B hardface coating on 316LN stainless steel in liquid sodium at elevated temperature. *Journal of Nuclear Materials*. 2017;**495**:431-437
- [4] Handbook ASM. *ASM Specialty Handbook: Nickel, Cobalt, and their Alloys*. In: Davis JR, editor. *EUA*. Davis & Associates; 2000
- [5] Silva B. Caracterização da liga Colmonoy-5 sinterizada por plasma pulsado (SPS)”, *Dissertação (Mestrado em Engenharia e Ciência dos Materiais)*. Campos dos Goytacazes – RJ: Universidade Estadual do Norte Fluminense – UENF; 2019
- [6] Luo JL et al. Effect of NiCrBSi content on microstructural evolution, cracking susceptibility and wear behaviors of laser cladding WC/Ni-NiCrBSi composite coatings. *Journal of Alloys and Compounds*. 2015;**626**:102-111
- [7] Benea L et al. Fretting and wear behaviors of Ni/nano-WC composite coatings in dry and wet conditions. *Materials and Design*. 2015;**65**:550-558
- [8] Araújo PHD. Caracterização de Materiais Dissimilares com Revestimentos NiCrSiBC em Diferentes Substratos *Dissertação (Mestrado em Engenharia e Ciência dos Materiais)*. Campos dos Goytacazes – RJ: Universidade Estadual do Norte Fluminense – UENF; 2016. p. 27
- [9] Silva LJ, D’Oliveira ASC. Liga NiCrSiBC: Microestrutura e Dureza de Revestimentos Processados a Arco e a Laser. *Soldagem & Inspeção*. 2015;**20**(1):39-47
- [10] Hemmati I et al. Effects of the alloy composition on phase constitution and properties of laser deposited Ni-Cr-B-Si coatings. *Physics Procedia*. 2013;**41**:302-311
- [11] Hemmati et al. Dilution effects in laser cladding of Ni-Cr-B-Si-C hardfacing alloys. *Materials Letters*. 2012;**84**:69-72
- [12] Silva LJ, D’Oliveira ASCM. NiCrSiBC coatings: Effect of dilution on microstructure and high temperature tribological behavior. *Wear*. 2016;**350-351**:130-140
- [13] Yamanoglu R et al. Characterization of nickel alloy powders processed by spark plasma sintering. *Powder Metallurgy*. 2014;**57**(5):380-386
- [14] Asl MS et al. Effects of sintering temperature on microstructure and mechanical properties of spark plasma sintered titanium. *Materials Chemistry and Physics*. 2018;**203**:266-273
- [15] Borkar T, Banerjee R. Influence of spark plasma sintering (SPS) processing parameters on microstructure and mechanical properties of nickel. *Materials Science & Engineering A*. 2014;**618**:176-181
- [16] Shashanka R et al. Effect of Y₂O₃ nanoparticles on corrosion study of spark plasma sintered duplex and ferritic stainless steel samples by linear sweep Voltammetric method.

Archives of Metallurgy and Materials.
2018;**63**(2):749-763

[17] Balaguru S, e Gupta, M. Hardfacing studies of No alloys: A critical review. Journal of Materials Research and Technology. 2021;**10**:1210-1242

[18] Chen G et al. A comparative study of Ti-6Al-4V powders for aditive manufacturing by gas atomization, plasma rotating electrode process and plasma atomization. Powder Technology. 2018;**333**:38-46

[19] Shashanka R, Chaira D. Effect of sintering temperature and atmosphere on nonlubricated sliding Wear of Nano-Yttria-dispersed and Yttria-free duplex and ferritic stainless steel. Tribology Transactions. 2017;**60**(2):324-336

[20] Shashanka R, Chaira D. Development of nano-structured duplex and ferritic stainless steels by pulverisette planetary milling followed by pressureless sintering. Materials Characterization. 2015;**99**:220-229

[21] Naik HV, e Kalyankar, V.D. Development of NiCrSiBC weld hardfacing approach for P91 steels used in steam turbine componentes. Soldagem & Inspeção. 2021;**26**:1-15

[22] Silva LJ et al. Effect of microstructure on wear performance of NiCrSiBC coatings. Wear. 2019;**428-429**:387-394

[23] Kesavan D, Kamaraj M. The microstructure and high temperature wear performance of a nickel base hardfaced coating. Surface & Coatings Technology. 2010;**204**:4034-4043

[24] Chen X et al. Microstructural evolution of NiCrBSi coatings fabricated by stationary local induction cladding. Journal of Materials Engineering and Performance. 2018;**27**(5):2446-2456

Experimentation and Optimization of Multilayered Aluminum-Based Functionally Graded Materials

Pattapagalu Naga Sudhakar Srinivas, Pittam Srinivas Rao, Kolari Deepak and Nallamilli Srinivas Reddy

Abstract

According to current industrial and societal demands, product manufacturing is now highly competitive. The current research is primarily focused on the creation of functionally graded materials that are essential for automotive cylinders and their internal components. Since aluminum plays a significant role in automobile components, layerwise deposition of the matrix and reinforcements is used. Aluminum alloy (Al 356) was investigated in weight proportions of 100, 95, and 90%, while the reinforcement varied from 0 to 7.5%. The particulate reinforcements were chosen to be silicon carbide (SiC) and nickel (Ni). Zinc stearate is used as lubricating agent to enhance the free-flow compaction process and to avoid the wastage in synthesis. The compressed specimens were examined for various mechanical and microstructural characterization. An ultimate compressive strength of 328 MPa and 68 BHN was achieved at 85% Al, 5% SiC, and 7.5% Ni, as per research criterion. Scanning electron microscopy (SEM), energy dispersive X-ray analysis (EDAX), and X-ray diffraction analysis (XRD) images of the inclusions and matrix are compatible and compact due to the excellent bonding. The process variables were adjusted using Taguchi optimization, which shows that the sintering duration and compaction pressure are crucial for the validation of manufacturing and characterization.

Keywords: gradation materials, powders, compaction, ejection, properties, SEM, EDAX, molecular structure

1. Introduction

Functionally graded materials (FGMs) are a distinct and varied class of materials with a wide range of uses, from home to commercial. The introduction of these materials in the field of mechanical and materials engineering aims to provide a novel and resilient material that satisfies mechanical, microstructural, and tribological requirements. In order to provide solutions with this kind of materials, these types of materials are designed and developed. Materials with continuous material properties in all

directions and some modifications to their microstructure are unable to withstand all temperature variations and gradients within a short period of the material thickness.

Even if they are successful, researchers with their creativity and knowledge are working hard to produce these materials to a greater level, but the production and characterization processes have flaws and limitations. This is frequently accomplished by progressively shifting the volume fraction of two components with various thermomechanical properties in a certain direction, resulting in a compound with various volume ratios [1]. For spacecraft with one side exposed to extremely high temperatures and the other exposed to extremely low temperatures, FGMs are the best choice because they distribute material functions throughout the material body for best heat resistance and mechanical qualities. FGM is used in the development of most industrial sectors' products today, including those in the automotive, information technology, computer science, and other related fields [2].

1.1 Development and progression of FGM

Most of the research investigations are progressed with the development of functionally graded aluminum composites by the aid of centrifugal casting analyzed the influence of mechanical and wear properties of pure aluminum, boron carbide, silicon carbide, alumina, and titanium boride. Radhika et al. [3] in her research experimentations with FGM stated that the outer peripheries of the FGM exhibit higher hardness except in AlB_4C and the outer zone exhibits tensile strength at its maximum. Chandrappa et al. [4] have synthesized with the aid of conventional powder metallurgy method at $436^\circ C$ sintering temperature and depicted that high volume fraction of SiC caused clustering of carbide phase at grain boundaries, which restricts interparticle contacts and further becomes a wall for densification in their study titled, "manufacturing and characterization of Al-SiC FGM developed through powder metallurgy." For preparation of Al/Si functionally graded materials using ultrasonic separation method, Zhang Zhong tao et al. [5, 6] have successfully synthesized the standardized Al-SiC FGM and also depicted that increasing the composition of SiC makes the FGM harder and at a limiting value, it becomes brittle and crack formation is observed, with the highest compressive strength obtained at 7.5% of SiC insertion.

A research article designated as synthesis of hydroxyapatite in combination with titanium alloy to prepare FGM composites by powder methodology ultimately used as implant materials depicted that microhardness is increased by 28% when compared with steel alloys. Amir Arifin et al. [7] successfully processed HA/Ti FGMs and depicted that increasing the titanium percentage increases the hardness and compaction capability of the synthesized FGM. He has also illustrated the elements' flawless cohesion and excellent microstructural characteristics. Madhusudan et al. [8] successfully formulated a procedure to determine the optimal thickness of the mold material in the production of FGM in centrifugal casting, as well as inferred various parameters affecting FGM production, starting with preheating, molten metal heating, and solidification rate.

2. Selection of materials

The materials used in the experimentation process were chosen based on functional requirements, as we intend to develop an electromechanical aeronautical application product, and thus, aluminum is the best product, with silicon carbide for high

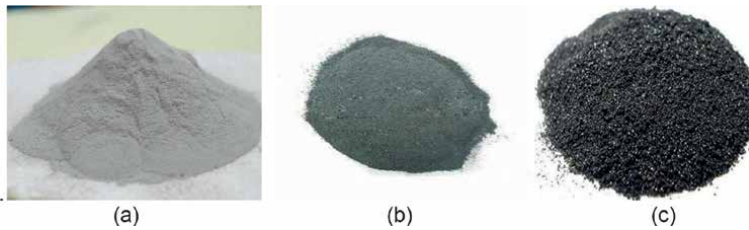


Figure 1.
 Powdered form of (a) Al 356 (98% purity, 100 mesh size), (b) SiC (150 mesh size), and (c) Nickel (180 mesh size).

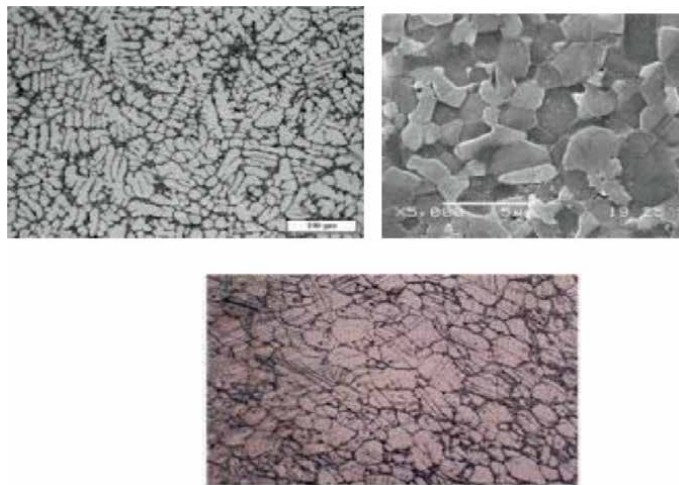


Figure 2.
 SEM morphological images of Al 356, SiC, and Nickel.

Layer	Composition (%)	Weight (g)	Matrix	Reinforcement
1	100	26	Pure Al	NIL
2	90/10	22.4/2.6	Pure Al	SiC
3	80/10/10	20.8/2.6/2.6	Pure Al	SiC, Ni

Table 1.
 Depiction of layerwise composition of the matrix and the reinforcements in FGM.

toughness and hardness and nickel for good wear and corrosive resistance, and all materials were obtained from Raghavendra spectro metals LTD, Hyderabad, and are in powdered form as shown in **Figure 1**.

2.1 Blending of powders by weight ratio

The matrix and the reinforcements are successfully blended by considering weight percentages with the aid of digital weighing balance with least count of 1 milligram, and the uniform mixing of matrix and the reinforcements are successfully blended with ball milling machine with 1000 kg capacity as per ASTM D7152 standardization, which is depicted in **Figure 2** and **Table 1**.

3. Compaction process

After uniform blending of the powders that consist of matrix and reinforcements, the next most crucial process is the compaction where the blending mixture as per rule of mixtures is needed to attain the solid shape, which means we need to convert from powder to solid form that is a complicated and cumbersome process. This is achieved by powder compaction machine having capacity of 1Ton supplied from Instron equipments limited, which is suitable for all kinds of metallic power metallurgical process. The compaction and ejection process is controlled automatically, and the application of the loading can be visualized on monitor and display of crucial parameters with a graphical interface. The compaction load is maintained at 480KN, and the ejection at 80KN that is treated as nominal and safe standards and any variations of loading conditions and the material failure are indicated with the aid of a buzzer or by alarming system. Cylindrical specimens are generated, which have 40 mm diameter and 10 mm thickness depicted in **Figures 3** and **4**. After the necessary and sufficient conditions, the green compacted specimen is manufactured and is digitally weighed and checked its manufacturing defects visually and also by the microscope according to specified standards of ASTM B925-15. The compacted specimens can be viewed in **Figure 5**.

4. Sintering process

The compacted specimens are sintered at a temperature of 472 degrees centigrade in muffle furnace depicted in **Figure 6**. The sintering process is mainly developed to



Figure 3.
Microbalance weighing of green-compacted FGM specimens.

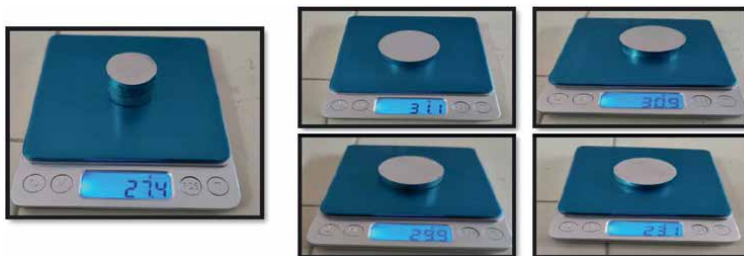


Figure 4.
Sectional views (front and side) of the dry-compacted specimen.



Figure 5.
Compaction testing machine for the preparation of green compact FGM.

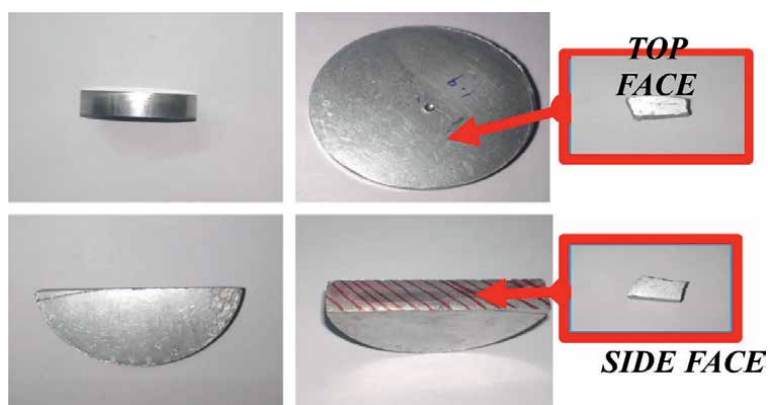


Figure 6.
Sintering process of green-compacted FGM in high tubular furnace.

increase the hardness of the green compacts as they are in very low strength and cannot be used for the material testing and also to enhance the hardness of the component. It is taken to be 70% of the melting temperature of the pure aluminum melting point (673 degree centigrade) [9].

5. Material characterization

5.1 Density

Table 2 defines the comparison between the experimental measured density and the density achieved through theoretical calculations of the aluminum alloy and the manufactured FGM composites. By clearly visualizing the spectral images, we can clearly depict that the composites are prepared successfully with low porosity and microstructural imperfections. However, during the calculation we depicted that the measured values have attained lower values than those of the theoretical values. The depiction of low pores in the composite, low interstitial voids, agglomerations, and discontinuities, which are due to the impingement of reinforcements in proper weight percentages, is the main source during the compaction process. The theoretical and measured densities have been depicted in **Figure 7**

Material	Theoretical density(g/cc)	Measured density(g/cc)
Pure Al 356	2.78	2.68
Al 356+10%SiC	2.84	2.79
Al 356+10%SiC+10%Ni	2.92	2.84
Al 356+5%SiC	2.85	2.75
Al 356+5%SiC+5%Ni	2.87	2.82

Table 2.
Theoretical and measured densities of the alloy and FGM composites.

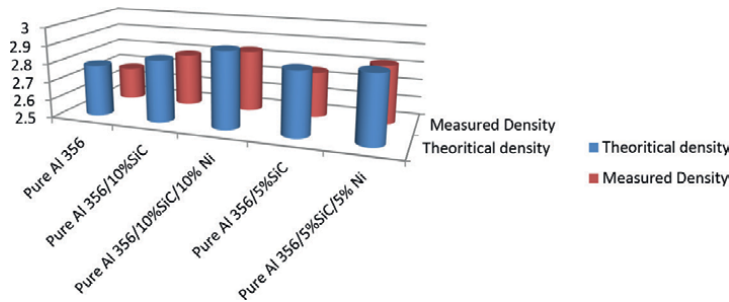


Figure 7.
Theoretical density vs. practical density.

5.2 Evaluation of material hardness

The FGM shows a macro-hardness of 34.65% greater than the pure aluminum base metal when conducted in Brinell hardness tester. The process is done as per ASTM E384 since these results are to be validated with a standard process and then only the results will serve the purpose.

The compressive strength is been characterized by using UTM with ASTM E-38 standardized specifications. Upon application of force on both sides, the FGM composites are failed at point and when calculating the stress-strain diagrams, the compressive strength is depicted to be 258.5 MPa, which has enhanced from 215.8 MPa for the base metal Al356 compression strength, which is depicted in **Figures 7–9** for Al356/10%SiC/10%Ni composition attained the maximum value.

5.3 Vicker’s microhardness test

The microhardness of FGM is found to be 2.85 times the base metal when conducted on Vicker’s hardness. Where VHN is known as Vicker’s hardness number, the hardness value for each of the layer is designated in **Tables 3 and 4** with VHN units.

5.4 Scanning electron microscopy (SEM)

The scanning electron microscopy (SEM) characterization shows the development of grains and grain limits of grid and building up materials, and there are no arrangement of voids, breaks, and surface flaws [10]. This process is done as per ASTM E986, which clearly shows how the bonding of constituents and blunt interfaces with good

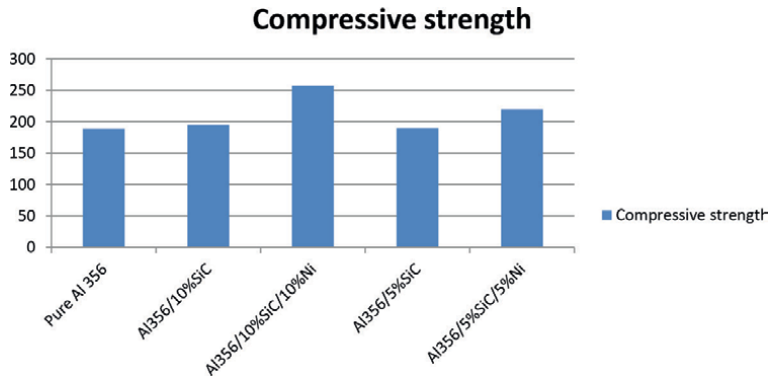


Figure 8.
 Compression strength vs. composition.

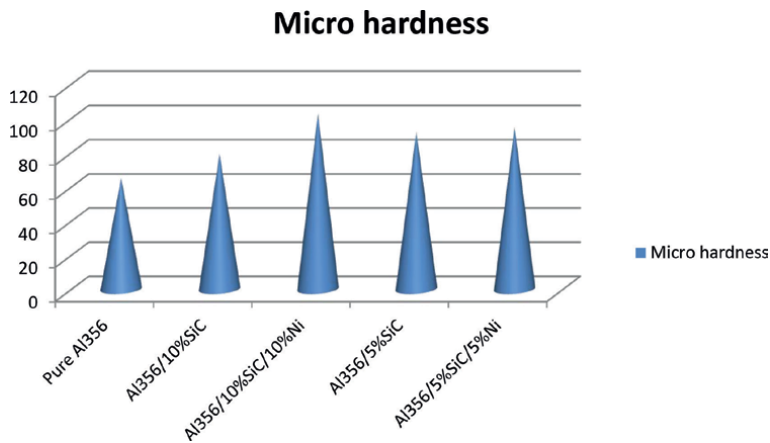


Figure 9.
 Microhardness vs. composition.

Material	Compressive strength(MPa)
Pure Al 356	189
Al 356+10%SiC	195
Al 356+10%SiC+10%Ni	258
Al 356+5%SiC	190
Al 356+5%SiC+5%Ni	220

Table 3.
 Depiction of compressive strength of FGM composites with composition.

amount of contact between them. The observation of bonding is not only done at the bonding region of the matrix and the reinforcement's level but also we have observed at the intermolecular level, that is, at the middle region where the matrix and the reinforcements bond together with the equal weight percentages (50%) as depicted in **Figures 10–12**.

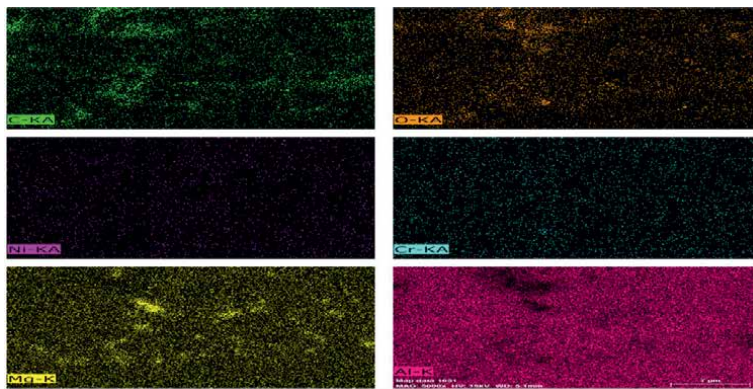


Figure 12.
 SEM micrographs, quantitative results, and mapping of Al6061/0.6SiC_{np}/0.4Cr_{np}.

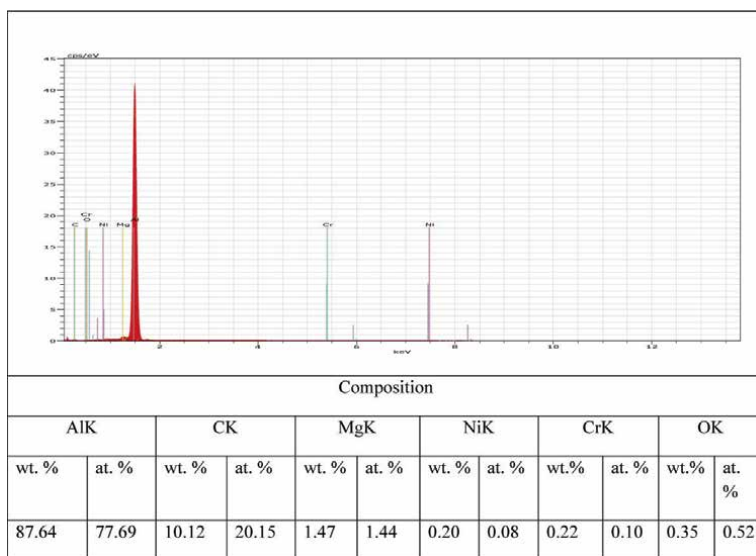


Figure 13.
 EDAX Analysis of Al-SiC-Ni FGM bottom most layer.

5.5 Energy-dispersive X-ray analysis (EDAX)

The energy-dispersive X-ray analysis (EDAX) shows that there is no presence of any foreign material in the microstructure of the final developed material and also there are no traces of chemical reaction within the elements and nonexistence of carbides and oxides [11, 12] as shown in **Figures 13** and **14**.

5.6 X-ray diffraction analysis (XRD)

The X-ray diffraction analysis (XRD) analysis is exclusively done to determine the grain size, and it is found to be 6.28 Å and the calculated maximum interplanar spacing of the atoms is 3.13 Å [13, 14]. **Table 5** clearly visualizes the effect of the diffraction angle and the full width at half maximum (FWHM) parameter on the crystalline size,

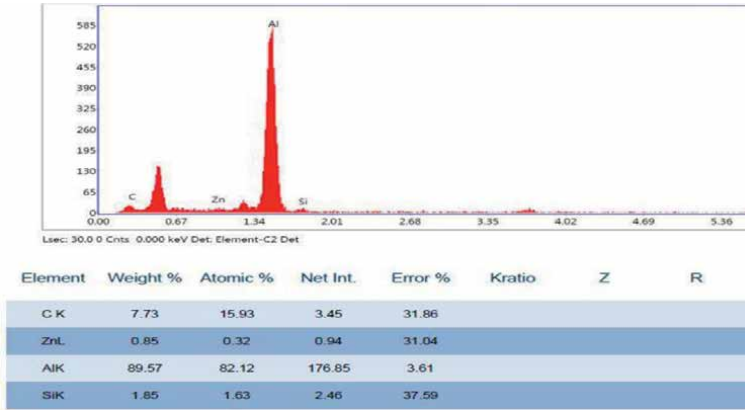


Figure 14.
EDAX test results for bottom layer of Al-SiC-Ni FGM.

Peak position (2θ) (degrees)	FWHM (beta)	Crystalline size (D)
28.44487	0.16022	8.93493
38.51731	0.21445	6.85444
44.77116	0.23935	6.27019
43.34172	0.25013	5.96976
65.15187	0.29904	5.50677
78.29161	0.36344	4.92322
82.50489	0.36068	5.11749

The average crystalline size is 6.224 Angstroms.

Table 5.
XRD values of the dry compacted FGM specimens.

thereby emphasizing the bonding strength between the matrix and the reinforcement constituents and also the size of the ultimate molecules formed after powder metallurgical process [15–17] (**Figure 15**).

5.7 Optimization of the process parameters

Taguchi optimization is used to discover the best fabrication conditions for achieving the best microhardness and compressive strength. We employed the larger is better condition (1) of Taguchi optimization, since the material required great hardness and compacting strength in 95% of the applications [18–21]:

$$Larger\ is\ Better = -10 \log_{10} \left[\left(\frac{1}{n} \right) * \sum \left(\frac{1}{y_i^2} \right) \right] \quad (1)$$

The SN (signal-to-noise) ratios for compressive strength measurements are generated based on the aforesaid equation, and the values are utilized to plot

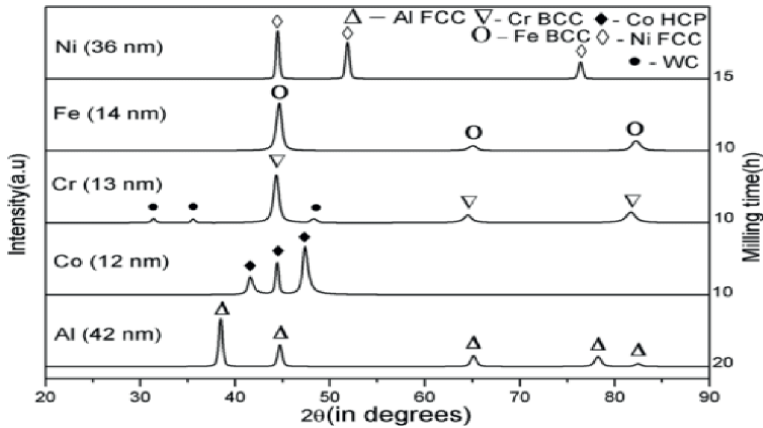


Figure 15.
 XRD graph of Al-Sic-Ni FGM.

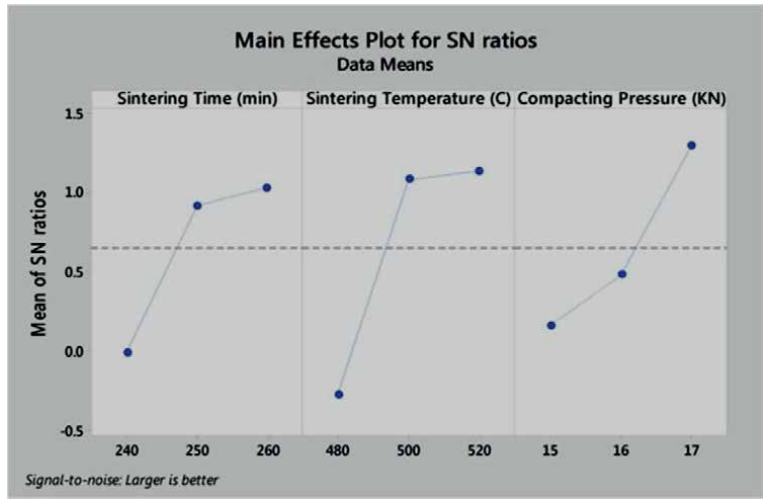


Figure 16.
 SN curves for compressive strength.

the curves, which are shown in **Figure 16**. **Figure 16** shows the SN ratio plots for compressive strength, which shows the effect of each parameter utilized in manufacturing and blend production of the dry-compacted specimens [22–24]. High compressive strength was achieved by using parameters such as compacting pressure, sintering pressure, and sintering duration. When compared with compacting pressure and sintering time, sintering temperature causes high deviations in compressive strength, but sintering duration improves compressive strength as depicted in **Tables 6** and **7** and **Figure 17** [25–27].

6. Conclusion

- FGM prepared through powder metallurgical process has attained ratios and the thorough blending with the aid of tumbling mechanism.

Level	Sintering time	Sintering temperature	Compaction pressure (KN)
1	374	472	447.25
2	398.78	489.36	452.69
3	408.65	498.57	487.25
Delta	34.65	26.57	40
Rank	2	3	1

Table 6.
Response table for the means of the SN ratio of compressive strength.

Level	Sintering time	Sintering temperature	Compaction pressure (KN)
1	1.025	0.985	1.325
2	1.058	1.157	452.69
3	1.154	1.3547	487.25
Delta	34.65	26.57	40
Rank	2	3	1

Table 7.
Response table for the means of the SN ratio of microhardness.

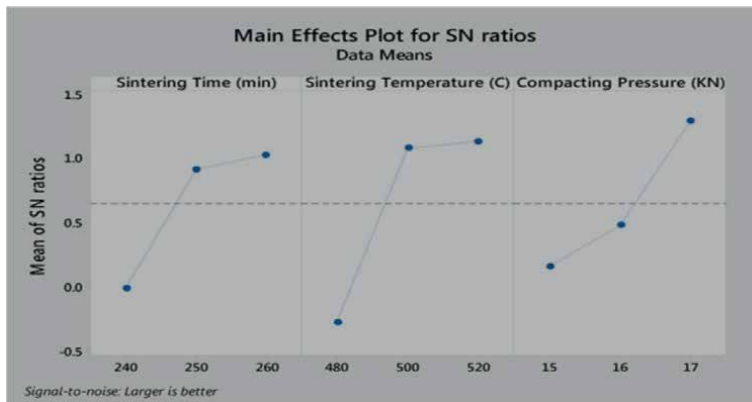


Figure 17.
SN curves for microhardness.

- The FGM is handled effectively by utilizing compaction machine with programmed load controlling limit where the compaction pressure is kept up with at 450KN and ejection load at 50KN.
- The sintered specimens are created at a sintering temperature of 472 degrees centigrade. The FGM shows a full-scale hardness of 34.65% more noteworthy than the Al 356 base metal when led in Brinell hardness tester that is extensively used for macro-hardness and the microhardness is generated with the help of Vicker’s hardness analyzer and observed that the FGM hardness is 2.85 times the base metal.


- The SEM characterization shows the arrangement of grains and grain limits of network and building up materials, and there are no developments of voids, breaks, and surface blemishes. The EDAX shows that there is no synthetic response inside components and furthermore with unfamiliar material and no presence of carbides and oxides.
- The XRD investigation is only done to decide the grain size and its observed to be 6.28 angstroms. The approval of the took on powder metallurgical cycle is confirmed effectively by the pictures shaped in miniature underlying characterization.
- Taguchi optimization conferred that the compressive strength and the micro-hardness have been highly dependent on the sintering temperature, and the microstructural properties are greatly been influenced by the compaction pressure.

Author details

Pattapagalu Naga Sudhakar Srinivas*, Pittam Srinivas Rao, Kolari Deepak
and Nallamilli Srinivas Reddy
Vardhaman College of Engineering, Hyderabad, Telangana, India

*Address all correspondence to: srinivas.pns@vardhaman.org

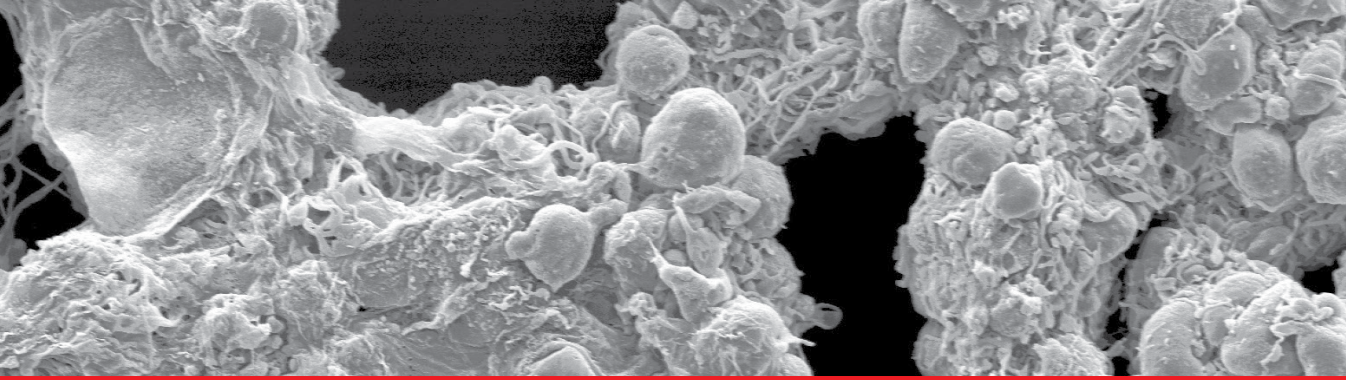
IntechOpen

© 2022 The Author(s). Licensee IntechOpen. This chapter is distributed under the terms of the Creative Commons Attribution License (<http://creativecommons.org/licenses/by/3.0>), which permits unrestricted use, distribution, and reproduction in any medium, provided the original work is properly cited. 

References

- [1] Kim D et al. Carbon nanotubes-reinforced aluminium alloy functionally graded materials fabricated by powder extrusion process. *Materials Science and Engineering: A*. 2019;**745**:379-389
- [2] Devadiga U, Kumar R, Poojary R, Fernandes P. Artificial neural network technique to predict the properties of multiwall carbon nanotube-fly ash reinforced aluminium composite. *Journal of Materials Research and Technology*. 2019;**8**(5):3970-3977
- [3] Radhika N, Raghu R. Abrasive wear behavior of monolithic alloy, homogeneous and functionally graded aluminium (LM25/AlN and LM25/SiO₂) composites. *Particulate Science and Technology*. 2019;**37**(1):10-20
- [4] Kumar R, Chandrappa CN. Synthesis and characterization of Al-SiC functionally graded Material composites using powder metallurgy techniques. *IJRSET*
- [5] Zhang Z-T, Li T-J, Yue H-Y, Zhang J. Preparation of Al/Si functionally graded materials using ultrasonic separation method. *Journal of China Foundry*. 2008;**5**(3):1672
- [6] Gupta K, Saini H, Zaidi MA. Synthesis of functional graded material by powder metallurgy. *Journal of Material Science and Mechanical Engineering (JMSME)*. 2017;**4**(3):163
- [7] Arifin A, Sulong AB, Muhamad N, Syarif J, Ramli MI. Material Processing of Hydroxyapatite and Titanium Alloy (HA/Ti) Composites as Implant Materials using Powder Metallurgy: A Review
- [8] Madhusudhan E et al. Effect of mould wall temperature on rate of solidification of centrifugal casting. *International Journal of Advanced Materials Science*. 2013;**2013**:37
- [9] Daniel-Mkpume CC et al. Silica sand modified aluminium composite: An empirical study of the physical, mechanical and morphological properties. *Materials Research Express*. 2019;**6**(7):076539
- [10] Kim D et al. Fabrication of functionally graded materials using aluminium alloys via hot extrusion. *Metals*. 2019;**9**:210
- [11] Zhang K et al. Free vibration of nonlocal Timoshenko beams made of functionally graded materials by Symplectic method. *Composites Part B: Engineering*. 2019;**156**:174-184
- [12] Salama EI, Morad SS, Esawi AMK. Fabrication and mechanical properties of aluminium-carbon nanotube functionally-graded cylinders. *Materialia*. 2019;**7**:100351
- [13] Chen M et al. Three-dimensional vibration analysis of beams with axial functionally graded materials and variable thickness. *Composite Structures*. 2019;**207**:304-322
- [14] Canakci A, Arslan F, Varol T. Physical and mechanical properties of stir-casting processed AA2024/B4Cp composites. *Science and Engineering of Composite Materials*. 2014;**21**:505-515
- [15] Dhaneşwara D, Syahrial AZ, Ayman MT. Mechanical properties of nano SiC-reinforced aluminium A356 fabricated by stir casting method. *Procedia Engineering*. 2017;**216**:43-50. DOI: 10.4028/www.scientific.net/msf.929.86

- [16] Sivakumar G, Ananthi V, Ramanathan S. Production and mechanical properties of nano SiC particle reinforced Ti–6Al–4V matrix composite. *Transactions on Nonferrous Metals Society China*. 2017;**27**:82-90
- [17] Padmavathi KR, Ramakrishnan R. Tribological properties of micro and nano SiC reinforced Aluminium metal matrix composites. *International Journal of ChemTech Research*. 2017;**10**(6):367-372
- [18] Shashanka R et al. Development of Nano structured duplex and ferritic stainless steels by pulverisette planetary milling followed by pressure less sintering. *Materials Characterization*. 2015;**99**:220
- [19] Avar B, Panigrahi M, Soguksu AK, et al. Photocatalytic activity of soft magnetic Fe_{80-x}Co_xZr₁₀Si₁₀ (x = 0, 40, and 80) nanocrystalline melt-spun ribbons. *Top Catalysis*. 2022
- [20] Shashanka R, Chaira D. Optimization of milling parameters for the synthesis of nano-structured duplex and ferritic stainless steel powders by high energy planetary milling. *Powder Technology*. 2015;**278**:35-45
- [21] Basavarajappa PN et al. Investigation of structural and Mechanical properties of Nanostructured TiMgSr Alloy for Biomedical applications. *Biointerface Research in Applied Chemistry*. 2023;**13**:118
- [22] Gajalakshmi K, Senthilkumar N, Prabu B. Multi-response optimization of dry sliding wear parameters of AA6026 using hybrid gray relational analysis coupled with response surface method. *Measurement Control*. 2019;**1**:14
- [23] Abdalkader NJ, Ahmed PS, Hanoos MM, Riyadh S, Izzat A. Fabrication of metal matrix composites reinforced with nano SiC and studying their corrosion behavior in 3.5%NaCl. *ZANCO. Journal of Pure Applied sciences*. 2016;**28**:251-255
- [24] Rajendrachari S. An overview of high-entropy alloys prepared by mechanical alloying followed by the characterization of their microstructure and various properties. *Alloys*. 2022;**1**:116-132
- [25] Mahale RS et al. Mechanical testing of spark plasma sintered materials: A review. *AIP Conference Proceedings*. 2022;**2469**:200
- [26] Pradeep NB et al. Investigation of microstructure and mechanical properties of microwave consolidated TiMgSr alloy prepared by high energy ball milling. *Powder Technology*. 2022;**408**:1177
- [27] Avar B et al. Micro structural investigations of rapidly solidified Al-Co-Y alloys. *Advances in Materials Science and Engineering*. 2013;**2013**:163537



*Edited by Shashanka Rajendrachari,
Volodymyr Shatokha and Baris Avar*

This book discusses the basics of powder metallurgy and its interesting applications along with various powder manufacturing techniques. It also reviews the wettability of powders and the properties and applications of various metal powders. It is a great tool for understanding the various parameters of sintering techniques. The book includes seven chapters that describe basic concepts of powder metallurgy, sintering, and related applications.

Published in London, UK

© 2023 IntechOpen
© Thomas Spaeter / iStock

IntechOpen

